

**AN EXPERIMENTAL TEST OF CPT CONSERVATION
IN DECAYS OF NEUTRAL KAONS**

by

Gayle Lynne Grazer

A DISSERTATION
PRESENTED TO THE FACULTY
OF PRINCETON UNIVERSITY
IN CANDIDACY FOR THE DEGREE
OF DOCTOR OF PHILOSOPHY

RECOMMENDED FOR ACCEPTANCE
BY THE DEPARTMENT OF
PHYSICS

January 1988

ABSTRACT

We have measured the phase difference $\Delta\phi$ between the complex parameters η_{00} and η_{+-} , which describe CP violation in the decays of neutral kaons to neutral and charged pion final states. These phases are observable in the interference effects which come about from a superposition of short- and long-lived kaons. A non-zero value of $\Delta\phi$, suggested by a 1979 measurement made by a group at New York University, would imply CPT violation. In a recent experiment at Fermilab, we created K_L - K_S interference by sending a pure K_L beam through a regenerator, producing a beam which contained a superposition of both K_S and K_L . We collected over 14,000 decays of these kaons to $\pi^0\pi^0$ and about 110,000 to $\pi^+\pi^-$. The shapes of the proper time spectra for these decays depend on the phases of η_{00} for decays to neutral pions and η_{+-} for decays to charged pions. By comparing these spectra with corresponding distributions obtained from a Monte Carlo simulation, we find that the phase difference $\phi_{00} - \phi_{+-} = -0.2^\circ \pm 9.8^\circ(\text{statistics}) \pm 5.8^\circ(\text{systematic})$. We therefore see no evidence for CPT violation, although within the uncertainty our result is compatible with the NYU measurement.

Contents

Abstract	ii
Acknowledgements	v-vi
Tables	vii
Figures	viii-x
Chapter 1. Introduction	1
1.1 <i>CPT</i> symmetry	1
1.2 The neutral kaon system	2
1.3 Phenomenology of <i>CPT</i> violation	4
1.4 Measuring the phase difference	9
Chapter 2. Design of the experiment	11
Chapter 3. Apparatus	17
3.1 Beam line	17
3.2 Regenerator and decay region	19
3.3 Spectrometer	21
3.4 Lead glass	24
3.5 Background rejection system	28
Chapter 4. Trigger and data acquisition	33
4.1 Charged mode	33
4.2 Neutral mode	34
4.3 Data acquisition	37
4.4 Data collection and samples	38
Chapter 5. Analysis of events	40

5.1 Chamber alignment	40
5.2 Finding tracks	40
5.3 Charged mode: $K \rightarrow \pi^+ \pi^-$	43
5.4 Glass calibration	64
5.5 Finding clusters	65
5.6 Neutral mode: $K \rightarrow \pi^0 \pi^0$	67
Chapter 6. Extracting the phase difference	96
6.1 Outline of the method	96
6.2 The Monte Carlo simulation	97
6.3 Background estimation	108
6.3.1 Diffractive and inelastic regeneration	108
6.3.2 Semileptonic decays	110
6.3.3 $K_L \rightarrow 3\pi^0$ decays	111
6.4 Finding the phase difference	112
Chapter 7. Result and estimate of systematic errors	127
7.1 Result	127
7.2 Estimates of systematic errors	127
7.3 Conclusion	131
7.4 Future plans	131
References	135

Acknowledgements

High energy physics is almost by definition a group effort, and this experiment was no exception. I wish to thank first my advisor, George Gollin, for his continued support and direction. I also wish to acknowledge my other Princeton colleague Jeffrey Okamitsu for many helpful discussions. Many thanks are also due to my collaborators from the University of Chicago (Bruce Winstein, Mary Dung, Koichiro Nishikawa, Ritchie Patterson, Yau Wah, Roland Winston, Michael Woods, Hitoshi Yamamoto), Fermilab (Greg Bock, Rick Coleman, Yee Bob Hsiung, Kenneth Stanfield, Raymond Stefanski, Taku Yamanaka), Elmhurst College (Earl Swallow), and the Centre d'Etudes Nucléaires Saclay (René Turlay, Bernard Peyaud, Pascal Debu, Paloma Cabeza, Remi Daudin, Patrick Jarry). I also wish the best of luck to the newcomers to E731: Magnus Karlsson, Lawrence Gibbons, Vaia Papadimitriou, and Bertrand Vallage.

The technical support staff at Princeton helped us “get it all together”; many thanks go to Howard Edward and the cast of characters at the Elementary Particles Laboratory. I also wish to acknowledge the Fermilab technical staff, especially Gene Beck, as well as the fine help from the University of Chicago and Saclay support staffs.

Last, but by no means least, I wish to thank all my friends everywhere who have helped *me* “keep it together” throughout these often trying times. For service above and beyond the call of duty in assisting with the final production work of this thesis, I owe many thanks to Lloyd Rawley. Space permits the acknowledgement of only a few others: Marvin Bradshaw, Gloria Donaldson, Richard Sumner, John Schivell, Carl Bopp, and Laurel Lerner at Princeton, as well as William Burley, Dennis Farnum, Phyllis Hale, Dwaine Johnson, James Mulvey, Nancy Penson, and Taiji Yamanouchi at Fermilab. I especially wish to express my heartfelt thanks to my family, especially my parents

Harold and Jean Grazer to whom this work is dedicated.

Tables

1. Some experimental <i>CPT</i> tests	2
2. Charged mode events in each data set after all cuts	60
3. Charged mode events in (E,z) bins	92-94
4. Neutral mode events in (E,z) bins	95
5. Charged mode Monte Carlo events in (E,z) bins	104-106
6. Neutral mode Monte Carlo events in (E,z) bins	107
7. Fraction of $2\pi^0$ sample from $3\pi^0$ background	112
8. Neutral p_i^2 background subtraction in (E,z) bins	117
9. Fixed parameter values for phase fit	123
10. Summary of systematic effects	133

Figures

1. ϵ' in the complex plane	6
2. Components of Δ in the complex plane	9
3. E731 spectrometer, elevation view	12
4. Schematic view of the E731 beam line	18
5. Schematic side view of the regenerator	20
6. Schematic side and beam views of the HDRA components	22
7. Drift chamber cell geometry	23
8. Schematic beam view of A bank	24
9. Schematic beam view of B bank	25
10. The E731 lead glass array	27
11. Schematic side view of Princeton lead-lucite counters	30
12. Schematic beam view of Princeton lead-lucite counters	31
13. Schematic side view of glass hole region	32
14. $E_T E_2$ calculated by the mass box for good $K_L \rightarrow 3\pi^0$ decays	36
15. Finding p_t^2 for a charged decay	45
16. Number of RA counters hit per charged event	45
17. Distance of pion track from center of vacuum window	47
18. Aperture cuts on pion tracks at the A bank	48
19. Aperture cuts on pion tracks at the B bank	49
20. Aperture cuts for kaons at the regenerator	50
21. Invariant mass of “ $p\pi$ ” for kaon energy > 130 GeV	51
22. Aperture cuts on pion tracks at the B bank in lead curtain hole region	52
23. Aperture cuts on pion tracks at the μ_2 bank	53

24. Momentum of pion tracks	54
25. Track s^2 for upstream x and y views	55
26. Weighted distance of closest approach/ σ_{dcl}	56
27. Meeting-in-the-magnet track offsets/ σ_{offset}	56
28. Reconstructed p_t^2 for charged decay events	58
29. Reconstructed kaon mass	59
30. Λ^0 mass after separate analysis	60
31. Charged decay vertex distributions	61-62
32. Reconstructed kaon energy distributions, charged events	63
33. E/p as a function of E	66
34. Weighted x track separation at the glass for lepton tracks	69
35. Energy distributions in the back anti	71
36. Number of RA counters hit per charged event	73
37. Signal in collar anti	73
38. Signal in VA3	74
39. Signal in DRAN	74
40. Hits in VA2, VA3, and VA4 scintillators	75
41. Lepton track separation at glass	76
42. Neutral pairing algorithm	79
43. χ^2 for best photon pairing	80
44. Neutral decay vertex distributions	81-82
45. Reconstructed energy of photon clusters	83
46. Weighted separation at the glass for lepton tracks	83
47. Finding p_t^2 for a neutral decay	85
48. p_t^2 for events from regenerated beam	86

49. p_t^2 for events from vacuum beam	86
50. Electron cluster energy/track momentum	87
51. Distance of lepton track from center of vacuum window	87
52. Positions of e^+e^- tracks at the A bank	88
53. Positions of e^+e^- tracks at the B bank	89
54. Reconstructed kaon energy distributions, neutral events	90
55. Reconstructed kaon mass, regenerated beam	91
56. Reconstructed kaon mass, vacuum beam	91
57. Charged mode data to Monte Carlo energy comparison	101
58. Neutral mode data to Monte Carlo energy comparison	101
59. Charged mode data to Monte Carlo z comparison	102
60. Neutral mode data to Monte Carlo z comparison	103
61. Charged p_t^2 distribution with background fit	109
62. Neutral p_t^2 distribution with background fit	111
63. Diffractive/inelastic events as a function of z	114-116
64. Average true E as a function of z , charged	119
65. Average true z -reconstructed z , charged	120
66. Average true E as a function of z , neutral	121
67. Average true z -reconstructed z , neutral	122
68. $\Delta\phi$ as a function of z limits	129
69. Energy scale effects on $\Delta\phi$	132

Chapter 1

INTRODUCTION

1.1 *CPT* symmetry

The discoveries of approximate and exact symmetries in the ways that particles interact have been useful guides to the physicists trying to describe these interactions. Three of these symmetries are C , P , and T , for charge conjugation, parity, and time reversal, respectively. These symmetries may be applied individually or in combinations. Perhaps the most important of these is the combination of CPT , mainly because of the *CPT Theorem*,¹ which states that a field theory of local interactions that is Lorentz invariant² is invariant under the combined operation of CPT or any of its permutations. These hypotheses are so general and fundamental to our current understanding of interactions that any violation of this symmetry would be surprising. A detected violation of CPT would not only call into question the assumptions on which the theorem rests but also change our understanding of matter *vs.* antimatter. CPT conservation predicts, for instance, the equality of masses, lifetimes, and magnetic moments for particles and their antiparticles. Some of the more sensitive experimental limits on CPT conservation are given in Table 1.

Current experimental limits suggest that C , P , and T individually are exact symmetries of both the strong and electromagnetic interactions. The weak interaction, however, violates both C and P , although T violation has not yet been directly observed. Conservation of both T and CPT implies conservation of the combined symmetry CP .

Table 1. Some experimental CPT tests (from ref. 3)

Test	Limit
$(g_{e^+} - g_{e^-})/\text{average}$	$(2.2 \pm 6.4) \times 10^{-11}$
$(g_{\mu^+} - g_{\mu^-})/\text{average}$	$(-2.6 \pm 1.6) \times 10^{-8}$
$K^0 - \bar{K}^0$ mass difference/average	$< 6 \times 10^{-19}$
$K^+ - K^-$ mass difference/average	$(-0.6 \pm 1.8) \times 10^{-4}$
$\mu^+ - \mu^-$ mean lifetime difference/average	$(3 \pm 8) \times 10^{-5}$
$K^\pm \rightarrow \mu^\pm \nu$ rate difference/average	$(0.54 \pm 0.41)\%$

1.2 The neutral kaon system

It is particularly instructive to describe the neutral kaon system, the K^0 and its antiparticle the \bar{K}^0 , in terms of CP . Neutral kaons were observed to decay to both two pion and three pion final states. Quantum statistics arguments tell us that both the $\pi^0\pi^0$ and the $\pi^+\pi^-$ final states must have $CP = +1$, while similar arguments for $\pi^+\pi^-\pi^0$ and $\pi^0\pi^0\pi^0$ give an assignment of primarily $CP = -1$ to these states. Applying CP to the $|K^0\rangle$ state gives $e^{i\theta}|\bar{K}^0\rangle$, where θ is unmeasurable so we may choose it to be zero. Thus,

$$|\bar{K}^0\rangle \equiv CP|K^0\rangle$$

and

$$|K^0\rangle \equiv CP|\bar{K}^0\rangle.$$

We can then construct CP eigenstates as candidates for the observed weak eigenstates:

$$|K_1\rangle = \frac{1}{\sqrt{2}}(|K^0\rangle + |\bar{K}^0\rangle) \quad (CP = +1)$$

and

$$|K_2\rangle = \frac{1}{\sqrt{2}}(|K^0\rangle - |\bar{K}^0\rangle) \quad (CP = -1).$$

If CP were conserved, the K_1 would then decay rapidly to two pions, while the K_2 would decay more slowly because of the limited phase space available for three-body decays. The short-lived K was well-known when this description was put forward; the long-lived K was subsequently found,⁴ lending support to the model. In 1964, however, Christenson *et al.*⁵ found that the long-lived K also decayed to two pions, albeit at a much reduced rate. Since this CP violation is so small, it is most convenient to express the weak eigenstates $|K_S\rangle$ and $|K_L\rangle$ in the $K_1 - K_2$ basis:

$$|K_S\rangle = \frac{1}{\sqrt{(1 + |\varepsilon_S|^2)}}(|K_1\rangle + \varepsilon_S|K_2\rangle)$$

and

$$|K_L\rangle = \frac{1}{\sqrt{(1 + |\varepsilon_L|^2)}}(\varepsilon_L|K_1\rangle + |K_2\rangle),$$

where the magnitudes of ε_L , ε_S are approximately 2×10^{-3} .

With these definitions in mind, it may be helpful to review briefly some relevant features of the quantum mechanics of neutral kaons.⁶ The proper time evolution of a K_L or K_S can be represented by $c \exp(-im\tau) \exp(-\Gamma\tau/2)|K\rangle$, where m is the kaon mass, τ is the proper time, and Γ is the decay rate. A beam containing an arbitrary fraction of both is then described by

$$\psi(\tau) = c_L e^{-im_L\tau} e^{-\Gamma_L\tau/2} |K_L\rangle + c_S e^{-im_S\tau} e^{-\Gamma_S\tau/2} |K_S\rangle.$$

Consider the decay of such a mixture to a final state f :

$$A(\psi \rightarrow f) = c_L e^{-im_L\tau} e^{-\Gamma_L\tau/2} A(K_L \rightarrow f) + c_S e^{-im_S\tau} e^{-\Gamma_S\tau/2} A(K_S \rightarrow f),$$

where the decay amplitudes are complex. There is nothing to prevent us from expressing $A(K_L \rightarrow f)$ as $\eta A(K_S \rightarrow f)$, where η is a complex number. Multiplying the amplitude

$A(\psi \rightarrow f)$ by its complex conjugate gives us the observable decay rate:

$$\begin{aligned} \Gamma(\psi \rightarrow f) = & \Gamma(K_S \rightarrow f) \times \\ & [|c_L|^2 |\eta|^2 e^{-\Gamma_L \tau} \\ & + 2 |c_L| |c_S| |\eta| \cos(\phi_\eta + (m_L - m_S)\tau) e^{-(\Gamma_L + \Gamma_S)\tau/2} \\ & + |c_S|^2 e^{-\Gamma_S \tau}], \end{aligned}$$

where we have absorbed any extra phases from c_L and c_S into the phase of η . The second term comes from the coherent interference of K_S with K_L ; here the phase of η appears as a measurable quantity. [Recall that above we said that the phase θ between the K^0 and \bar{K}^0 was unmeasurable. We can see from an argument similar to the one above that this is so because strangeness is conserved, so the K^0 and \bar{K}^0 cannot go to the same final state.] We are now ready to consider some more complicated phenomenology.

1.3 Phenomenology of CPT violation⁷

As suggested by Table 1, one of the most sensitive places in which to look for possible CPT violations is the neutral kaon system; this is the only system, for example, in which CP violation has been observed. In addition to mass or lifetime differences, however, CPT violation could manifest itself as a difference in phase between the neutral decay CP -violating amplitude ratio

$$\eta_{00} = |\eta_{00}| e^{i\phi_{00}} \equiv \frac{A(K_L \rightarrow \pi^0 \pi^0)}{A(K_S \rightarrow \pi^0 \pi^0)}$$

and its counterpart for charged decays η_{+-} , as we shall see below. (Current values for these parameters are $|\eta_{00}| = (2.299 \pm 0.036) \times 10^{-3}$, $\phi_{00} = (54 \pm 5)^\circ$, $|\eta_{+-}| = (2.275 \pm 0.021) \times 10^{-3}$, and $\phi_{+-} = (44.6 \pm 1.2)^\circ$.³) First let us assume that CPT is conserved. We can look at the decay products of the K^0 - \bar{K}^0 system in terms of two

pion final states of definite isospin I rather than states of definite charge by defining the amplitudes A_I as follows:

$$A(K^0 \rightarrow \pi\pi, I) = A_I e^{i\delta_I}.$$

CPT conservation implies

$$A(\bar{K}^0 \rightarrow \pi\pi, I) = A_I^* e^{i\delta_I},$$

where operating with C has changed the K^0 to \bar{K}^0 and T has given the complex conjugate of the amplitude A_I . The δ_I represent final state $\pi\pi$ scattering phase shifts and are not affected by the decay interaction itself; they are therefore unchanged. An additional parameter ϵ' may be defined as

$$\begin{aligned} \epsilon' &= \frac{1}{\sqrt{2}} \frac{A(K_2 \rightarrow \pi\pi, I=2)}{A(K_1 \rightarrow \pi\pi, I=0)} \\ &= \frac{1}{\sqrt{2}} i \frac{\text{Im}A_2}{\text{Re}A_0} e^{i(\delta_2 - \delta_0)}. \end{aligned}$$

From the definition we see that ϵ' describes direct CP violation in the decay interaction, rather than the CP violation observed because of the $K_1 - K_2$ mixing which gives K_L and K_S and which is described by ϵ .

We also see that $\phi_{\epsilon'} = \delta_2 - \delta_0 + \pi/2$ or $\delta_2 - \delta_0 - \pi/2$, depending on the sign of ϵ' . The phase shifts δ_I have been measured in a variety of experiments. In their review of kaon data, Devlin and Dickey⁸ found an average of $(-45 \pm 5)^\circ$ for $\delta_2 - \delta_0$ from pion production, while Cronin⁹ averaged results from K_{e4} decays, $K_{\pi 2}$ decays, and pion production to obtain a similar result. With this value, we expect the phase of ϵ' to be either 45° or -135° , approximately parallel or antiparallel to η_{+-} .

For comparison with experiment, ϵ' can also be expressed as

$$\epsilon' = \frac{1}{3}(\eta_{+-} - \eta_{00}) + \left(\frac{1}{3}\eta_{+-} + \frac{2}{3}\eta_{00} - \epsilon_L\right)\omega,$$

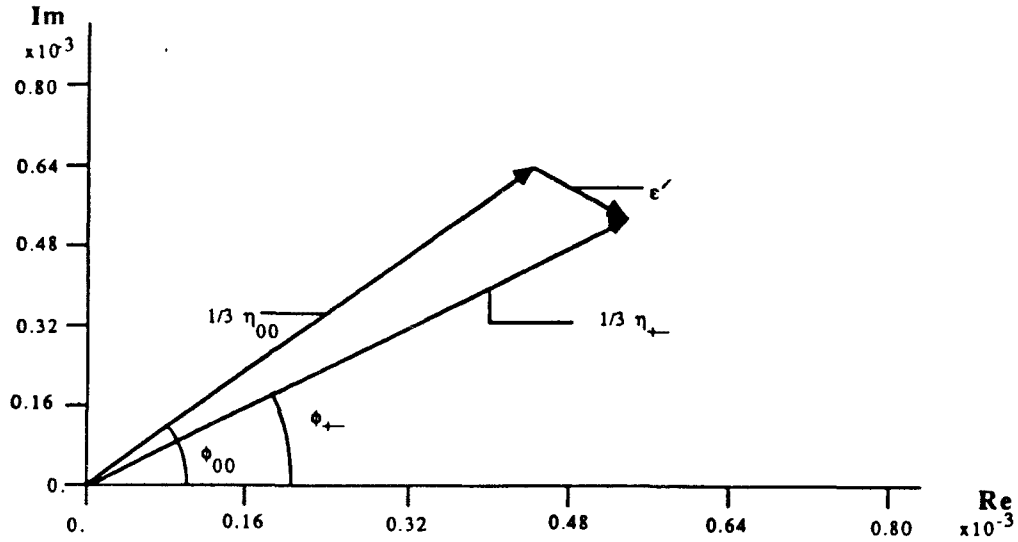


Figure 1. ϵ' in the complex plane

where

$$\omega \equiv \frac{1}{\sqrt{2}} \frac{A(K_S \rightarrow \pi\pi, I=2)}{A(K_S \rightarrow \pi\pi, I=0)}, \quad |\omega| \simeq .03$$

describes $|\Delta I| = 1/2$ rule violations. If we assume *CPT* conservation, the first term in the ϵ' expression is about 15 times greater than the second. Neglecting the term containing ω , then, we have

$$\epsilon' \simeq \frac{1}{3}(\eta_{+-} - \eta_{00}).$$

(See Figure 1.)

Using the current values of η_{+-} and η_{00} as shown in the figure gives a phase for ϵ' different from that expected from $(\delta_2 - \delta_0)$ measurements by nearly 90° , mostly the result of the difference between ϕ_{00} and ϕ_{+-} . To quantify this, let us consider the components of ϵ' with respect to the direction $\delta_2 - \delta_0 + \pi/2 = 45^\circ$. Evaluating these

using the experimentally determined values for η_{00} and η_{+-} gives

$$|\varepsilon'_{\perp}| = (0.13 \pm 0.06) \times 10^{-3},$$

while

$$|\varepsilon'_{\parallel}| = (0.00 \pm 0.05) \times 10^{-3},$$

giving an ε'_{\perp} which is consistent with zero only at the two standard deviation level.

Now let us consider the same analysis if we do not require *CPT* conservation. We can construct a new kaon decay amplitude which also includes a *CPT*-violating term B_I :

$$A(K^0 \rightarrow \pi\pi, I) = (A_I + B_I)e^{i\delta_I}.$$

Application of *CPT* to this expression gives

$$A(\bar{K}^0 \rightarrow \pi\pi, I) = (A_I^* - B_I^*)e^{i\delta_I},$$

where the sign difference follows from the requirement that the second term be odd under *CPT*. These new expressions for the amplitudes imply

$$\varepsilon' = \frac{1}{\sqrt{2}} \frac{\text{Re}B_2 + i\text{Im}A_2}{\text{Re}A_0 + i\text{Im}B_0} e^{i(\delta_2 - \delta_0)},$$

where the phase of ε' now need not be $\delta_2 - \delta_0 + \pi/2$ or $\delta_2 - \delta_0 - \pi/2$. We see that incorporating *CPT* violation gives us a way to describe an ε'_{\perp} component.

In addition to $|\Delta S| = 1$ processes, a $\phi_{00} - \phi_{+-}$ phase difference can signal *CPT* violation in $\Delta S = 0$ ($K^0 \leftrightarrow \bar{K}^0$) and $|\Delta S| = 2$ ($K^0 \leftrightarrow \bar{K}^0$) transitions. To see this more clearly, let us use the Wigner-Weisskopf formulation¹⁰ applied to neutral kaons:¹¹

$$-\frac{d}{dt} \begin{pmatrix} a \\ \bar{a} \end{pmatrix} = \left(iM + \frac{1}{2}\Gamma \right) \begin{pmatrix} a \\ \bar{a} \end{pmatrix},$$

where a, \bar{a} are the amounts of K^0 and \bar{K}^0 amplitudes present at a given time, and M and Γ are the “mass” and “decay” matrices, each Hermitian, with elements M_{ij} and Γ_{ij} . Let us now construct another CPT -violating parameter

$$\Delta = \frac{i(M_{11} - M_{22}) + \frac{1}{2}(\Gamma_{11} - \Gamma_{22})}{i(m_S - m_L) + \frac{1}{2}(\Gamma_S - \Gamma_L)}.$$

M_{11} is m_K , while M_{22} is $m_{\bar{K}}$. Γ_{11} and Γ_{22} are the K^0 and \bar{K}^0 decay rates, respectively. Note that the off-diagonal elements are nonzero because of the mixing to give the decay eigenstates. Since CPT conservation implies that $m_K = m_{\bar{K}}$ and $\Gamma_K = \Gamma_{\bar{K}}$, $\Delta = 0$ if CPT holds. We can compare this with experimental results by looking at the components of Δ with respect to the unit vector that makes an angle $\phi = \arctan(2(m_L - m_S)/(\Gamma_S - \Gamma_L))$ with the real axis. After some algebra we find that $\Delta_{\parallel} \propto (\Gamma_{11} - \Gamma_{22})$ and $\Delta_{\perp} \propto (M_{11} - M_{22})$. These components can be evaluated as has been done in both references 7 and 11. For our purposes, it is sufficient to present the results. Reference 11 finds

$$\Delta_{\parallel} = \cos \phi [\text{Re} \bar{\alpha} + \text{Re} \varepsilon_0 - \text{Re} \varepsilon_L]$$

and

$$\Delta_{\perp} = -\varepsilon_{0\perp} - \cos \phi \text{Im} \bar{\alpha} - \sin \phi [\text{Re} \varepsilon_0 - \text{Re} \varepsilon_L],$$

where

$$\bar{\alpha} = (1/\Gamma_S) \sum_f A^*(K_S \rightarrow f) A(K_L \rightarrow f)$$

with final states f of $\pi\pi, I = 2$; $\pi l\nu$; $\pi^0\pi^0\pi^0$; and $\pi^+\pi^-\pi^0$; and

$$\varepsilon_0 = \frac{1}{3}(2\eta_{+-} + \eta_{00}) + \frac{2}{3}(\eta_{+-} - \eta_{00})\omega = \frac{A(K_L \rightarrow 2\pi, I = 0)}{A(K_S \rightarrow 2\pi, I = 0)}.$$

Using the values for these parameters given in reference 7, we find

$$\Delta_{\parallel} = (-0.09 \pm 0.07) \times 10^{-3},$$

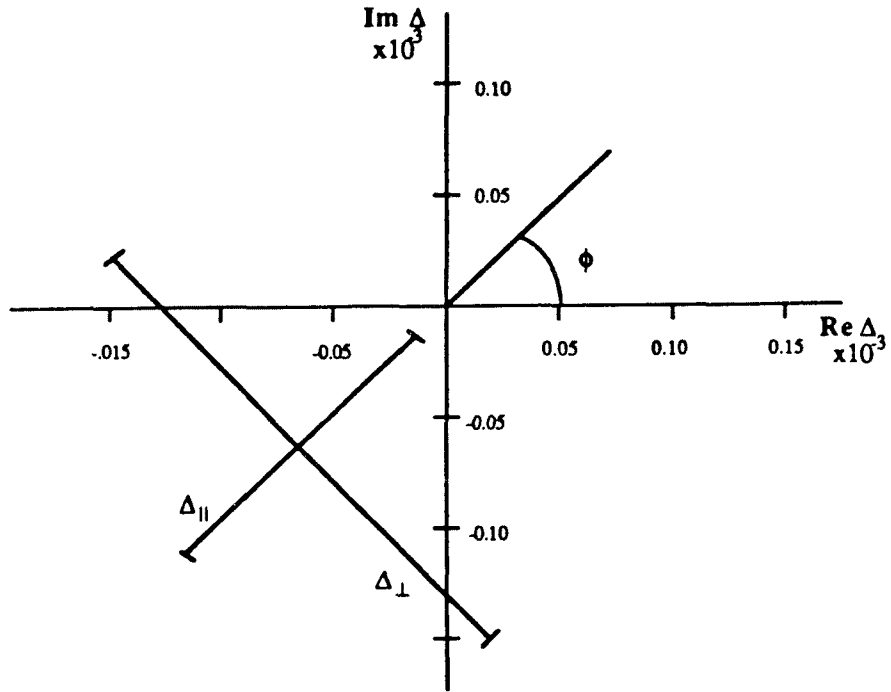


Figure 2. Components of Δ in the complex plane.

and

$$\Delta_{\perp} = (-0.06 \pm 0.12) \times 10^{-3},$$

with no evidence of a *CPT* violation. (See Figure 2.)

1.4 Measuring the phase difference

Since most of the discrepancy of ϵ'_{\perp} from zero comes from the neutral phase, how reliable is our knowledge of $\phi_{00} - \phi_{+-}$? The world average value³ is $(9.8 \pm 5.4)^{\circ}$, while the best single value comes from a 1979 measurement by a group from New York

University which found $(12.6 \pm 6.2)^\circ$.¹² The experiment which produced the data used in the present analysis was designed to measure the decay rates used to calculate $|\eta_{00}|$ and $|\eta_{+-}|$. A pure K_L beam was used to produce K_S using the regeneration property of neutral kaons. Regeneration refers to the increase in the amount of K_S in a kaon beam relative to the amount of K_L after the beam has traversed some matter. Thus an incident K_L beam such as ours had some fraction of K_S in addition to the K_L after passing through the regenerator.

Let us look more closely at how this comes about. Neutral kaons are produced in the strong eigenstates K^0 and \bar{K}^0 . When such a beam is incident on matter, the two strong components interact differently with it because of strangeness conservation: the K^0 can only scatter, while the \bar{K}^0 can scatter but can also be absorbed in associated production reactions. K_S regeneration is described as

$$|K_L(0)\rangle \rightarrow |K_L(t)\rangle + \rho|K_S(t)\rangle,$$

where ρ is the complex regeneration amplitude and terms of order $|\rho|^2$ have been neglected. $|\rho|$ is typically a few $\times 10^{-2}$ for our incident kaon energies and regenerator. The decay rate to two pions downstream of a regenerator, then, is

$$\begin{aligned} & |A(K_L(t) \rightarrow 2\pi) + \rho A(K_S(t) \rightarrow 2\pi)|^2 \\ &= \Gamma(K_S \rightarrow 2\pi)[|\rho|^2 e^{-\Gamma_S \tau} \\ &+ 2|\rho||\eta| e^{-(\Gamma_S + \Gamma_L)\tau/2} \cos(\Delta m \tau + \phi_\rho - \phi_\eta) \\ &+ |\eta|^2 e^{-\Gamma_L \tau}]. \end{aligned}$$

Here we see ϕ_η (either ϕ_{00} or ϕ_{+-} , depending on the 2π decay mode under study) appearing in a physically measurable way. Let us now consider some of the practical problems encountered in doing a measurement of this sort.

Chapter 2

DESIGN OF THE EXPERIMENT

CPT tests aside, there is still a great deal of uncertainty in our knowledge of *CP* violation. At this writing, it is still unclear whether the only *CP*-violating effect in the $K - \bar{K}$ system comes from the $K_1 - K_2$ mixing or whether the decay interaction itself also violates *CP*. Fermilab experiment 731 is attempting to settle this point with a precision measurement of

$$\left| \frac{\eta_{00}}{\eta_{+-}} \right|^2 = \frac{\Gamma(K_L \rightarrow \pi^0 \pi^0)}{\Gamma(K_S \rightarrow \pi^0 \pi^0)} \bigg/ \frac{\Gamma(K_L \rightarrow \pi^+ \pi^-)}{\Gamma(K_S \rightarrow \pi^+ \pi^-)}.$$

The difference between this ratio and 1 is proportional to $|\epsilon'/\epsilon|$. To do such a measurement requires the ability to produce both K_L and K_S , as well as the ability to collect data from all four decay modes. To do such a measurement precisely requires the ability to understand the performance of our detector very well.

The K_L were obtained from primary protons incident on a target which produced a mixture of K^0 and \bar{K}^0 . By waiting long enough (looking far enough downstream), the K_S decayed away leaving only K_L . We produced two of these K_L beams; putting a block of material in one of the K_L beams gave us some new K_S , as described above. All decays of interest were constrained to be upstream of the conversion plane hodoscope (Figure 3.).

For charged decays ($K \rightarrow \pi^+ \pi^-$), the decay products were tracked in a series of four drift chambers. A magnet between the second and third chambers allowed us to measure the momenta of the tracks; extrapolating the tracks in the two chambers upstream of the magnet allowed us to determine the decay vertex of the parent kaon.

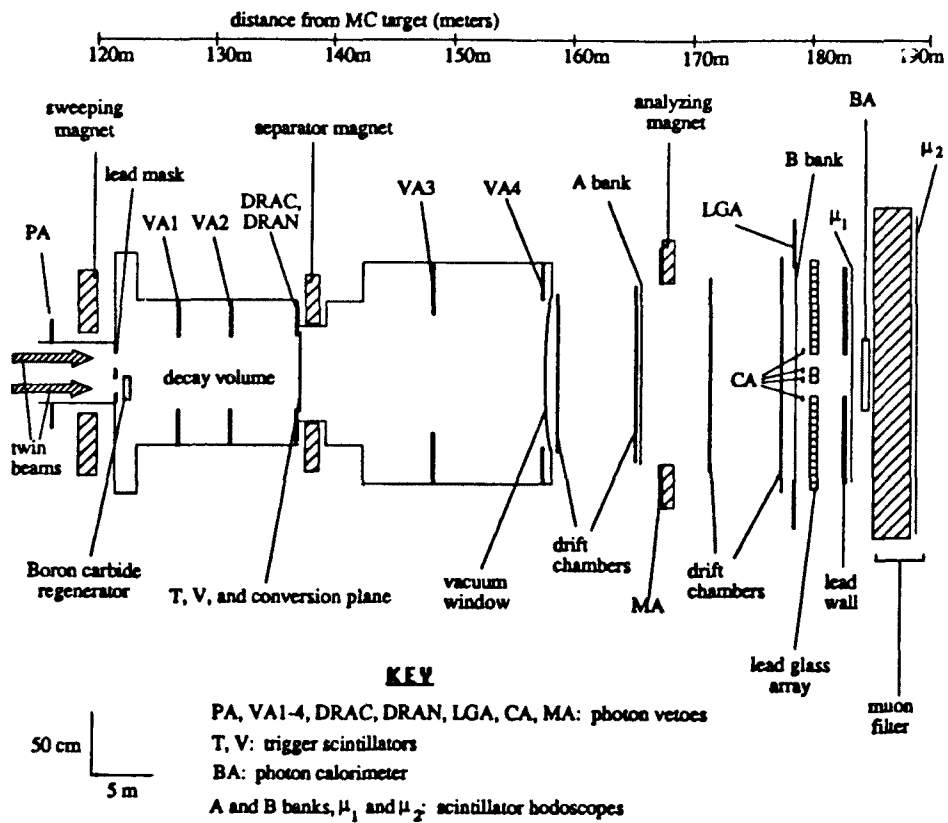


Figure 3. E731 spectrometer, elevation view.

Scintillator banks on either side of the magnet as well as at the end of the decay volume provided the topological information we used to trigger the data acquisition system.

For neutral decays ($K \rightarrow \pi^0\pi^0$), a lead glass array downstream of the chambers was used to measure the energy of photons from the π^0 's, determining the kaon energy and the decay vertex position along the beam direction. Transverse vertex information was obtained by placing a thin lead sheet at the downstream end of the decay volume to convert one of the photons to an electron-positron pair which could be momentum-analyzed and also tracked back to the conversion plane. Having a pair of charged particles allowed us to trigger using two of the three hodoscopes used in the charged mode.

By using essentially the same detector for K_S and K_L in both charged and neutral decay modes, we could cross check our understanding of the neutral decay data with that from the better-resolved charged mode. For example, we could determine the incident energy spectrum of kaons and the positions of various spectrometer elements from the charged mode data and compare them with those obtained from the neutral mode analysis as a check on the neutral mode energy calibration. The neutral energy calibration itself relied on the chambers for accurate electron momentum determination.

Because we wanted to do a precision measurement, we had to reduce our sensitivity to time-dependent systematic effects. Counter efficiencies could have drifted, for example, or changed as a function of beam intensity. The frequency of accidental events might have increased as a function of activity in the apparatus. The amount of computer deadtime might also have been different between K_L and K_S decays. Say, for example, that a K_S beam had a higher trigger rate than a K_L beam. It would then be possible for a larger fraction of K_L events relative to a flux monitor (needed to normalize the rates) to be accepted, while proportionally more K_S events would be lost. Any of

these problems could have systematically eliminated more K_S or K_L . To avoid this, we collected K_L and K_S decays simultaneously using two vertically separated beams, eliminating the need for a separate flux monitor. Decays to neutral pions were recorded at a different time from decays to charged pions. Because the beam targetting was done in the horizontal direction, beam intensity was a strong function of horizontal distance from the center of the beam. Placing one beam above the other rather than next to it reduced possible intensity differences between the two beams. We placed a regenerator in one beam at a time, alternating its position between pulses to average out any remaining intensity differences between the two beams. We switched between charged and neutral pion collection every few weeks.

We anticipated other possible biases due to our background subtraction procedures, since the sources of background are different for K_S and K_L . The decay spectrum for kaons downstream of a regenerator given in the previous chapter holds only for the case in which the exiting kaons are scattered in the forward direction by the entire regenerator, giving a coherent superposition of K_L and K_S amplitudes. Not all K interactions result in this coherent regeneration, however; diffractive regeneration, in which a kaon scattered from a single nucleus rather than the entire regenerator, gave a background to the coherent peak. Because of the imperfect resolution of our detector, some of these incoherently scattered events will appear to have scattered coherently; it is necessary, therefore, to reject as many K 's as possible which really received nonzero transverse momentum (p_t) kicks in the regenerator. We used readily available boron carbide for the regenerator because its small nuclei tend to give kaons larger scattering angles and so fewer events with small p_t that could be confused with resolution-smearred ones.

The ratio of coherent regeneration to diffractive is proportional to the length of the

regenerator,¹³ favoring long regenerators for relatively higher coherent production. This calculation ignores absorption, however. For coherent regeneration, it can be shown that $|\rho|^2 \propto L^2$ without absorption. Maximizing the yield when the absorption factor $e^{-L/\Lambda}$ is included, where Λ is the interaction length, gives an optimal regenerator length of 2Λ . The regenerator was also instrumented with anticounters to reject events in which a kaon interacted inelastically with a nucleus and produced extra particles.

In addition to reducing the sources of p_t background, we also improved the p_t resolution by minimizing multiple scattering in all elements of the detector. We accomplished this by evacuating the path of the kaon and its resulting decay products from just downstream of the target to just upstream of the first drift chamber. The large air gaps between chambers were filled with helium bags. The chamber windows, the hodoscopes, and the vacuum window at the downstream end of the decay volume were made as thin as possible. In addition to reducing multiple scattering, having so little material in the beam reduced the number of false triggers caused by the interaction of neutrons from the beam with various detector elements.

Backgrounds to the K_L beams came primarily from other K_L decay modes. The CP -violating decay $K_L \rightarrow \pi^+\pi^-$ had to compete against $K_L \rightarrow \pi^\pm e^\mp \nu$ with a branching fraction of 39%, $K_L \rightarrow \pi^\pm \mu^\mp \nu$ (branching fraction 27%), and $K_L \rightarrow \pi^+\pi^-\pi^0$ (12%). The $K_{\mu 3}$ decays were suppressed by detecting the muons in a scintillator bank at the end of the spectrometer, just downstream of three meters of steel. $K_{e 3}$ and $\pi^+\pi^-\pi^0$ decays were eliminated by placing a removable lead curtain in front of the second scintillator bank during $\pi^+\pi^-$ data-taking. This lead converted photons from the π^0 's; these electrons, as well as electrons from $K_{e 3}$ decays, showered in the lead, producing a large signal in the scintillators which allowed us to reject these events at the trigger level.

The primary neutral mode background to $K_L \rightarrow \pi^0\pi^0$ came from $K_L \rightarrow 3\pi^0$

decays (branching ratio 22%) in which two of the six photons were lost or fused with other showers in the glass. Veto counters were designed to tag events with photons wide of the glass for rejection offline. The number of fusion events was reduced by introducing another magnet just downstream of the decay volume to compensate for the kick given to the e^+e^- pair in the analyzing magnet, giving an overall focussing effect and reducing the number of separate energy depositions in the glass. *Bremsstrahlung* photons produced by the pair in the lead sheet traveled near the original photon direction and so hit the glass at the point where the pair converged. Spreading the pair out early also made track separation in the chambers easier since otherwise the only separation of the pair would come from multiple scattering in the lead.

Chapter 3

APPARATUS

3.1 Beam line

With this overview in mind, we may now look in detail at the apparatus. The data for this analysis were produced in the Meson Center beamline at Fermilab during the 1985 Tevatron fixed target running period (March through September) (see Figure 4).

For standard data taking, we used a one-proton-interaction-length beryllium target (about $3.2 \text{ mm} \times 3.2 \text{ mm} \times 30.5 \text{ cm}$) bombarded at an angle of 5 mrad with approximately 1×10^{12} 800-GeV protons per twenty second spill. Because neutron production is peaked in the forward direction (an angle of 0 mrad), targetting at this angle increased the kaon to neutron ratio in our neutral beam. Fermilab provided us with control of two upstream trim magnets as well as a beam profile monitor, allowing us to adjust the beam direction as needed. The proton beam was about 3 mm in diameter at the target. Sweeping magnets immediately downstream of the target disposed of any charged particles, and the remaining beam was passed through a two-hole collimator. The holes were about 1.0 cm wide and 0.9 cm high, with centers spaced 1.8 cm apart. The downstream end of each hole was plugged with 7.6 cm of lead and 54 cm of beryllium. These plugs were designed to act as neutral “sweepers”, i.e., to remove other unwanted particles from the neutral beam. Photons from π^0 decays were converted in the lead, and the resulting charged particles were then swept out of the beam by more magnets downstream. Since the interaction length for kaons in beryllium is 50% longer than for neutrons, approximately 17% of incident neutrons emerged unscattered from

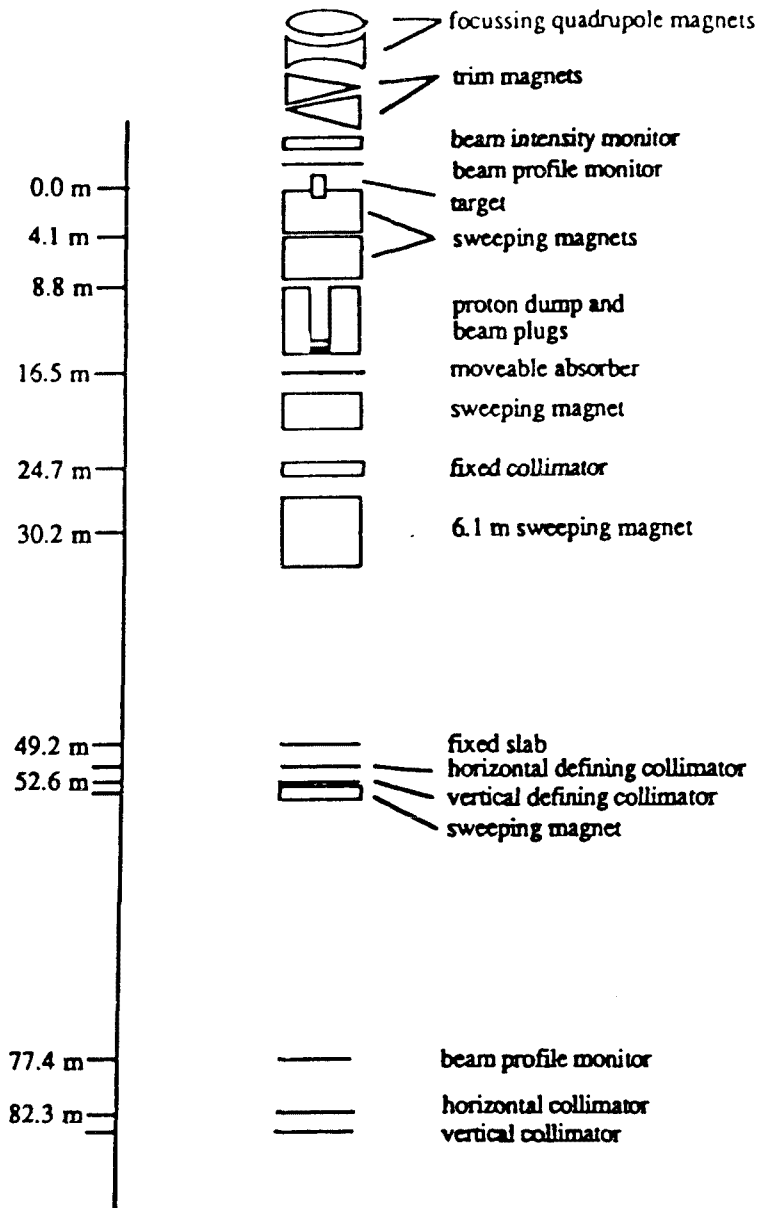


Figure 4. Schematic view of the E731 beam line. The z scale is approximate.

the plug, to be compared with 31% of incident kaons. We thus improved our kaon to neutron ratio by a factor of 1.8.

In addition to the common plugs, the beam in which the regenerator was placed passed through an absorber of 46 cm of beryllium to attenuate the beam. Beryllium was chosen for its low Z and its kaon/neutron enhancement properties. Because the error on ϵ'/ϵ was limited by the collected $K_L \rightarrow 2\pi^0$ statistics, we needed the absorber to limit the number of competing $K_S \rightarrow 2\pi$ decays. Without the absorber we would have had about ten times more K_S data than K_L data; with it we had only 3-4 times more. If we had had unlimited running time, we could have just run longer. This, unfortunately, was not possible.

Downstream of the absorber, a slab and two defining collimators narrowed the beams down to their final sizes. The horizontal collimator aperture was 2.9 cm wide, while the vertical collimator aperture was 9.7 cm high. The slab was 3.6 cm thick and masked off the region between the two beams. The beams traveled in vacuum for 90 meters from the absorber to the spectrometer, where an estimated 6×10^6 kaons, 6×10^6 neutrons, 8×10^6 muons (most made in the proton dump), and a few thousand Λ^0 's arrived per spill. The beams passed through a sweeping magnet at the entrance to our apparatus, eliminating muons and charged particles from upstream decays. The magnet was used primarily in neutral mode data collection and glass calibration, as its use in the charged mode would have limited our acceptance of upstream decays in the charged mode.

3.2 Regenerator and decay region

The regenerator itself was made in four sections, each consisting of a 10 cm \times 10 cm \times 19 cm block of boron carbide, followed by 1.3 cm of lead, and 0.6 cm of scintillator

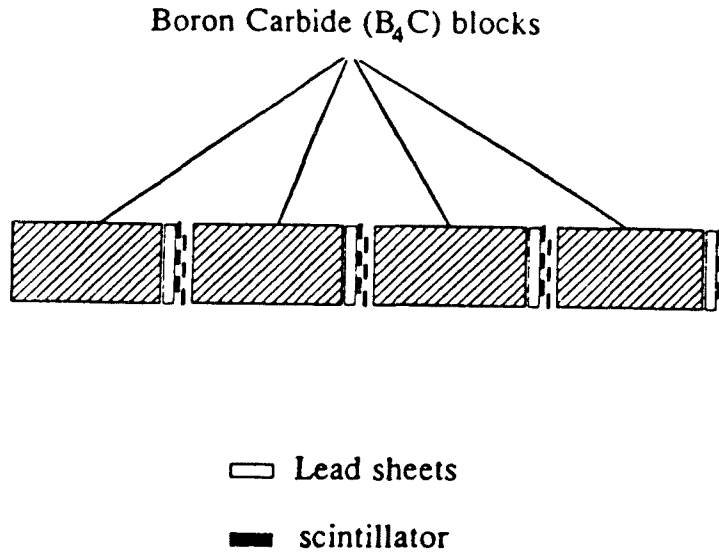


Figure 5. Schematic side view of the regenerator.

(Figure 5).

The scintillators made up the RA, or regenerator anti. The lead converted any photons produced in the regenerator blocks, allowing the RA to veto these events as well as events with charged particles produced from neutron interactions and K decays upstream of the scintillator.

Just upstream of the regenerator was the lead mask—a 5 cm thick sheet of lead 41 cm wide by 51 cm high with two 10 cm \times 10 cm holes for the beams. The purpose of the mask was to limit our acceptance of upstream decays; the holes in the mask were large enough that the mask did not define the beam profile. While there was no scintillator here, charged particles leaving the mask were detected downstream in the regenerator anticounter system. Even if charged π 's from an upstream K decay did elude the RA at the trigger level, we could still reject the event at the analysis level

since the pion trajectories would be changed by the scattering.

The fiducial decay volume for the kaons was fourteen meters of evacuated 1.2 m-diameter pipe just downstream of the RA. At the end of the decay volume were the trigger hodoscope and decay region anticounters (HDRA). (See Figure 6.) This package contained the V (or “veto”) counter, a plate of 0.96 mm scintillator 62 cm high and 50 cm wide. Behind this was a 0.1-radiation-length sheet of lead which could be rolled in and out of the beam depending on whether neutral or charged pion data were being taken, giving a 24% chance for one and only one of four photons from a $2\pi^0$ decay to convert. The T (or “trigger”) counter, identical to V in height and width but 1.39 mm thick, sat just behind the lead sheet. Including the wrapping as well as the scintillator, the V counter contained .0037 of a radiation length of material, while T contained .0051.

Downstream of the HDRA was the second magnet of the experiment, used as the separator for e^+e^- pairs in neutral mode as well as in glass calibration. We set this to give an estimated horizontal kick of 28.9 MeV/c in neutral mode to compensate for that given by the analyzing magnet. We did not use the separator at all in charged mode as the decay kinematics usually gave us adequate $\pi^+\pi^-$ separation.

Not far downstream of the separator magnet the vacuum pipe widened to a 1.8 m diameter. Fourteen meters further it terminated in a .0025 radiation-length thick, but extremely strong, vacuum window of 23-mil-thick Kevlar cloth attached to a 5-mil-thick sheet of mylar.

3.3 Spectrometer

The first chamber in the spectrometer was placed just downstream of the vacuum window. Although the chambers varied in size and number of wires, they were all of the same basic design: one vertical layer of sense wires spaced 1.3 cm apart, an identical

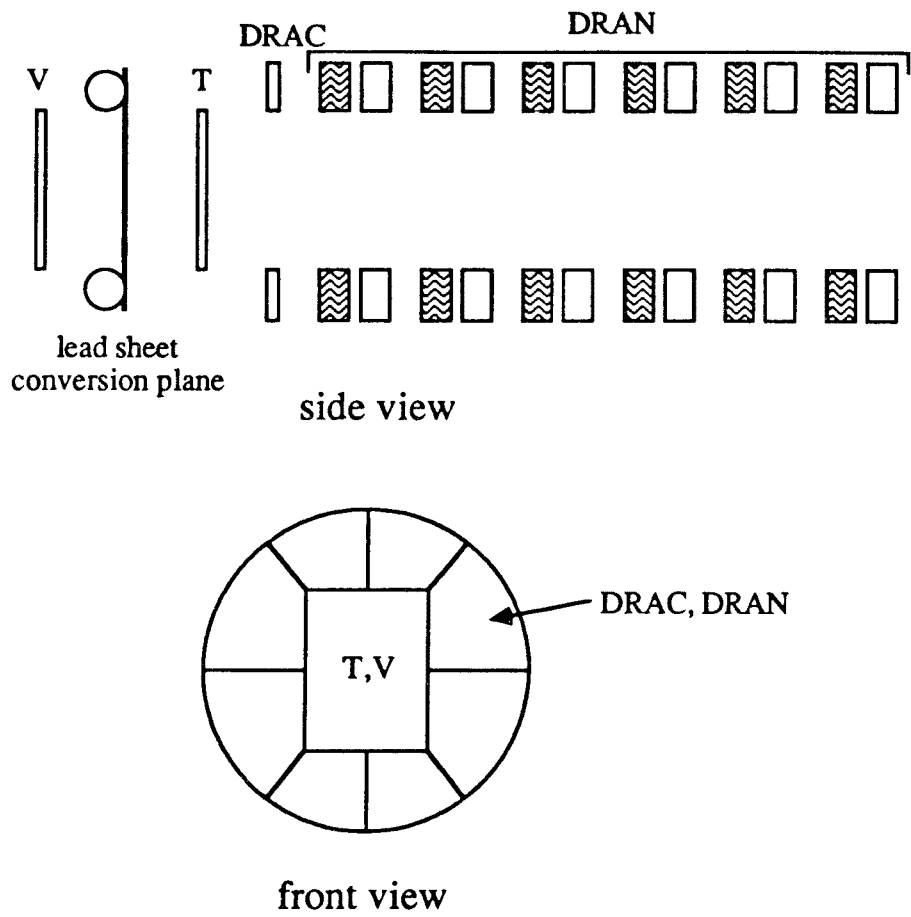


Figure 6. Schematic side and beam views of the HDRA components.

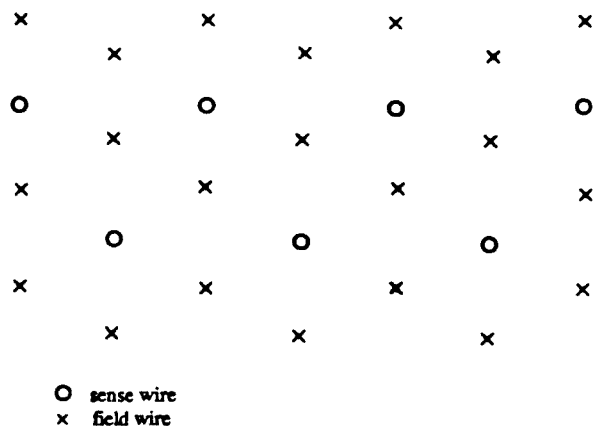


Figure 7. Drift chamber cell geometry.

layer offset by half of a cell spacing, and two similar horizontal planes (Figure 7). Such a cell geometry was designed to reduce chamber thickness and the multiple scattering associated with it. The chambers were filled with a gas mixture of 50% argon and 50% ethane to which was added 1/2% ethanol. The wire planes had typical position resolutions of about $150 \mu\text{m}$ and average efficiencies of 98%.

Downstream of the second chamber was the A bank, two rows each of twenty-four vertically oriented, 2 mm thick (0.0065 radiation length with wrapping) scintillators. The sixteen central counters in each row were 5 cm wide, while the outer four at the ends of each row were 10 cm wide. Each counter was 70 cm long, giving a total coverage of $1.6 \text{ m} \times 1.4 \text{ m}$. (See Figure 8.)

The analyzing magnet was a large dipole with an aperture 1.47 m high, 2.54 m wide, and 1.01 m deep. This aperture contained an aluminum box to support a helium bag; even with the box in place, though, the magnet gap was not a defining aperture. We operated the magnet to give a $0.1 \text{ GeV}/c$ kick in neutral mode and $0.2 \text{ GeV}/c$ in charged mode. These currents were chosen to give large enough kicks for good

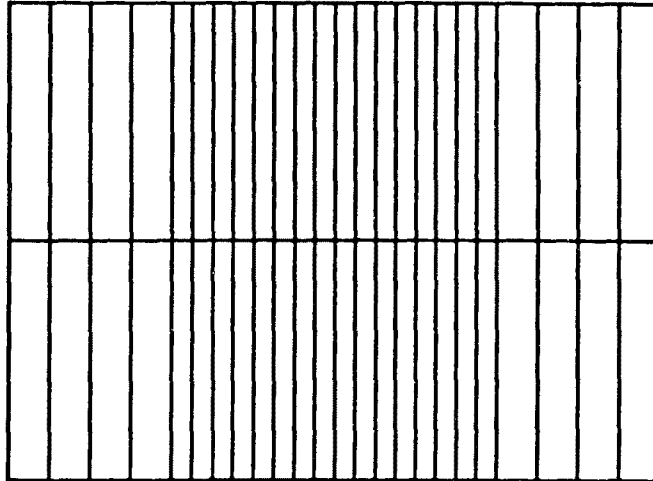


Figure 8. Schematic beam view of the A bank.

momentum resolution without bending the particles so far that they crashed into the box or missed the rest of the detector.

The second half of the spectrometer followed, with two drift chambers separated by a helium bag. These were followed by the B bank, thirty more scintillators arranged like those in the A bank. The B counters were thicker (1 cm), though, as well as larger: the eleven central counters in each row were 10 cm wide, while the outer four counters were each 17.5 cm wide. The counters were 90 cm long, giving a total size of 1.8 m by 1.8 m. (See Figure 9.)

3.4 Lead glass

The lead glass array was a key element in the neutral mode apparatus (Figure 10). The array was made of 804 blocks of Schott F2 lead glass, each measuring approxi-

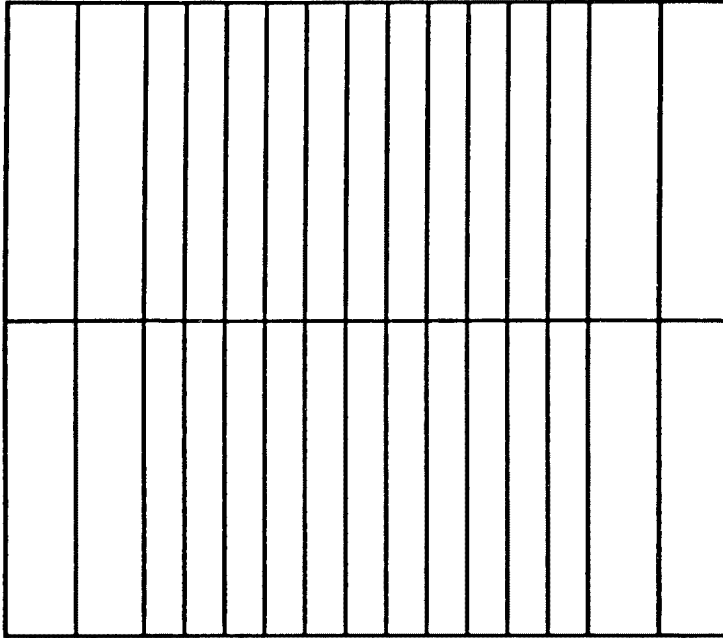


Figure 9. Schematic beam view of the B bank.

mately $5.81\text{ cm} \times 5.81\text{ cm} \times 60.96\text{ cm}$ (20 radiation lengths). The length was chosen large enough to reduce shower leakage from the back of the array (we retained 95-98% of the energy)¹⁴, yet small enough to show little attenuation of the light from the front of the block (and worse resolution). The block widths were chosen as a compromise between fine segmentation for good position resolution and coarse segmentation for ease of instrumentation. The blocks were stacked in a circular arrangement with two holes corresponding to the positions of the two beams. Each block was read out with an Amperex 2202 10-stage photomultiplier tube. Our light yield was approximately 700 photoelectrons per GeV. Each block also had a G10 mount glued to the front which held an optical fiber in place. The other end of the fiber bundles was mounted facing a xenon flasher, allowing us to monitor gain changes in the glass between the special

calibration runs, as well as to look for gain changes as a function of time into the spill. We found early in the run that the gains of about 1/3 of the blocks did change during the spill, some as much as 10%. For this reason we installed LED's whose light was transmitted by the fibers to provide a constant low level of light to mimic "beam on" conditions (about one photon every ADC gate). Keeping the tubes "on" in this way gave us much more uniform glass response. We had an overall glass energy resolution of $2\% + 6\%/\sqrt{E}$ (in GeV).¹⁴

Rather than attempt to seal each tube from room light, we placed the entire array inside a light-tight "house". This also facilitated control of the temperature of the block/photomultiplier tube pair, since rapid changes could cause the corners of the blocks to crack away from the tubes. In addition, the components in the phototube base were somewhat temperature sensitive and therefore so were the gains. Unfortunately it was not as easy to protect the glass from radiation damage. The four blocks between the beam pipes suffered the most damage, which was monitored as a decrease over the run of about 15% in the ratio of the average flasher response for the central four blocks to the average flasher response for the entire array.

In addition to the 804 blocks in the array itself, we had two blocks with full readout which sat in the glass house but out of the beams. These "reference" tubes were used to generate pedestals at a random frequency. This scheme allowed us to get a true measurement of the pedestal variation with time due to 60 Hz and other noise. Triggering in any way which used the 60 Hz line voltage could have given us misleadingly small pedestal variations if the same point on the oscillations of the ADC signal were sampled each time. The pedestal trigger was generated by putting a small source of Am^{241} near a block of sodium iodide ($\text{NaI}(\text{Tl})$) scintillator. The light from this scintillator was detected by the reference tube which signaled the data acquisition system

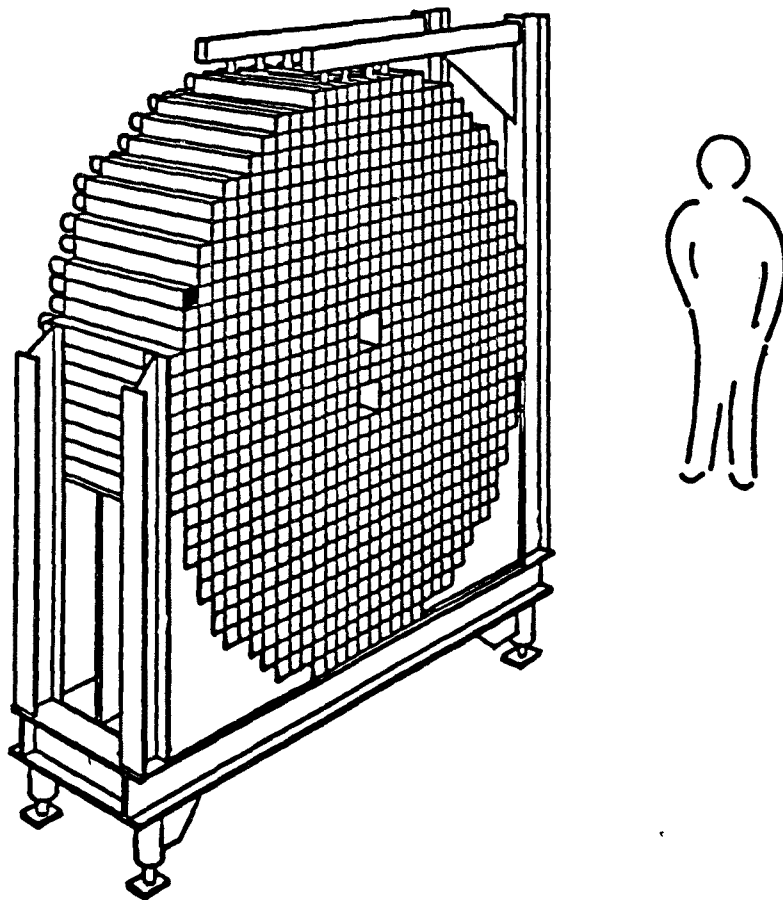


Figure 10. The E731 lead glass array.

to record pedestals.

3.5 Background rejection system

As discussed earlier, there were a number of detector elements designed to reject undesirable events. For the charged mode we had a lead curtain, 2.3 radiation lengths thick, placed just upstream of the B bank to reject electrons and photons from competing K_L decay modes. Holes were cut out at the beam positions to avoid high rates in the B bank from beam interactions. Rejection of muons from semileptonics and the beam spray was achieved by the use of a 2.3 m by 2.3 m scintillator bank of 23 counters behind about 3.3 m of steel (μ_2) as described above.

Recall that $K_L \rightarrow 3\pi^0$ events with missing photons were our major background in the neutral vacuum beam. Great care was taken to eliminate as many of these events as possible with the use of a whole system of veto counters. Photons from decays upstream of the sweeping magnet which had already left the beam pipe were converted and detected in the scintillator pinching anticounter (PA). To seal off the outer edges of the detector we used six planes of lead-lucite counters, the vacuum anti (VA), magnet anti (MA), and lead glass anti (LGA). (See Figures 11 and 12.) Each lead-lucite counter contained a total of 0.2 radiation lengths of lucite interleaved with 5.6 radiation lengths of lead. Showers in the lead from stray $3\pi^0$ photons spread into the lucite, where Čerenkov light was produced. Single sheets of scintillator upstream of the sandwiches indicated whether the entering particle was neutral or charged, *i.e.*, was a photon or not. Both the PA and the lead-lucite counters were supplied by the Princeton group and were designed to detect deposits of a few hundred MeV of energy. Light from these photon vetoes was collected with Amperex 2232B photomultiplier tubes. The light yield here was about 25 photoelectrons per GeV. Counters serving a similar purpose surrounded

the T and V counters: DRAC (scintillator) and DRAN (lead-scintillator sandwich).

Some attention also had to be given to the inner edges of the detector—the holes in the glass array. The back anticounter (BA) was a lead-lucite calorimeter placed behind the glass and centered on the beams in order to detect electrons and photons which missed the glass by traveling down the beam pipes. The segmentation of the BA was fine enough to allow some lepton/hadron differentiation in the analysis. (See Figure 13.) Finally, to tag events in which energy was deposited near enough to the holes in the glass that energy leakage could have occurred, we installed the CA, or collar anticounter, made of scintillator with a three-radiation-length copper converter. Suspended 1.3 m in front of the glass, each rectangle of counters was about 17.5 cm on each side with a hole 11.6 cm wide and 12.3 cm high in it, one for each beam. The bottom edge of the bottom rectangle was 5.4 cm above the top edge of the lower rectangle. The holes formed by the CA counters were therefore the same size as the holes in the glass, while the counters themselves covered a width of half of a glass block around the holes.

A reduction of the trigger rate in the neutral mode was achieved by the use of a lead wall placed just behind the glass. With between two and three interaction lengths of material (glass plus lead), many hadrons showered and were detected in another scintillator bank (μ_1).

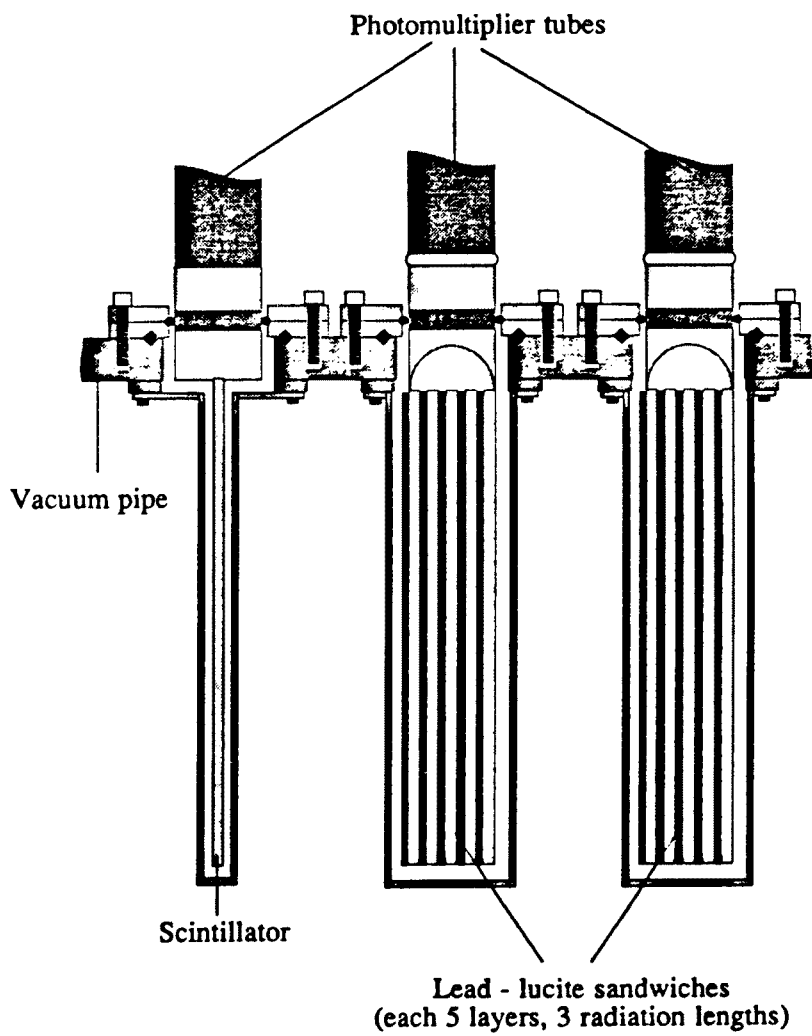
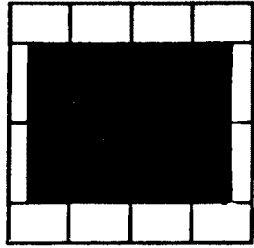
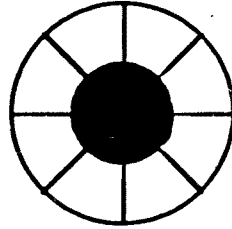


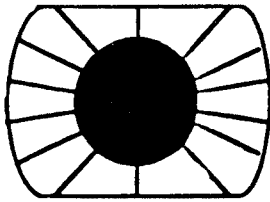
Figure 11. Schematic side view of Princeton lead-lucite counters.



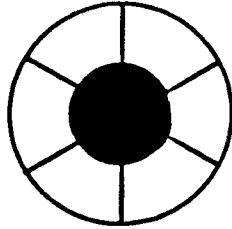
MA



VA3,4



LGA



VA1,2

Figure 12. Schematic beam views of the lead-lucite counters.

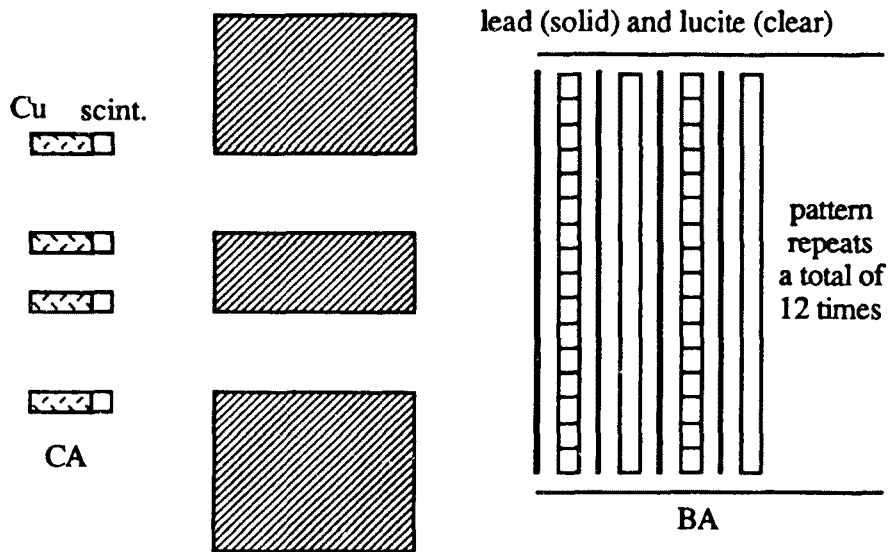


Figure 13. Schematic side view of glass hole region.

Chapter 4

TRIGGER AND DATA ACQUISITION

4.1 Charged mode

For $\pi^+\pi^-$ decays, the event topology was simple: two charged particles were seen in the decay volume with no activity in the RA and were bent in a magnetic field. The RA requirement helped to select kaons that had regenerated coherently, reducing the number of events in which an incident kaon or neutron scattered inelastically, knocking a nucleus apart and sending charged particles out of the regenerator blocks. We found that it was sufficient for the trigger to look for activity only in the six scintillators farthest downstream, which we called RA_{IV}. A subsequent decay of the kaon to charged pions in the decay volume was signaled by activity in the V plane. We chose to trigger on V rather than T just downstream to avoid triggering on events in which a neutron had interacted in V and sprayed particles into T. A veto on events with activity in the DRAC eliminated events which had charged particles outside of the aperture defined by T and V.

Decay kinematics alone usually gave us good angular separation for the π^+ and π^- in the horizontal x plane (bend plane for the analyzing magnet), so the separator magnet was kept off. We assumed that the parent kaon was headed down the center of the detector. (In reality there was a spread of about 1 mrad up and down.) Momentum conservation allowed us to require hits in both the east and west halves of the A bank (upstream of the analyzing magnet) and hits in both the east and west halves of the B bank. Because the B bank had an odd number of counters in each row, the two center

counters were included in both east and west side trigger logic. To ensure that single hits were not counted as good events, we demanded that at least two B counters had fired. The A and B bank requirements were tightened by additionally demanding no more than two hits in either bank to reject accidentals.

Some of the background rejection detailed in the design discussion was done at the trigger level. The lead curtain was rolled in for $\pi^+\pi^-\pi^0$ and $\pi e\nu$ rejection. Photons and electrons from upstream decays showered in the lead, giving large signals in the B bank. We vetoed events with signals greater than five times the signal obtained from a minimum ionizing particle. To take care of muons from semileptonic decays, as well as to cut two track triggers from dump muons and accidentals, we vetoed events in which there was a hit in the μ_2 bank. To further decrease the trigger rate, any event with hits in VA3, VA4, LGA, or PA scintillators was aborted at the final decision level before being written to tape.

A symbolic summary of the charged trigger is

$$\overline{RA_{IV}} \cdot V \cdot \overline{DRAC} \cdot (A_{EAST} \cdot A_{WEST}) \cdot \overline{3A} \cdot (B_{EAST} \cdot B_{WEST}) \cdot 2B \cdot \overline{3B} \cdot \overline{B5} \\ \cdot \overline{\mu_2} \cdot \overline{VA3_S \oplus VA4_S \oplus LGA_S \oplus PA}.$$

4.2 Neutral mode

For a good neutral mode decay, we had no charged particles upstream of the lead converter sheet but did have two tracks downstream of the sheet in the spectrometer. We then expected a fairly large energy deposit in the lead glass. These considerations gave us our basic trigger. The sheet conversion requirement was implemented using V to veto events containing charged particles upstream of the sheet and using T to trigger on particles downstream of the sheet. DRAC again vetoed any events sneaking around the edges of T and V. The splitting and reconverging of tracks in the neutral mode required

a different topology in the scintillator than we used for the charged mode. Since the A counter widths were small and the pair had been separated, we demanded two hits in the A bank, although we could no longer demand that they be in opposite halves. The converging geometry at the B bank and the larger counter widths meant that a good event could have tracks in either one or two counters. We again required that there be no more than two hits in either the A or B banks and no hits in the μ_2 bank.

In order to use the lead glass information in the trigger, we used special adder circuits to perform a fast analog sum of the signals from groups of seven to nine glass blocks. These sums were further combined to give a signal proportional to the total energy in the glass (E_T). This signal was discriminated inside the portakamp with a threshold corresponding to about 30 GeV in the glass. This was a conservative level as far as the desired neutral decays were concerned since our acceptance was small for kaons of such low energy.

The adders were also used to reject events at the final decision level in conjunction with a trigger processor which we called the mass box. The name came from its main task—to give a quick estimate of the invariant mass of the decaying particle, based on the expression

$$m_K^2 = \frac{E_T E_2}{z^2},$$

where $E_T = \sum E_i$ is the total energy in the glass, $E_2 = \sum E_i r_i^2$ is the second moment of energy, r_i is the radial distance from the center of the array to the center of the shower, and z is the distance from the decay vertex to the lead glass. The construction of the E_T signal using the adders was described above; we made E_2 in a similar way. We considered r_i to be expressed in units of the glass array radius, giving r_i all less than 1, and then used resistive dividers to attenuate the signal from each adder by the appropriate amount.

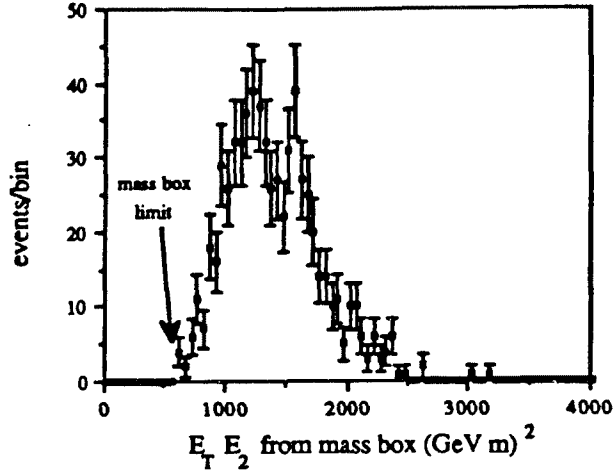


Figure 14. $E_T E_2$ calculated by the mass box for good $K_L \rightarrow 3\pi^0$ decays.

The mass box threshold was also set conservatively to an effective $E_T \cdot E_2$ of 600 (GeV m)². Figure 14 shows how this cut compares with $E_T \cdot E_2$ for good $K_L \rightarrow 3\pi^0$ events. One reason for the conservative threshold here was the anticipated difficulty of understanding the effects of the mass box on the acceptance. Another was the imperfect gain-matching of the glass; only two thirds of the blocks had gains within 10% of the peak value, and the remaining blocks tended to have lower gains. A third consideration was the non-negligible length of the decay volume. For the same energy pattern in the glass, the calculated K mass could vary by 50% depending on the distance from the decay vertex to the glass.

Further background and trigger rate reductions were achieved by using PA, RA_{IV}, and μ_2 in veto, just as in the charged mode. To eliminate stray hadrons we required that the μ_1 bank have a total pulse height corresponding to fewer than five minimum ionizing particles.

This, then, is a symbolic summary of the neutral trigger:

$$\overline{PA} \cdot \overline{RA_{IV}} \cdot \hat{V} \cdot T \cdot \overline{DRAC} \cdot 2A \cdot (\geq 1B) \cdot \overline{(3A \oplus 3B)} \\ \cdot (E_T > 30\text{GeV}) \cdot \overline{\mu_2} \cdot (\mu_1 < 5\mu) \cdot (\text{mass box OK}).$$

It should also be noted that charged, neutral, flasher, and $B \cdot \mu_2$ triggers were only accepted after the “beginning of spill” and before the “end of spill” signals provided by the laboratory; pedestals were accepted between spills.

4.3 Data acquisition

The data acquisition hardware was fairly traditional: we used CAMAC readout directed by a PDP-11/45 running the Fermilab MULTI data acquisition package. In addition to responding to charged and neutral mode triggers, the system also wrote prescaled (usually 2^{16}) triggers of $B \cdot \mu_2$ events for monitoring chamber positions and calibrating and monitoring various counters. Pedestals were gated only between spills and came at a frequency of about 1 Hz. The flasher was gated by a pulse generator about once per second during the spill. The accelerator beginning-of-spill signal gated scalers which recorded singles rates of trigger counters as well as the trigger rates themselves.

The mass box decision information was read directly through CAMAC. Hits in all of the scintillators were tagged in latches. The up/down status of the regenerator and absorber was also stored. We digitized the adder signals, E_2 , and the signals from the phototubes looking at the BA lucite in LeCroy model 2285 12-bit ADC's, while the lead glass, CA, E_T , and the reference tube signals used a 15-bit version. These ADC's had a sensitivity of about 33 counts/pC; a minimum-ionizing muon depositing 2/3 GeV in the glass gave a signal of typically 200 counts. The linearity of each ADC module was verified over the full operating range prior to installation. The 100-ns gate for the adder/BA ADC's was shorter than the 250-ns lead glass ADC gate so that the

adders might be used later in rejecting out-of-time clusters from accidentals in the glass. Signals from the lead-lucite counters, DRAN, and μ_1 were also digitized at a reduced, though adequate, sensitivity of 0.25 counts/pC in LeCroy model 2249 ADC's; a 25 ns gate width was used here. A minimum-ionizing muon deposited energy equivalent to a 100 MeV energy photon. These signals were about 50 counts above pedestal. Digital chamber information was obtained using LeCroy 4291B TDC's in four crates, each containing a 4298 crate controller as well. There was a master controller (model 4299) in addition. The TDC system was operated in common stop mode, which stored the hit wire number and also the time between the signal on the wire and the trigger in 1 ns bins. (Maximum drift times were about 250 ns.) The PDP-11 stopped writing chamber data after 250 words and proceeded with the next event. The end-of-spill events contained the information from the scalers which had been summed over the spill.

MULTI gave us the ability to monitor event displays and histograms of the performance of any section of the detector: lead glass pedestals and flashers, frequency of hits in trigger counters, and chamber time and wire hit distributions were studied online for every run.

4.4 Data collection and samples

When the accelerator was running well, it delivered 10^{12} protons per twenty second spill on target. At this intensity our data logging was limited by a dead time of about 40% to 3000 neutral triggers or 7000 charged triggers per spill.

Of our more than 800 magnetic tapes of data, we chose to use just over 500 of them for the final analysis. The earlier tapes were written as both the Tevatron and our apparatus were coming up; these tapes may have added biases which would not

have been easily understood and so were rejected. Since it took us so much longer to gather the statistics-limiting $K_L \rightarrow 2\pi^0$ decays, we spent more time in neutral mode than in charged, interspersing the latter at three intervals. After six weeks of useful data-taking, we ended up with 2.5×10^7 neutral and 7×10^6 charged triggers on tape.

In addition to the 2π decay events, we needed to collect events for glass calibration, which we did using specially created e^+e^- pairs which we momentum-analyzed in the spectrometer and tracked to the glass. To create a beam with a softer momentum spectrum than we had for regular data-taking, we used a one-interaction-length copper target instead of our usual beryllium target. Replacing the lead in the beam plugs with an extra 1.2 m of beryllium gave us a photon beam with little hadron contamination. The beam photons were converted to e^+e^- pairs by a beam profile display monitor of 5-mm-thick copper upstream of our apparatus. The converter sheet in the HDRA was removed. Different combinations of currents in the sweeper and separator magnets were used to spray the electrons over all but the outermost blocks of the glass array, with many blocks receiving electrons of several energies. About 40% of the blocks received more than 100 electrons over the whole calibration run. We repeated this procedure once per week during stable running for a total of six sets of calibrations.

The chamber equivalent of the glass calibration was the $B \cdot \mu_2$ run with the analyzing magnet off. These straight-through events were used for alignment as well as chamber plane efficiency studies and were usually taken once per shift.

Chapter 5

ANALYSIS OF EVENTS

5.1 Chamber alignment

Before we began with the charged track finding and reconstruction, we had to determine the chamber positions. This was done by survey before and after the run and by software in between. The positions of chambers 1 and 4 (numbered from upstream to downstream) were assumed to be well-known. Tapes of the $B \cdot \mu_2$ straight-throughs were used to determine the relative position offsets of chambers 2 and 3 by calculating the mean residual between the reconstructed position of a hit and the projection of its track to that plane. Rotations in the xy plane were measured by the change in residual as a function of position along the wire. (For future reference it should be noted that our coordinate system was chosen with $x=0$ and $y=0$ at the center of the glass, with y positive up and x positive to the west (or beam left). The target position defined $z=0$, with z increasing in the direction of the beam.)

5.2 Finding tracks

The basic track finding algorithm will now be described; any variations on this basic scheme for, say, neutral tracking rather than charged will be indicated at the appropriate places in the discussions of the specific reconstruction analyses. After eliminating all hits with differences between the time of the common stop and the hit on the wire greater than 250 ns or less than 10 ns, we began to look for tracks in the x view planes upstream of the analyzing magnet. Track candidates were identified by choosing all

possible pairs of track endpoints from the first (most upstream) x plane of chamber 1 and the first x plane of chamber 2, the first x plane of chamber 1 and the second x plane of chamber 2, and the second x plane of chamber 1 and the second x plane of chamber 2. Each point was assigned an x position corresponding to the wire position in space including transverse offsets but not rotations, *etc.* Z positions of tracks were assigned to be just the z position of the particular plane containing the wire. A fit was done to determine the slopes and intercepts of the tracks. These upstream track candidates were then extrapolated back to the plane of the HDRA where they were required to be within 30 cm of the center of the hodoscope in x , about 5 cm wider than the T and V counters on each side. Downstream tracks were found similarly but were required to extrapolate to positions at the plane of the glass which were inside the glass array ($|x| < 1$ m). In addition, the projection of the downstream track to the magnet center had to be within 3 cm of the projection of an upstream track. Hits from the other planes were associated with the track if their x positions as calculated above were within 1.5 cm of the projected track positions. In the cases where there were two or more hits per plane which fell within the “road”, the hit which gave the best “sum of times” was chosen. Hits in at least three planes of the possible four were required for a good track.

We then made corrections to the hit positions for the drift distances. A look-up table provided the time to distance conversion for each 1 ns of drift time from 0 to 250 ns for a given plane. Recall that the second wire plane in each direction was offset to allow us to determine from which side of the wire the drifting electrons had come. We used the x positions of hits in these complementary planes relative to those in the other planes to decide the direction of the drift distance correction. For some tracks there was no complementary plane information; the unpaired hit was then used to give two possible tracks, one for each possible sign of the drift distance. After the time

information was included, the tracks were refit to all of the hits using a least squares method to get track slopes, intercepts at the target, and s^2 's, where s^2 was a measure of the track quality:

$$s^2 = \frac{1}{(N_{hits} - 2)} \sum_{z \text{ or } y \text{ hits}} (x, y_{hit} - x, y_{projected})^2.$$

Upstream and downstream track lists were compressed by eliminating redundant tracks, defined as those whose slopes differed from another track's slope by less than 10^{-5} and whose intercepts differed by less than 10^{-3} .

Once all of the upstream and downstream segments were found, we had to match them up to give a complete track. A "meeting-in-the-magnet" offset was calculated for each possible pairing of upstream segments with downstream segments; those with separations greater than 1.5 cm were rejected. When two tracks shared hits, we kept only the track which gave the smallest separation. Events without two matching tracks were rejected.

Finding y tracks proceeded in much the same way as finding x tracks. Since the y tracks were essentially straight through the spectrometer, all eight planes were used for each track. Pairs of points were again used to give track slopes and intercepts. Tracks had to point to within 36 cm of the HDRA center, about 5 cm above and below the T and V edges, as well as within the lead glass array height (1 m). Hits were again associated with tracks if they fell within a 1.5 cm road. Because the y tracks could be very close together, especially in the neutral mode where the y separation was caused only by multiple scattering in the lead, a slightly different algorithm was used to determine which of several consecutive hits to use. In the case where the complementary plane had only one hit, the correct hit could be chosen from the sum of times, as in the x view. When there were two or more complementary hits, we calculated the sum

of the residuals for the hit and its complement on one side of the wire and compared it with the sum from the hits on the other side, choosing the pair with the smaller sum. If no complementary information at all was found, we chose the hit which gave the smallest residual. Y -view tracks were required to have hits in at least five of the eight possible planes. Time information was then used to adjust the y coordinates with complementary plane hits as it was in the x view, and lines were fit through all of the points with the time correction. Time information was assigned to single hits depending on the direction of the point from this best fit line. After all single hits had been accounted for, the tracks including all points were refit to give track parameters as above. The y track list was reduced by looking for tracks which shared hits. We kept the tracks which had the most hits or had the smallest χ^2 if the number of hits in each track was the same.

5.3 Charged mode: $K \rightarrow \pi^+\pi^-$

The analysis of the charged data was done in three steps. The first pass analyzed the raw data tapes. Events for which tracks could be found and which passed certain loose cuts were written to summary tapes. On the second pass we analyzed the events again, employing more stringent cuts. Information from events which survived these cuts was stored in condensed form on another set of summary tapes. Events from these tapes were further analyzed to give the final data set.

The first cut in the raw data analysis rejected events in which the absorber and regenerator were not in the same beam, as this only occurred if either the absorber mover or the regenerator mover malfunctioned. Hitting the regenerator alone with the full beam would have given a very high event rate in the spectrometer, possibly accompanied by drops in chamber efficiency and phototube base performance. Hitting

only the absorber would not have given us the same $K_L - K_S$ mixture as in other events.

After eliminating events with more than 145 hits in the chambers, we used the basic track finder described above. If we obtained two tracks in each view the tracks were refit, this time taking into account chamber rotations, offsets, the signal transit time along the chamber wire, and the light pulse transit time in the B bank counter which defined the trigger timing. In addition, separate upstream and downstream y tracks were fit for those halves of the track which had more than three hits.

Next the pion momenta were calculated based on the bending of the tracks in the analyzing magnet. The sum of the momenta of oppositely charged particles gave us the kaon momentum, while the sum of the pion energies gave us the kaon energy. The energy and momentum then gave us the kaon mass. Events in which the particles had the same sign of charge were discarded.

We obtained the decay vertex from pointing the x and y upstream tracks back to their point of closest approach. The decay vertex and the direction information from the momentum of the kaon allowed us to determine where the kaon left the regenerator. A comparison of the kaon's direction after traversing the regenerator with a line from the target to the exit point gave the transverse momentum kick. (See Figure 15.)

At this point we saved all events which satisfied loose kinematic cuts. We required that:

- 1) the kaon mass reconstructed to between 400 and 600 MeV/c^2 ,
- 2) each track had momentum of at least 5 GeV/c ,
- 3) the kaon energy fell between 15 GeV and 200 GeV ,
- 4) the decay vertex fell between 90 m and 150 m from the target (from upstream of PA to downstream of VA3), and
- 5) there was no activity in any of the RA counters. (See Figure 16.)

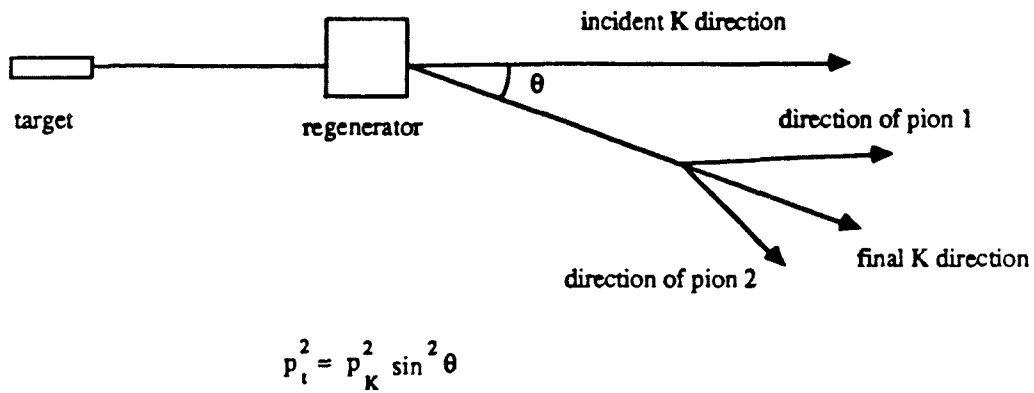


Figure 15. Finding p_t^2 for a charged decay.

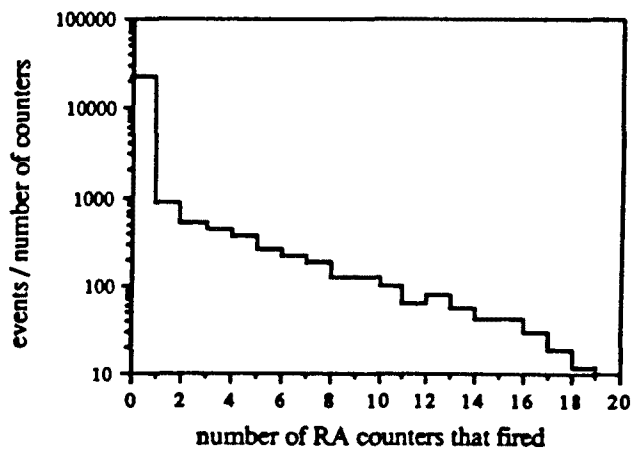


Figure 16. Number of RA counters hit per event. Plotted are events for which the absorber and regenerator were in the proper positions and for which exactly two z tracks were found.

The second pass of analysis was a little more thorough. Notice that in the first stage of the analysis no attempt was made to match the z - and y -view tracks. Here we

did the matching as follows: After the kaon direction was found, we compared the kaon's calculated vertical position at the target with the vertical position of the target itself. The x - y track pairings were swapped and the procedure was repeated. We took the true pairing to be that which gave a target position closest to the true value. We could have used the struck A or B counters to give us this matching for many charged mode events, but this method only worked if one pion struck the upper half of the scintillator bank and one struck the bottom. We did not record the lead glass energies for charged mode, although we did save the adder information. To use the adders for matching, the pions would have had to deposit enough energy in the glass to be seen reliably in the adders (which attenuated the glass signal by a factor of 5). Hadron showers were typically more spread out than electromagnetic showers and so would share energy among several adders. We would also have eliminated events in which an adder was inefficient or two tracks were close together and shared an adder. We preferred the y target position matching scheme because it allowed us to choose a pairing for every event.

Once we had the proper pairing, we could make more stringent cuts on the data. First were the aperture cuts. As we shall see below, the phase analysis depended on a good understanding of the detector as modeled by a Monte Carlo simulation. We therefore cut away from edges to ensure that the data and the Monte Carlo events had equivalent cuts. Charged pion candidates were required to fall within a circle of 1.17 m diameter at the plane of the vacuum window, and therefore within the window and not the flange holding it in place. (See Figure 17; in this and following figures, the arrows indicate the positions of the cuts.) Tracks at the A bank had to be more than 2.5 cm from the edges of the bank (Figure 18), while at the B bank they were required to be within a radius of 86.5 cm of the center of the bank (Figure 19). When projected to

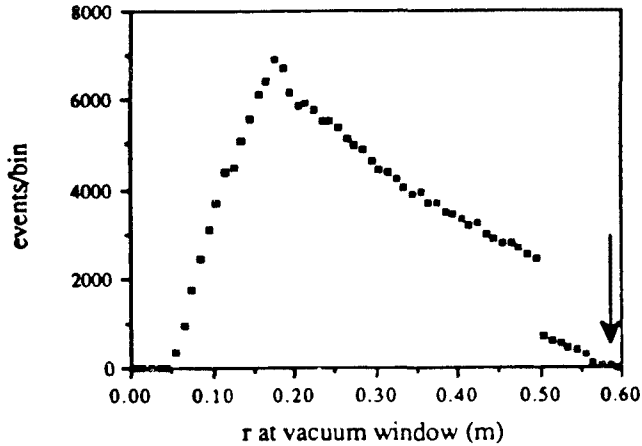


Figure 17. Distance of pion track from center of vacuum window. These events satisfied the first pass analyses and had exactly two tracks. The sharp drop at $r = 0.5$ m comes from the limiting aperture of the glass. The cut applied is indicated by the arrow.

the glass, this corresponded to a ring about one block from the outer edge of the array. At the upstream end of the spectrometer, aperture cuts were made on the position of the K at the regenerator to make sure there was no spillover between beams. The same cut was applied at the mask aperture to eliminate any events decaying upstream of the regenerator in which the pions scattered in the mask. Kaons were restricted to regions with $-0.0536 \leq x_{reg} \leq 0.048$ and either $-0.1368 \leq y_{reg} \leq -0.0352$ or $0.0162 \leq y_{reg} \leq 0.1178$, which cut only into the tails of the beams (Figure 20).

Another set of cuts was imposed to reduce the background from Λ^0 , semileptonic, and $\pi^+\pi^-\pi^0$ decays. If the reconstructed kaon energy was greater than 130 GeV, a $\Lambda^0 \rightarrow p\pi$ decay was suspected. (Λ 's with lower energy than this aren't seen in the detector since they decay much farther upstream and the pion misses our apparatus.) The event was reanalyzed assuming that the more energetic track belonged to a proton (or antiproton). We then calculated the energy of the parent " Λ^0 " as well as its mass.

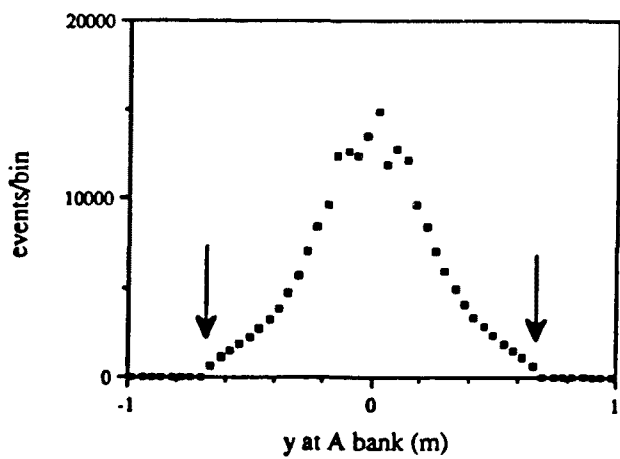
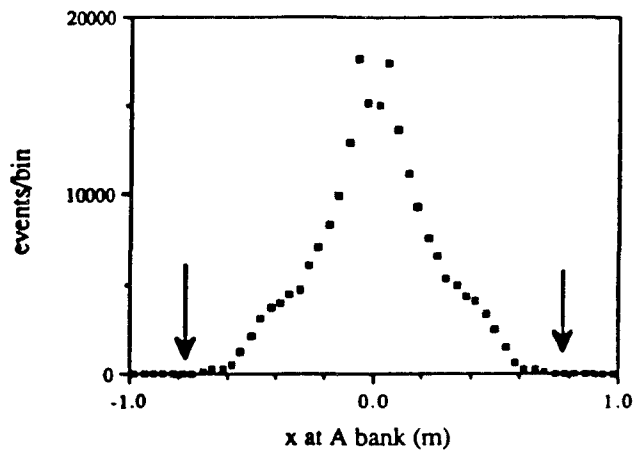


Figure 18. Aperture cuts on tracks at the A bank. These events satisfied the first stage analyses and had exactly two z tracks.

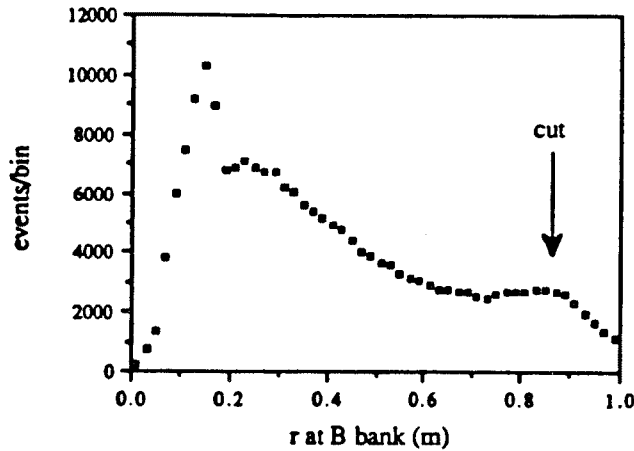


Figure 19. Aperture cut on tracks at the B bank. These events satisfied the first stage analyses and had exactly two x tracks.

Any events which had invariant masses within 10 MeV of the Λ^0 mass ($1.105 \text{ GeV}/c^2 < m_{\Lambda} < 1.125 \text{ GeV}/c^2$) were discarded (Figure 21). To eliminate any $K \rightarrow \pi e \nu$ decays which were not vetoed by the $\overline{B5}$ trigger requirement because the electron went through the holes in the lead curtain, an aperture cut for tracks was made at the B bank. The cut rejected events in two regions 13 cm wide and 13.2 cm high with a 9.6 cm strip of lead separating them (Figure 22). Remaining $K \rightarrow \pi \mu \nu$ decays were eliminated by requiring each track to extrapolate to the μ_2 bank center within 80 cm in x and 110 cm in y (Figure 23). This was nearly 2/3 of the width of the bank and the entire height. Each track was also required to have more than 10 GeV/ c momentum to eliminate events in which a low energy muon ranged out in the steel muon filter and went undetected in the scintillator (Figure 24).

Cuts were also made on track quality and topology. Because the momentum and direction of the kaon were calculated using only track information, it was important to have well-defined tracks. A cut of 2.5×10^{-7} on the track residuals s^2 defined above

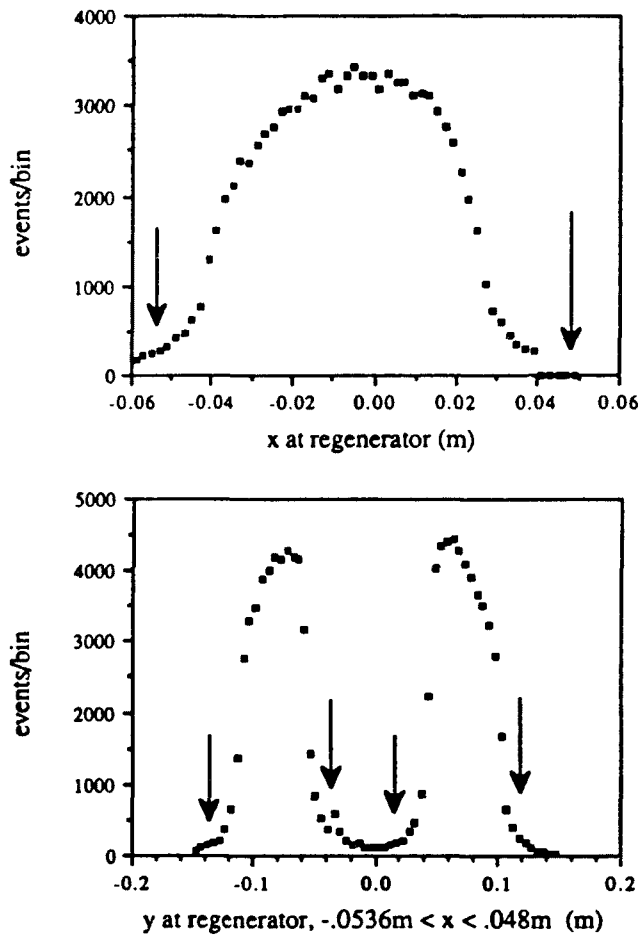


Figure 20. Aperture cuts for kaons at the regenerator. These events satisfied the first stage analyses and had exactly two z tracks. Note that no p_t^2 cuts have been imposed up to this point; doing so gives beam profiles which are clearly separated.

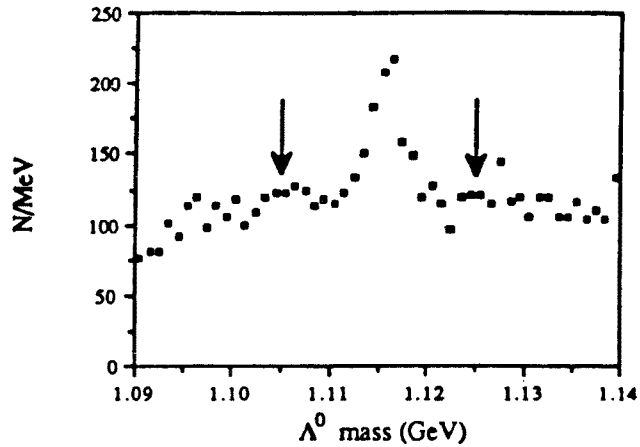


Figure 21. Invariant mass of “ $p\pi$ ” for kaon energy > 130 GeV. These events satisfied the first stage analyses, had exactly two α tracks, and passed the aperture cuts described in the text.

was imposed on each upstream and downstream half of a track in each of the two views (Figure 25). The distance of closest approach of upstream tracks was calculated and divided by the distance between the reconstructed vertex and chamber 1. This weighting made allowance for inaccuracies in extrapolation due to chamber resolution and multiple scattering; events which had a large extrapolation were allowed a larger separation at the decay vertex than events with a smaller extrapolation. We took the distance of closest approach to be the decay vertex. If the tracks were too far apart they might not have been from a kaon decay or could have been badly scattered, in which case our momentum determination would have been degraded. This weighted distance of closest approach had to be within 3 standard deviations of zero, where the standard deviation was defined as

$$\sigma_{del} = .245 \times 10^{-4} + .0085 \left(\frac{1}{p_1^2} + \frac{1}{p_2^2} \right)$$

(Figure 26). The momentum dependence here came from the deflection expected from

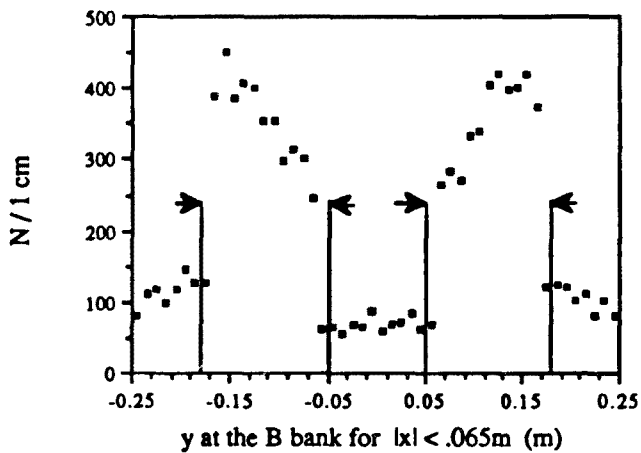
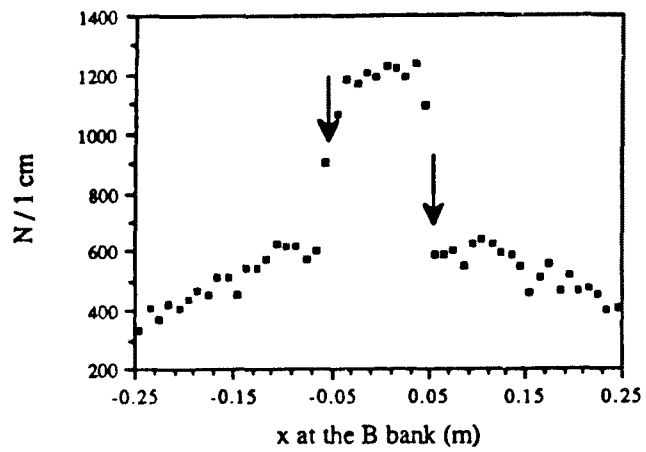


Figure 22. Aperture cuts on tracks at the B bank in lead curtain hole region. These events passed the first stage analysis and had exactly two z tracks.

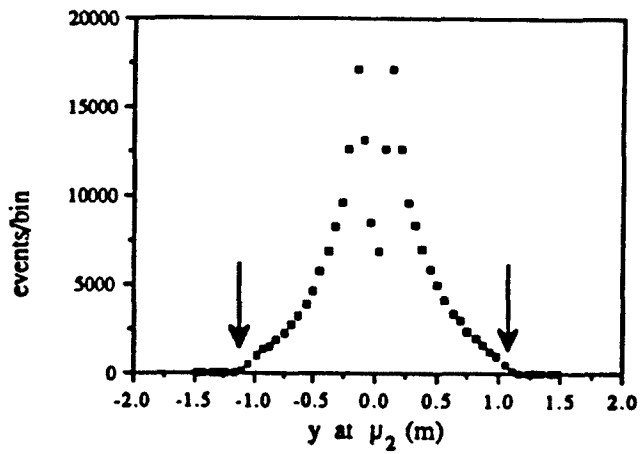
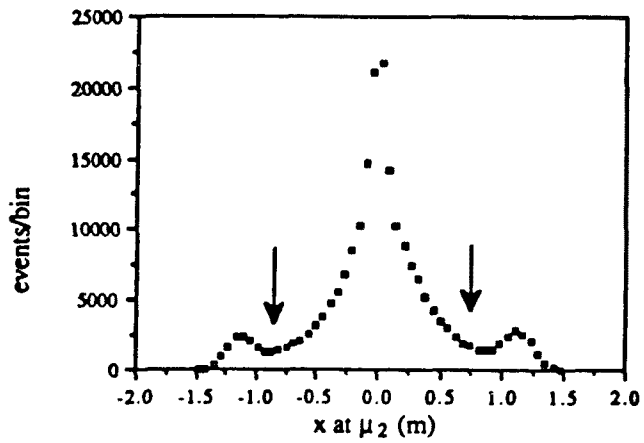


Figure 23. Aperture cuts on tracks at the μ_2 bank. These events passed the first stage analyses and had exactly two z tracks.

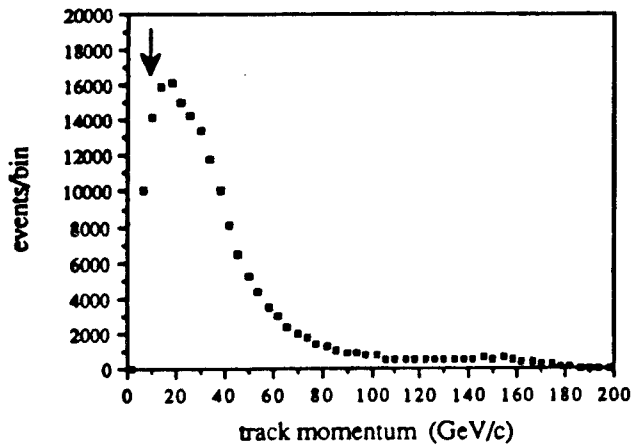


Figure 24. Momentum of pion tracks. These events passed the first stage analyses and aperture cuts and had exactly two z tracks.

the multiple scattering of two particles with independent trajectories. The constants were determined empirically.

The meeting-in-the-magnet track offsets were also compared to a momentum-dependent cut, this more stringent than that imposed by the track finder. Here

$$\sigma_{\text{offset}} = \left(220 + \frac{2700}{|p|} \right) \times 10^{-6},$$

and we required the track coordinates to match to within three σ_{offset} in each view (Figure 27). The momentum dependence here again reflected the effects of multiple scattering, this time of a single particle. As above, the constants were determined from the data.

Since the summary tape production cuts were fairly extensive, little additional analysis was needed at the final level of event selection. Here a cut on transverse momentum (p_t) was applied, since we were interested in only coherently regenerated kaons from the regenerated beam. (Coherent scattering was assumed when we added

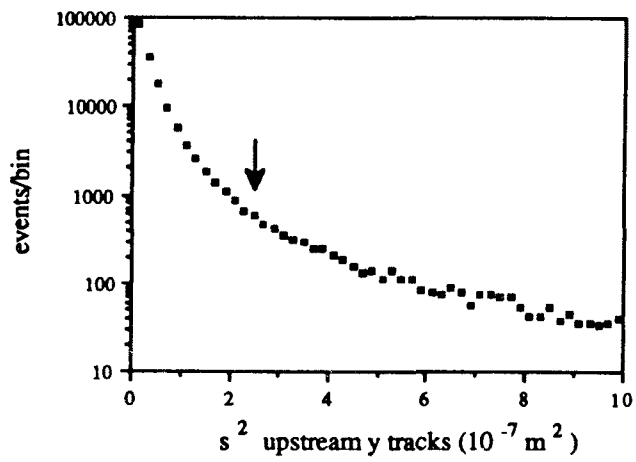
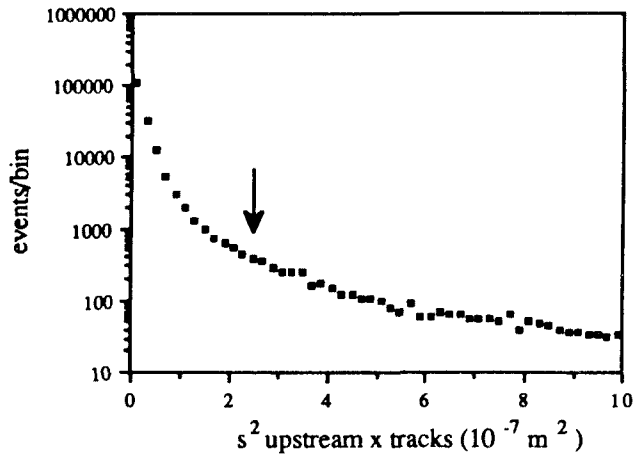


Figure 25. Track s^2 for upstream x and y views. These events passed first stage and aperture cuts and had exactly two x tracks.

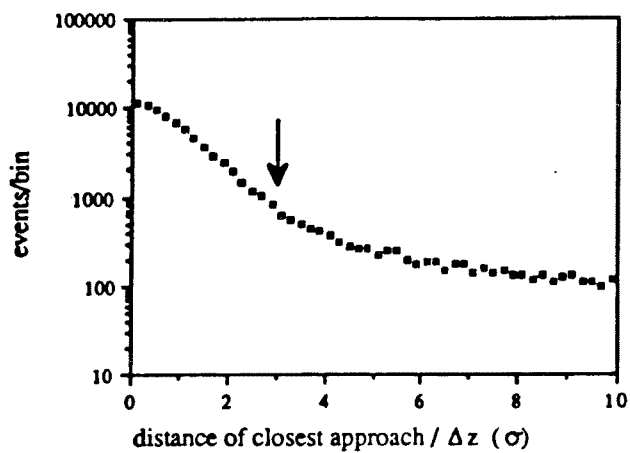


Figure 26. Weighted distance of closest approach/ σ_{dcl} for events which passed first stage and aperture cuts and had two x tracks.

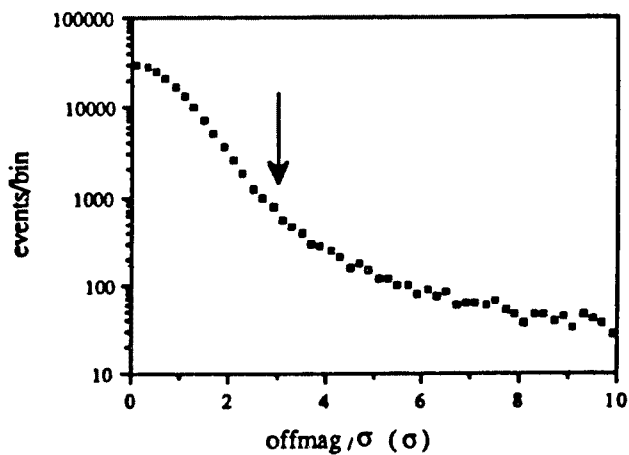


Figure 27. Meeting-in-the-magnet track offsets/ σ_{offset} for events which passed first stage and aperture cuts and had two x tracks.

the K_L and K_S amplitudes in determining the decay distribution as a function of proper time. Incoherent scattering processes do not have the same regeneration amplitudes as coherent ones and are not as easily calculable.) We eliminated most of the background from inelastic and diffractive regeneration (K scattering from one nucleus instead of the entire regenerator) by discarding events with high p_t . We find (Figure 28) that rejecting events with $p_t^2 > 250(\text{MeV}/c)^2$ rejected more background than signal while affecting K_S and K_L equally. (This was especially important for the ϵ'/ϵ measurement.) A tighter mass cut, to eliminate misreconstructed kaons, was also imposed: $484 \text{ MeV}/c^2 < m_K < 512 \text{ MeV}/c^2$ (Figure 29). We had tuned our magnet calibration to give us the correct value for the K mass; we then used the reconstructed Λ^0 mass as a check on the charged mode energy scale. Our value for the Λ^0 mass is in good agreement with the accepted value of $1115.60 \text{ MeV}/c^2$, as seen in Figure 30.

For the phase analysis we imposed a decay vertex cut of 124 m to 137 m (Figure 31) and a cut of 30 GeV to 130 GeV on the kaon energy (Figure 32). The vertex cuts were imposed because of the difficulty of understanding the smearing of events into unphysical regions of the decay volume. The high end energy cutoff allowed us to neglect K_S in the vacuum beam that were generated at the target, while the low end cutoff reflected our falling acceptance at lower energies. As seen in Figure 29, some background remained in both K_L and K_S data. The treatment of this background will be described following a discussion of the $K \rightarrow \pi^0 \pi^0$ analysis.

Table 2 gives the number of events after this level of analysis from each of the charged data sets for the regenerated and vacuum beams. Recall that we collected our charged data at three intervals. In the interim, we found that the beam collimator positions had changed slightly between sets, changing the beam profiles. This difference was noticeable, so we handled each data set individually.

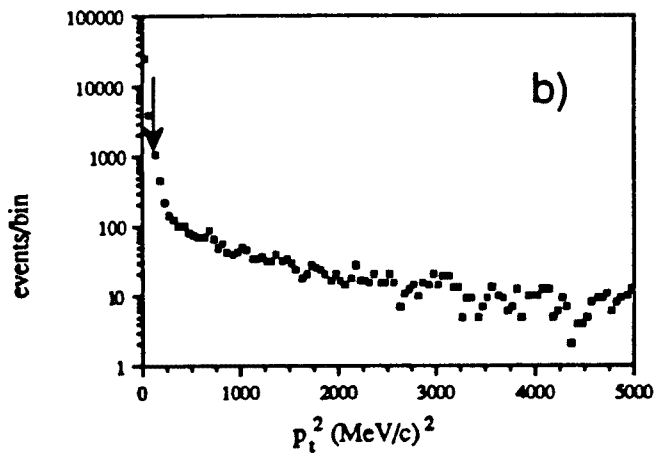
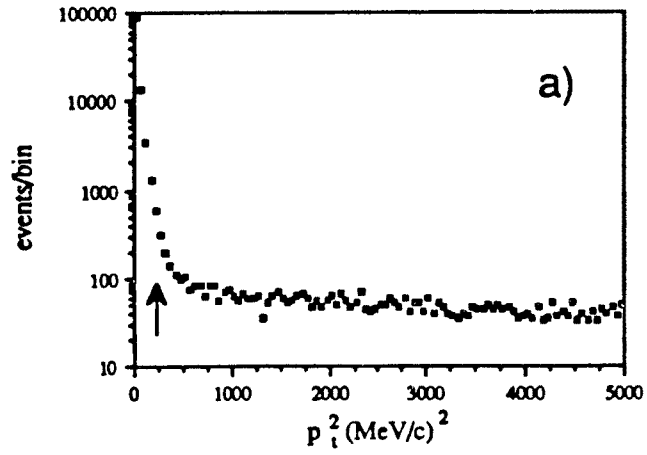


Figure 28. Reconstructed p_t^2 for charged decay events, a) regenerated beam, b) vacuum beam. These events passed all cuts except p_t^2 .

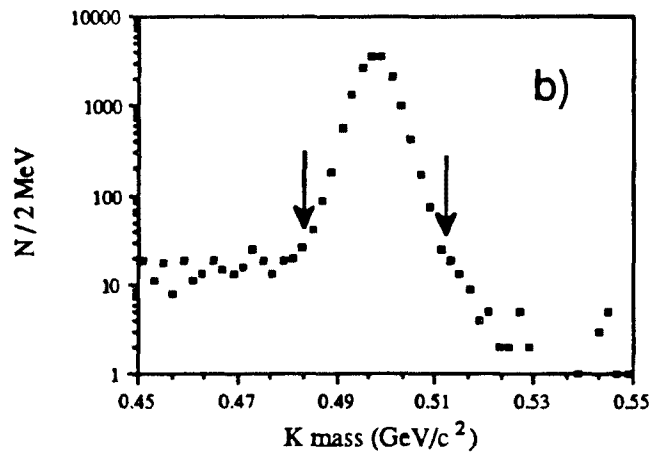
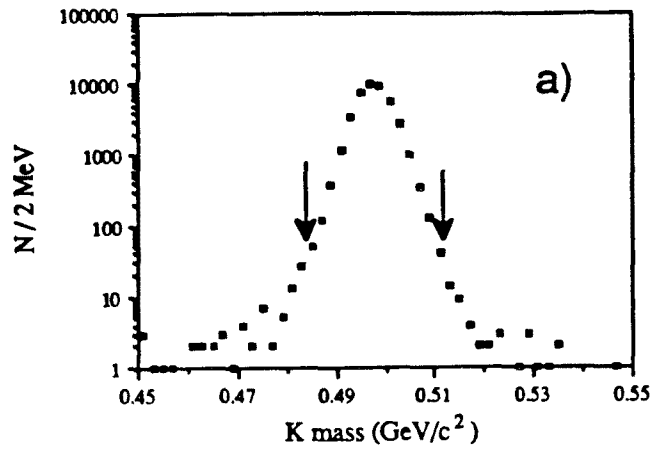


Figure 20. Reconstructed kaon mass, a) regenerated beam, b) vacuum beam.

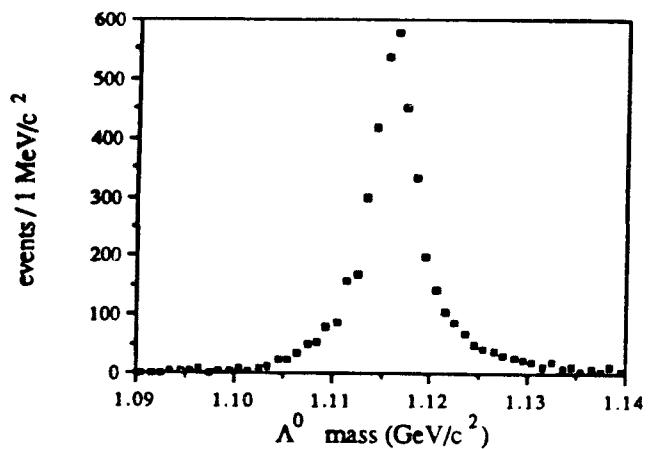


Figure 30. Λ^0 mass after separate analysis.

Table 2. Number of charged mode events after all cuts.
No background subtraction has been done.

data set	regenerated beam	vacuum beam
1	29846	8777
2	38064	14115
3	42494	15885

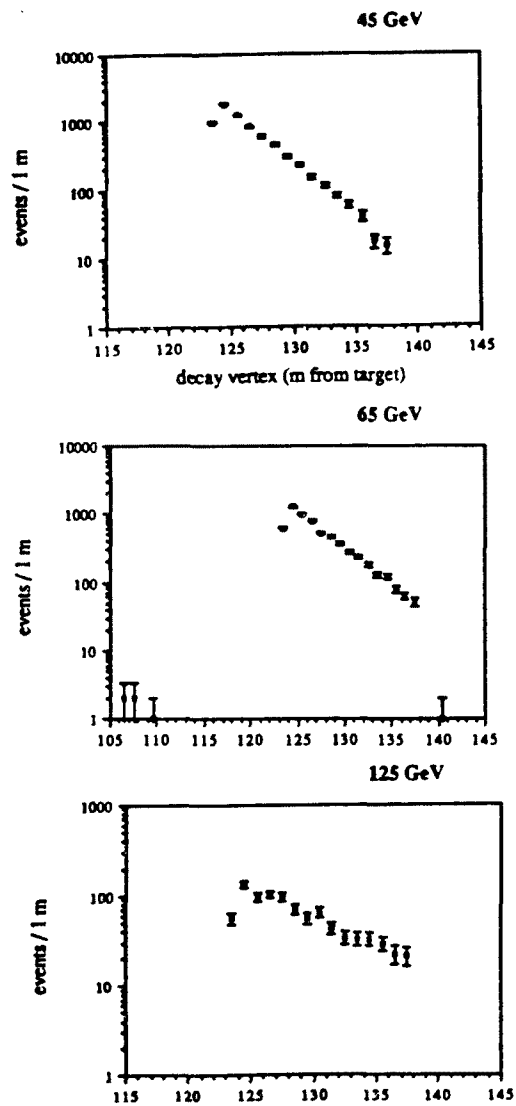


Figure 31. Decay vertex distributions from the regenerated beam at three representative energies. These events, taken from the last charged data run, passed all cuts.

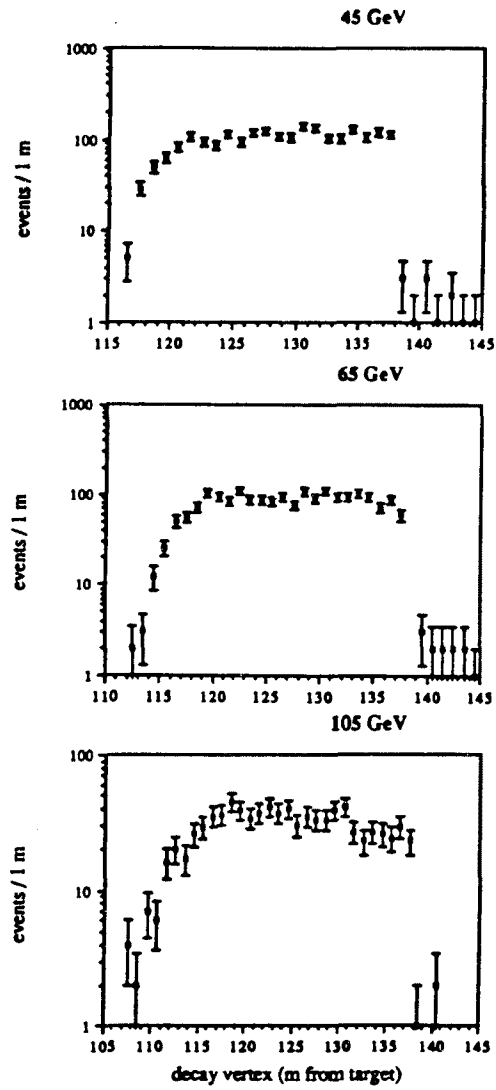


Figure 31, cont. Decay vertex distributions from the vacuum beam at three representative energies.

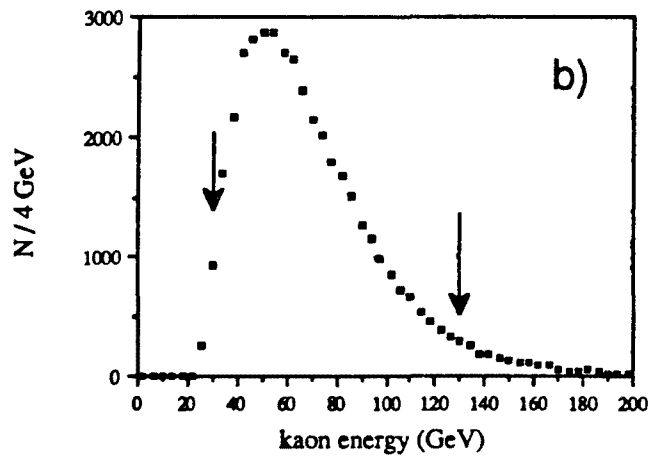
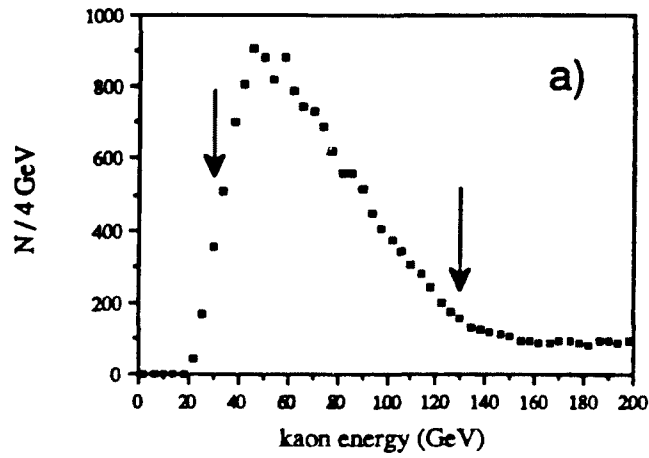


Figure 32. Reconstructed kaon energy distribution for a) vacuum beam, b) regenerated beam. These events passed all cuts except the $124 \text{ m} < z < 137 \text{ m}$ cut.

5.4 Glass calibration

In the neutral mode analysis, we used the lead glass information to give us both the kaon energy and the decay vertex z position, so the glass calibration was very important. We defined the gain of a glass block-photomultiplier tube-base-ADC channel as the ratio of the number of ADC counts above pedestal to the energy deposited in the block for 2 GeV photons. The momentum of a calibration electron could be determined from the amount it was deflected by the analyzing magnet, as well as from the energy of the electromagnetic shower in the lead glass. We could not, however, assume that the number of ADC counts seen in the glass was proportional to the measured track momenta, since the amount of Čerenkov light from a shower seen at the phototube depends in general on the amount of attenuation in a glass block and therefore on the depth of the shower in the glass. This shower depth depends on energy; more energetic showers peak at a point deeper into the glass than less energetic ones. The shape of this nonlinearity had to be determined before the gains could be calculated. This was done by separating the calibration data into 1 GeV energy bands between 2 and 8 GeV and 2 GeV bands between 10 and 20 GeV. The average gain correction between adjacent bands was determined (defining the 2 GeV bin to be 1), and these factors ($=E_{true}/E_{measured}$) were used to determine the coefficients of the power law:

$$E_{true} = aE_{measured}^{\beta}$$

The nonlinearity found in this way was $\beta = .9761 \pm .0015$. The fit agrees well with the predictions of Longo and Sestili¹⁵. Once the nonlinearity was established, the gains were determined by requiring that the average (true glass energy/track momentum) for calibration events be unity.

In addition to the special calibration events, we also used “sheet π^0 ” events for

determining the glass energy scale. Our neutral mode data contained about 250,000 events in which π^0 's were produced from hadron interactions in the lead converter along with two charged particles which triggered the apparatus. The specific z position and limited activity of these events in the glass made them especially valuable, since we could use the relation

$$m_\pi^2 = \frac{E_1 E_2 r_{12}^2}{z^2} \quad (1)$$

for the pion decay, where z was the (known) distance between the lead glass and the lead converter, and the energy of the lower energy photon was assumed to be given correctly by the e^+e^- calibration. Fourteen thousand additional events in which an η^0 was produced instead of a π^0 provided a cross-check on the energy scale. In this way we extended the determination of the nonlinearity to energies too high to be produced by sweeping electron pairs. We also found that there was about a 1.8% difference in energy scale between showers from incident electrons and showers from incident photons since photon showers started farther into the glass, suffering less attenuation. (See Figure 33.)

5.5 Finding clusters

Once the energy scale was determined we could analyze the neutral events. We needed a way to identify the energy depositions in the glass that we called clusters. In general we defined a cluster as a 3×3 group of blocks; this group contained about 98% of the energy of an electromagnetic shower, of which 60% to 85% was contained in the central block. Because the uncertainty in energy in blocks outside of the nine was large due to photon statistics, we chose not to include the next "ring" of 16 blocks. The basic cluster finding algorithm will be given next; any modifications to it in the course of the neutral reconstruction analysis will be pointed out as they occur in the discussion.

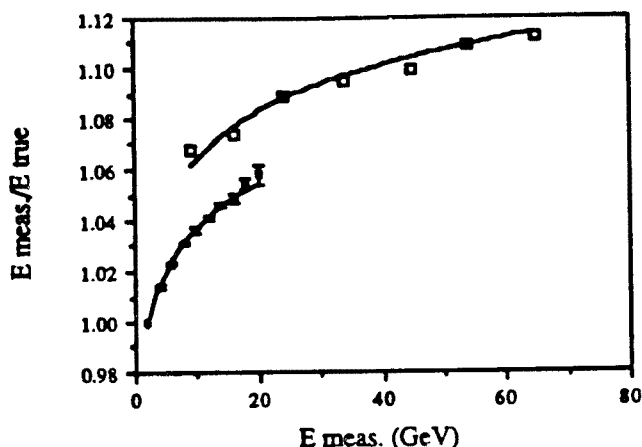


Figure 33. Measured energy/true energy as a function of measured energy. The lines represent an exponential with the same slope as that used for the nonlinearity. Open squares represent energies from photon clusters; closed squares represent energies from electron clusters.

The cluster finder looked at each block of the array individually. Blocks which contained more than 200 MeV were considered as candidates for cluster centers. If the block contained more energy than its eight adjacent neighbors and the sum of the nine together held more than 500 MeV, the block was identified as a cluster center. With this algorithm, we could not separate clusters closer than two blocks (about 12 cm) apart. Events in which more than 20 clusters were identified were rejected. A better estimate of the cluster center was then obtained by comparing the ratios of the energies of the three blocks in the central row or column of the cluster to the energy in the rows or columns on either side. A formula based on shower shapes converted these ratios into the distances by which to shift the cluster center from the block center. This treatment gave us position resolution which varied as a function of how far from the center of the block the photon hit, from 5.6 mm for photons hitting the center of the block to 2 mm for photons hitting within a few mm of the edge of the block. This variation in

resolution was determined from studies of cluster position with respect to track position from undeflected glass calibration events.

5.6 Neutral mode: $K \rightarrow \pi^0 \pi^0$

The neutral analysis, like the charged analysis, was done in three steps. As in the charged mode, the first pass was used to reject obviously bad events, *e.g.*, events with the wrong track topology. We cut all events in which the absorber and regenerator were in different beams. The average ADC pedestals were calculated from the between-spill pedestal events, while the nominal gains were adjusted by small corrections based on the flasher information. Cluster finding was then carried out as just described; events with fewer than two clusters were rejected. Cluster energies were corrected for nonlinearity as described in the calibration section above using $a=1.0119$.

Before tracks were actually found, we made a 1 ns correction to all drift times to take into account a difference in timing between the charged and neutral triggers. The procedure for finding the x track segments and matching upstream and downstream tracks was the same as before; now, however, we discarded events in which there were more than four pairings of upstream and downstream x track segments which fulfilled the meeting-in-the-magnet requirement. If there were three or four such pairs, the downstream segments were extrapolated to the glass, and the pair with the smallest separation was chosen.

The track finding procedure for y tracks was also nearly unchanged, although tracks with adjacent hits in chambers 1 and 2 were not discarded if the two tracks were close

together at the glass, as measured by XSEP2, where

$$\text{XSEP2} = \frac{(x_+ - x_-)^2}{\frac{1}{p_+^2} + \frac{1}{p_-^2}}.$$

The $x_{-,+}$ are the positions of the electron and positron at the glass, and $p_{-,+}$ are the corresponding momenta. Because of the reconverging technique, the pair should have been separated at the glass only by multiple scattering. The angle through which each particle scattered should therefore have been proportional to $1/p$; XSEP2, then, is independent of momentum. We expected the numerator always to be small for the electron pair; for hadrons, on the other hand, we did not necessarily expect a small separation at the glass.

If there were between one and eight y track candidates, we kept the event for further study. Choosing the correct y view tracks was accomplished by matching the y track positions at the glass with cluster centers which had already been matched with x tracks. The x and y impact positions had to fall within 5 cm of a cluster to match. Y tracks down the holes were kept and assigned a track-cluster separation of 5 cm. If the pair had not converged to a single cluster, the closest y track was assigned to each cluster. If more than two track candidates remained after the matching, the pair of y tracks which were closest to each other at the glass were retained.

With the best track candidates selected in this way, we attempted the matching of the x -view tracks with the y -view. We calculated the distance between the track impact point and the nearest cluster for each of the two possible x - y pairings. A match was made if the distance was less than 7 cm. The pairing with the most matches was assumed to be the correct one, while the x - y pairing with the smallest sum of separations was chosen if both pairs had the same number of cluster matches. At this point we examined the remaining clusters, demanding that they each have 2 GeV of energy and that the

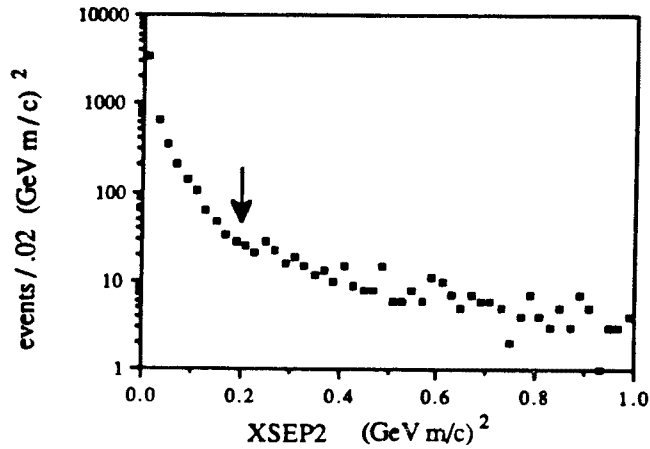


Figure 34. Weighted z track separation at the glass for electron and positron tracks. These events had the proper absorber and regenerator positions, more than one electron in the glass, two z tracks, one or two y tracks, and no tracks down the beam pipe.

adder corresponding to the central block of the cluster saw 80% of the cluster energy. The purpose of the adder cut was to eliminate clusters due to accidental hits. Recall that the adder ADC gate was narrower than the gate for the lead glass. Accidental events which were later than the adder gate were not seen by the adder even though they were seen in the glass. Tracks from good events were corrected for rotations and so on as above and refitted.

Events in which any tracks pointed down the beam pipes were now discarded. To include the energy of such a track, we would have had to assume that the particle was an electron or positron, which would have been hard to establish without using an E/p requirement. In addition, the particle might have crashed into the pipe, depositing some energy in the pipe and some in the glass, where the actual amount would be difficult to determine. Events with weighted track separation $XSEP2 > 0.2$ were also rejected as probable hadron events (Figure 34).

For the two pion sample we kept only events which had 2 x tracks and 1 or 2 y tracks. (For events which satisfied the above cuts, we found that about 40% had only one y track. Legitimate single- y -track events in the neutral mode were present because the e^+e^- tracks were separated only by multiple scattering in the y view. The tracks were often too close together to be resolved by the chambers.) The tracks had to match clusters and we required three additional clusters which had no associated tracks. This allowed us to take into account events in which the e^+e^- pair did not fully reconverge at the lead glass.

Finally we made use of the BA's lepton/hadron separation capability. Each of the three sections which made up the BA were themselves made of three layers of lucite fingers. The energy in the first and fourth of these layers were summed together. If they contained more than 5 GeV of energy, the sum was compared to the energy in the seventh layer. If the back part of the BA had more energy than the front ($E_7/(E_1 + E_4) \leq 0.2$), the event was retained, since such events were probably hadron interactions. The total of 48 layers each of lead and lucite presented 28 radiation lengths and 1.3 interaction lengths of material to the beams. Thus after the first section, only 36% of hadrons had interacted, while virtually all of the electrons had interacted. Events in which there was less than 5 GeV of energy in the first and fourth layers were also kept (Figure 35). Events which were acceptable to this point were saved in condensed form for further analysis.

There was a slight difference in the cluster finder for the second pass: it did not include blocks in a second cluster which had already been assigned to one cluster. The second stage of the analysis applied only a few cuts. Events which had activity in the RA were discarded (Figure 36). A CA cut rejected events near the hole region. Since the CA was more than a meter in front of the glass, some particles were able

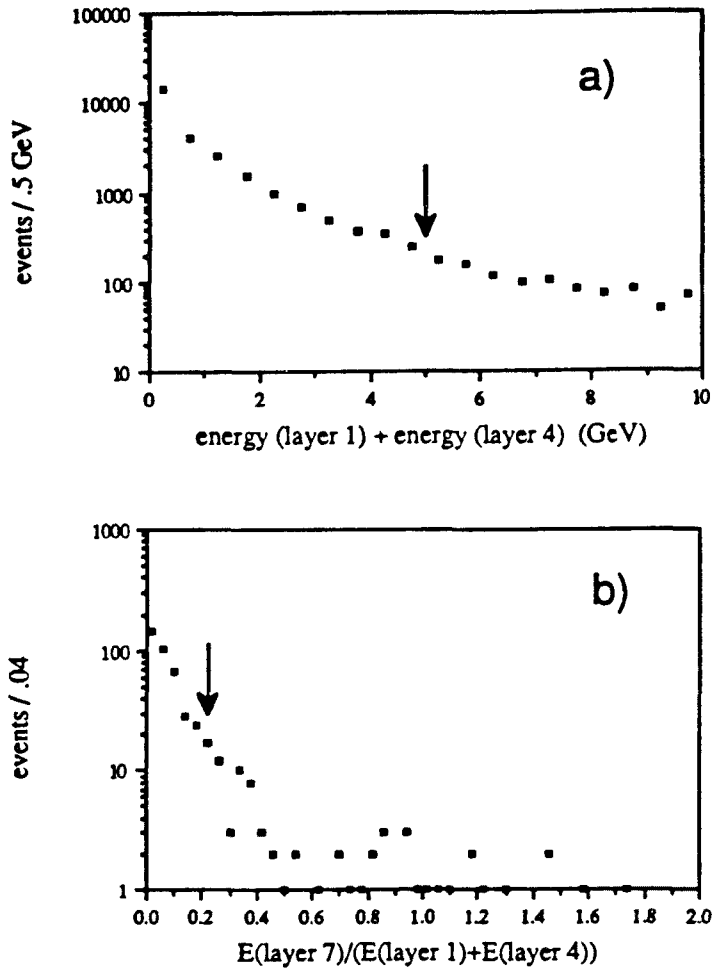


Figure 35. a) Energy deposited in the back anti. b) Distribution of energy in the back anti for events with $E(\text{layer1}) + E(\text{layer4}) \geq 5$ GeV. These events have the same cuts as those in Figure 34 with some additional restrictions: at least one track had to match a cluster, there had to be exactly three clusters, and XSEP2 had to be less than 0.2.

to miss the CA while still landing near enough to the pipes to suffer energy leakage. Events in which any CA counter had a signal of more than 50 counts above pedestal were rejected (Figure 37). An improvement in the signal-to-background ratio was also seen by eliminating events in which the lead-lucite sections of VA3 saw more than 1.5 times a minimum-ionizing signal (Figure 38) or in which DRAN saw more than 0.5 of a minimum-ionizing signal (Figure 39), indicating possible stray photons from $3\pi^0$ decays. Minor hardware problems made the rest of the lead-lucite counters less reliable at rejecting background than we needed, so we chose not to use them in this analysis. Events with stray charged particles were rejected by requiring no activity in the VA2, VA3, and VA4 scintillators (Figure 40).

Tracking was then redone as above, as was the x - y matching. At this point we demanded that there be either one or two clusters which were matched by tracks. The corrections for rotations and transit times, as well as the momentum determinations, were performed. In addition, both tracks had to match clusters.

Some small corrections to the cluster energies were made to take into account other physical effects. The energy of clusters which had a corner block missing was increased by a factor of 1.006 while the energy for those with a side block missing was increased by a factor of 1.017 to make up for the missing energy. Studies showed that the size of the energy correction needed was comparable to uncertainties in the energy in the blocks due to shower fluctuations, so we chose not to correct more precisely for a position dependence.

In the case where both tracks converged at the same cluster, the energy of a 5×5 group of blocks rather than just a 3×3 group was assigned to the cluster, omitting blocks in the outer ring of 16 which had more energy than the corresponding blocks in the first ring. Such outer blocks were probably centers for separate clusters. The

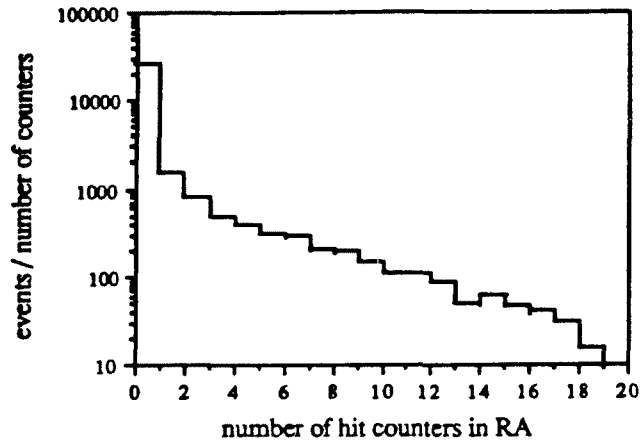


Figure 36. Number of hits in the RA per neutral event. These events passed all first stage analysis cuts.

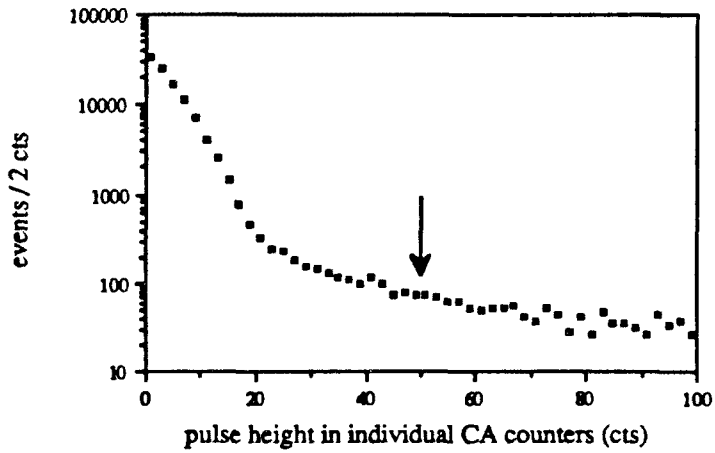


Figure 37. Signal in collar anti, pedestal subtracted. These events passed all first stage cuts and had no activity in the RA.

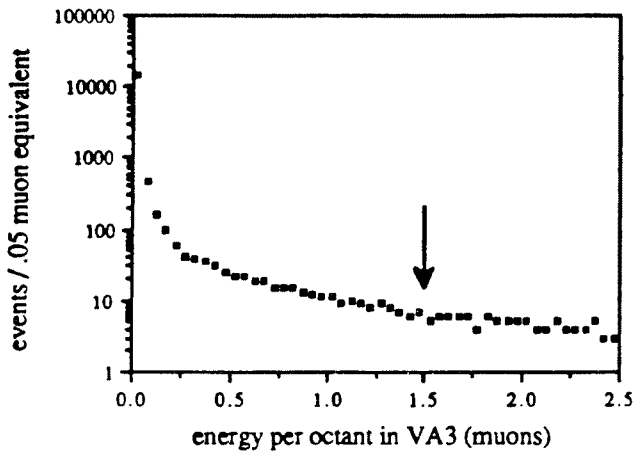


Figure 38. Signal in VA3, expressed in number of minimum-ionizing particles. These events passed all first stage cuts as well as second stage RA and CA cuts.

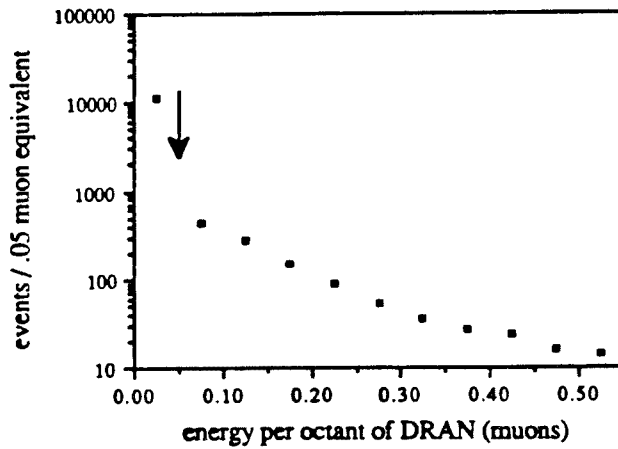


Figure 39. Signal in DRAN, expressed in number of minimum-ionizing particles. These events passed all first stage cuts as well as second stage RA, CA, and VA3 cuts.

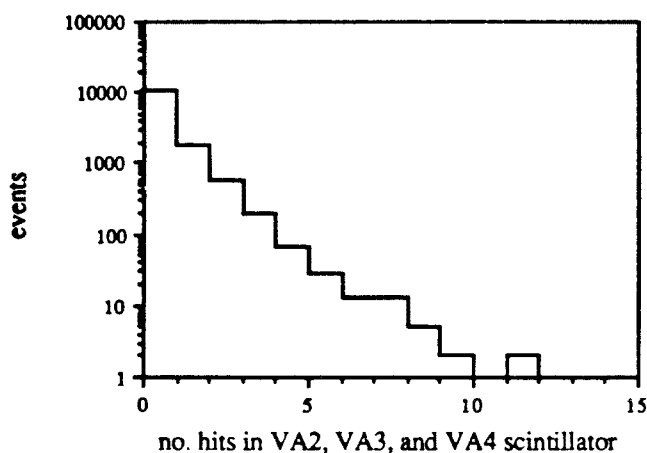


Figure 40. Number of VA2, VA3, and VA4 scintillators hit per event. These events passed all first stage cuts as well as second stage cuts on RA, CA, VA3 lead-lucite, and DRAN.

electron pair clusters were generally larger than single photon clusters since the e^+ and e^- did not always land exactly on top of each other. About 70% of the tracks were separated by 4.5 cm or less, although this spread did depend on energy: for a combined e^+e^- energy of 5 GeV, a similar fraction was separated by 7.5 cm or less, while for 45 GeV this separation went to about 2 cm. (See Figure 41.)

Data which passed the set of cuts just described were saved on separate summary tapes. The final analysis of the data was mainly concerned with further corrections to the lead glass energy. We first corrected for the difference in light collected from showers initiated by photons and those initiated by electrons. These corrections were different depending on whether or not the tracks converged well enough to make only one cluster. If the e^+ and e^- each had energy E , a cluster formed from both together would have an energy $2E$. Shower maximum for each shower, though, would be at a depth appropriate for a shower of E , farther from the phototube than shower maximum

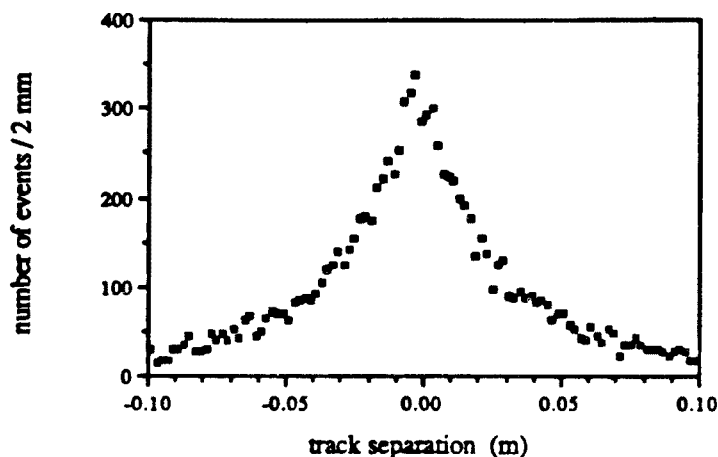


Figure 41. Electron-positron z view track separation at the lead glass. These events satisfied all first and second stage cuts.

for a shower of $2E$, and so would be attenuated more. In addition, light from showers started by a photon started an average of 0.7 radiation lengths farther into the glass than those started by electrons.

For the case of both tracks converging to a single cluster, the energy of the cluster was first reduced by a factor of 1.0265 to correct for having used a 25-block sum rather than a nine-block sum in determining the energy. The cluster energy was then split between the tracks according to the ratio of their momenta. Each energy was then separately corrected for nonlinearity using $a = 1.0188$, and the corrected energies were summed to give the cluster energy. For the case of tracks giving two clusters in the glass, the energies of the two clusters were reduced by a factor of 1.0065 to correct for overlap of energy between the two clusters, then each of them was corrected for nonlinearity as above. (Note that, with the modification to the cluster finder described above, this adjustment is no longer strictly correct. Removing it entirely changes the phase difference by only a small amount, so it was retained.) Once the electron clusters

were properly treated, the photon clusters were also corrected for nonlinearity using an a of 1.0017. The difference in the normalization factor a between photons and electrons was just due to the difference in shower depth mentioned above. The values for a were determined from calibration electron and π^0 events to a few tenths of a percent. Earlier on, we had required a minimum energy of 2 GeV for photon clusters only; we now imposed a minimum energy cut of 1 GeV on any clusters associated with the electron and positron.

We were now ready to reconstruct kaons, but for this it was more convenient to deal with four photons than three photons and the electron pair, so we constructed a “pseudophoton” from the e^+e^- pair in events where they gave two separate clusters. The pseudophoton energy was determined by summing the energies of the clusters, while the average coordinates were given by

$$q = \frac{E_i q_i + E_j q_j}{E_i + E_j},$$

where $q = x$ or y and i, j refer to the cluster. Finally all of the cluster energies, electron and photon, were reduced by an overall scale factor of 0.996. This factor was necessary to give us the proper value for the reconstructed edge of the regenerator as a function of energy; it was a measure of how well we understood the calibration process and electron/photon differences in the glass response.

The z coordinates of the pion vertices were determined by calculating z from equation (1) for each pair of photons of the three possible distinct pairings. A trial common vertex for the kaon was then calculated from a weighted average of the two pion vertices:

$$z_{avg} = \frac{\frac{z_{\pi i}}{\sigma_{\pi i}^2} + \frac{z_{\pi j}}{\sigma_{\pi j}^2}}{\frac{1}{\sigma_{\pi i}^2} + \frac{1}{\sigma_{\pi j}^2}},$$

where $\sigma_{\pi i} =$

$$\sigma_{\alpha\beta} = z_{\alpha\beta} \sqrt{\left(\frac{\sigma_{E\alpha}}{E_\alpha}\right)^2 + \left(\frac{\sigma_{E\beta}}{E_\beta}\right)^2 + \frac{4}{r_{\alpha\beta}^2} \sum_{q=z,y} (q_\alpha - q_\beta)^2 (\sigma_{q\alpha}^2 + \sigma_{q\beta}^2)} .$$

Here $\sigma_{E\alpha}$ was the energy uncertainty for the α^{th} cluster, determined from the measured energy resolution ($2\% + 6\%/\sqrt{E}$). The $\sigma_{z\alpha}$ were cluster position uncertainties, which for photon clusters depended on where the photon struck the block, as discussed above. For clusters which matched tracks, the position uncertainty in the x direction was given by

$$\sigma_x = \frac{0.14}{\sqrt{p_1^2 + p_2^2}} .$$

The y resolution was the same if two y tracks were found, but the denominator was replaced by the greater momentum of the two if only one y track was found, expressing the slightly greater uncertainty in direction associated with effectively having to average the tracks together. (See Figure 42.)

The consistency of the two pion vertices was determined by calculating

$$\chi^2 = \sum_{\substack{\text{pions} \\ i=1,2}} \frac{(z_i - z_{avg})^2}{\sigma_{\pi i}^2} ,$$

where z_i was the vertex calculated from the i^{th} pion, z_{avg} was the trial common vertex, and $\sigma_{\pi i}^2$ was the same as above. The analysis required a pairing χ^2 of less than 1 for an event to be accepted (Figure 43). A large value of χ^2 indicated that the four clusters did not all come from a clean $2\pi^0$ decay. Such events could have been $3\pi^0$ decays with missing or fused photons, for example. We then took the z_{avg} from the pairing with minimum χ^2 as the kaon decay vertex. Only events in which the vertex was between 124 m and 137 m from the target were used in this analysis (Figure 44), again, because the resolution smearing was difficult to treat properly.

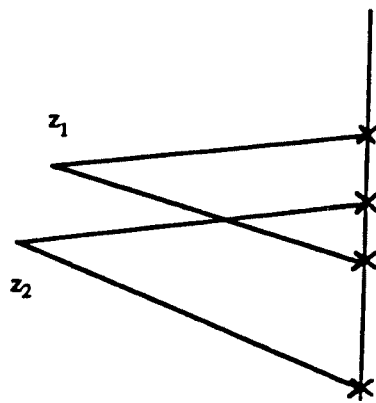
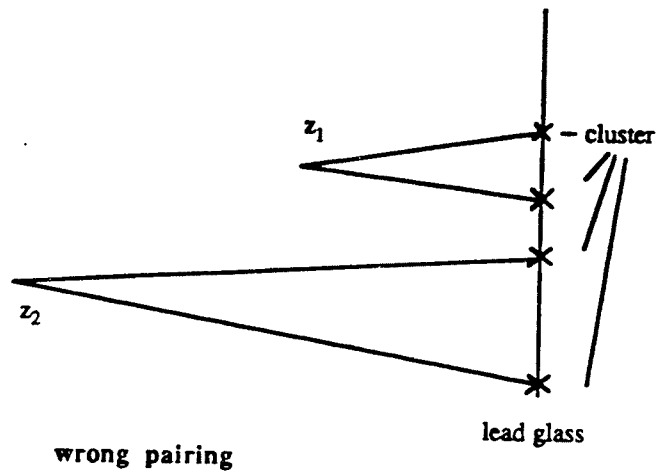


Figure 42. Two of three possible pairings for four photons; the correct pairing gives the closest agreement between the two pion vertices.

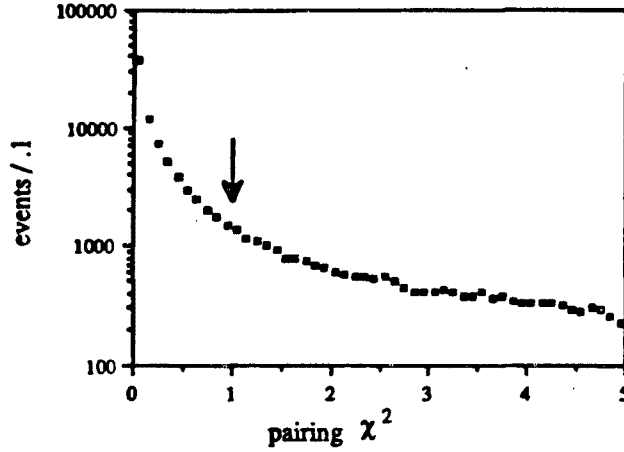


Figure 43. χ^2 for the best pairing of photons. These events satisfied all first and second stage cuts as well as final stage beam pipe aperture and e^+e^- cluster minimum energy cuts.

We now tightened our cluster energy cuts somewhat. Because it was difficult to get calibration events of such a high energy, even with the sheet π^0 's, the pseudophoton cluster and the photon clusters were each required to have less than 80 GeV of energy. Now that the final cluster energies were established, we increased the minimum energy of photon clusters to 2.5 GeV (Figure 45), leaving us less sensitive to the cluster energy adjustment at low energy.

The upstream and downstream y view track slopes and intercepts were averaged together and were used along with the x track parameters to find the impact points of the tracks at the glass. We then cut on

$$SEP2 = \frac{(x_+ - x_-)^2 + (y_+ - y_-)^2}{\frac{1}{p_+^2} + \frac{1}{p_-^2}},$$

a two-dimensional version of the momentum-independent separation XSEP2, requiring $SEP2 < 0.2$ for good events (Figure 46), again as a way of rejecting hadrons.

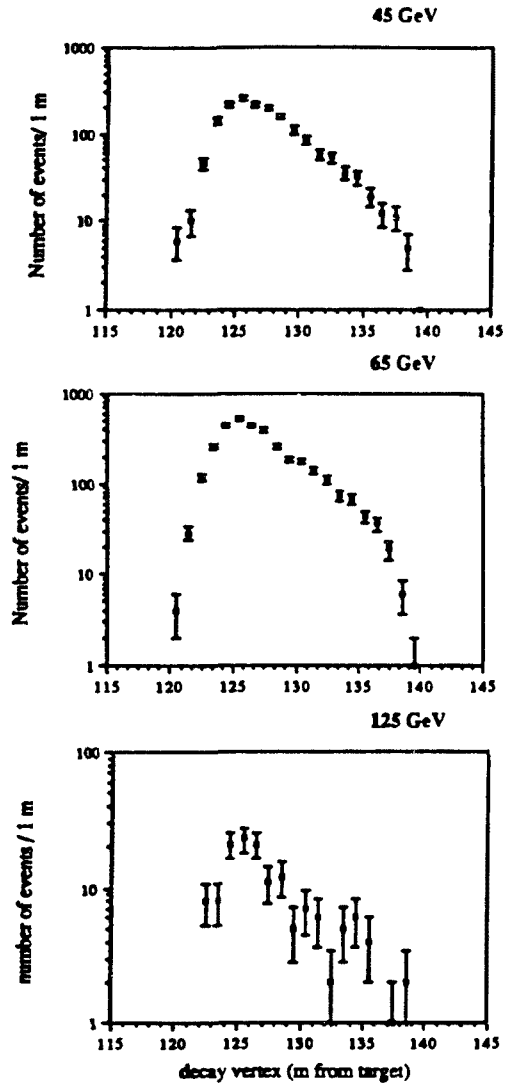


Figure 44. Decay vertex distributions from the regenerated beam at three representative energies. These events satisfied all first, second, and third stage cuts.

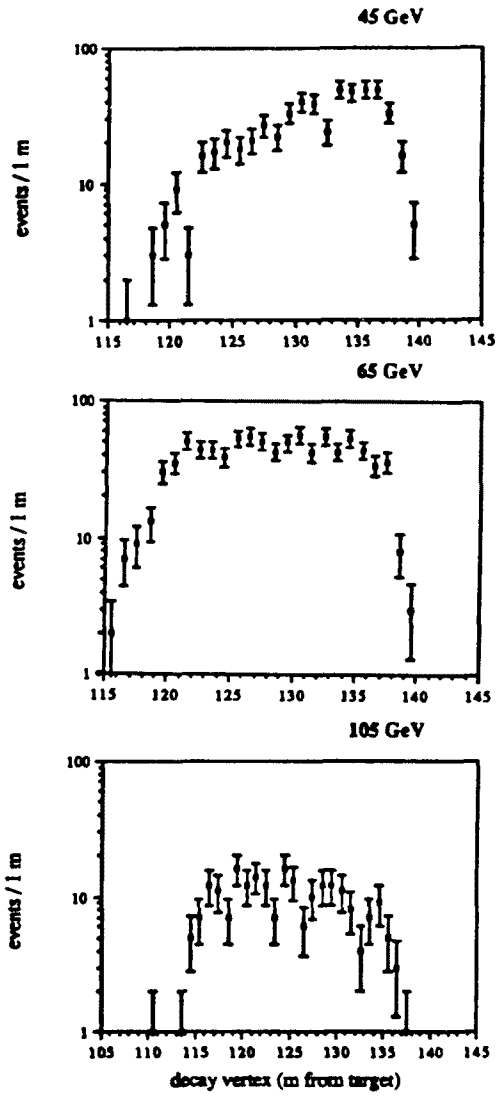


Figure 44, cont. Decay vertex distributions from the vacuum beam at three representative energies.

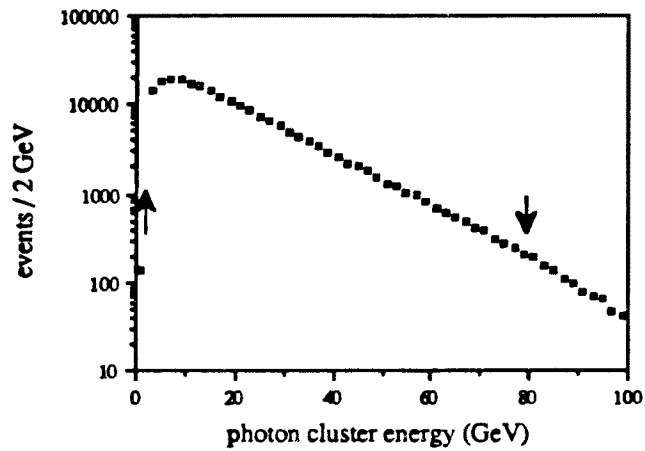


Figure 45. Reconstructed energy of photon clusters. These events satisfied all first and second stage cuts as well as final stage cuts on beam pipe aperture, e^+e^- cluster energies, and pairing χ^2 .

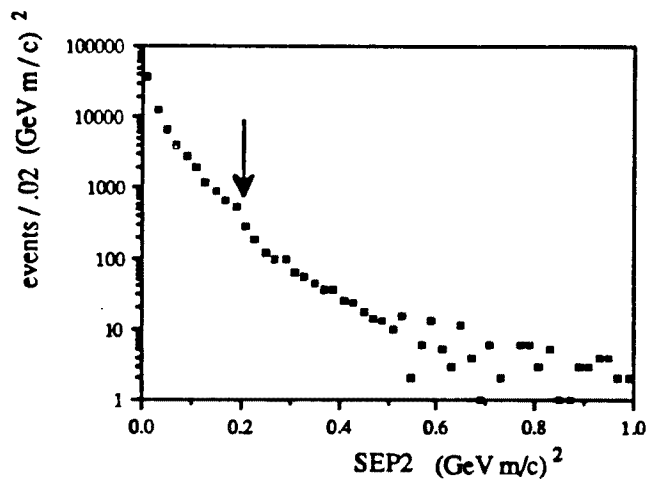


Figure 46. Weighted separation of the electron and positron tracks at the lead glass. These events satisfied the same cuts as events in Figure 45, plus photon cluster energy cuts.

We now made a p_t^2 cut using the directional information from the e^+e^- tracks as follows (Figure 47): Once the z of the vertex had been determined, the tracks from the pair upstream of the analyzing magnet were pointed back to the converter sheet to give the transverse coordinates of the parent photon there. The photon direction was then extrapolated to the decay plane to give the transverse decay position. We had additional directional information about the kaon from the center of energy of the event in the glass. The three photons were not deflected by the magnetic field, and, because the electron and positron were of opposite charge, the pseudophoton constructed from them suffered no net deflection. This meant that the center of energy in the glass corresponded to the impact point of the kaon had it not decayed. The line between the center of energy and the decay vertex was then extended upstream to the regenerator. The angle θ between this line and the direction of the incident K_L (determined as in the charged analysis), along with the K energy, determined $p_t^2 = p_K^2 \sin^2 \theta$. Here our resolution allowed us to cut events with $p_t^2 > 4000$ (MeV/c)². (See Figures 48 and 49.) As before, this eliminated more of the diffractive background than data events.

Another background cut was on E/p , the ratio of the lepton shower energy in the glass to its track momentum. Hadron showers had small E/p since they didn't deposit most of their energy in the glass. We also cut events which had too large a ratio. These were events in which there was sizeable *bremsstrahlung* photon energy, for example, or an extra photon cluster fused with the e^+e^- cluster. The limits for acceptable E/p were 0.8 and 1.5 (Figure 50).

Four aperture cuts were made on the paths of the e^+e^- pair. The first required the e^+ and e^- to pass through the vacuum window within 58.5 cm of the center. This aperture cut was the same size as that for the charged mode. (See Figure 51.) The second and third required the tracks to pass through the A bank and the B bank to

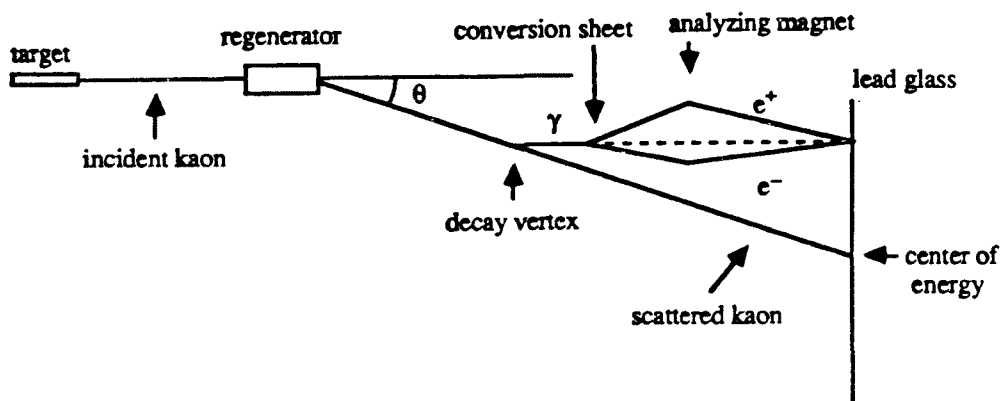


Figure 47. Schematic of p_i^2 reconstruction for neutral decays.

make sure that these were the tracks which had triggered the event. The A bank cut was the same as in the charged mode analysis (Figure 52), while the B bank cut was the same size as the bank itself: 1.8 m by 1.8 m (Figure 53). The final aperture cut rejected events in which any cluster center fell in one of the glass blocks surrounding the beam pipes, since their nonlinearities were not as well determined as those of the rest of the array; this gave a noticeable effect in the phase determination.

The K energy was calculated by summing up the energy of all clusters. For this analysis, only events with kaon energies between 40 and 130 GeV were used. There were too few events at higher energies than this to give sufficient statistics for an (E, z) bin phase analysis. In addition, for higher energies we also saw the effects of K_S - K_L interference in the vacuum beam. This was not unexpected since K^0 and \bar{K}^0 are produced at the target, giving a mixture of K_S and K_L . The interference term is proportional to $\exp(-\Gamma_S \tau/2)$, allowing K_S effects to be seen further downstream than if the beam were pure K_S . Kaons with energies lower than 40 GeV were discarded

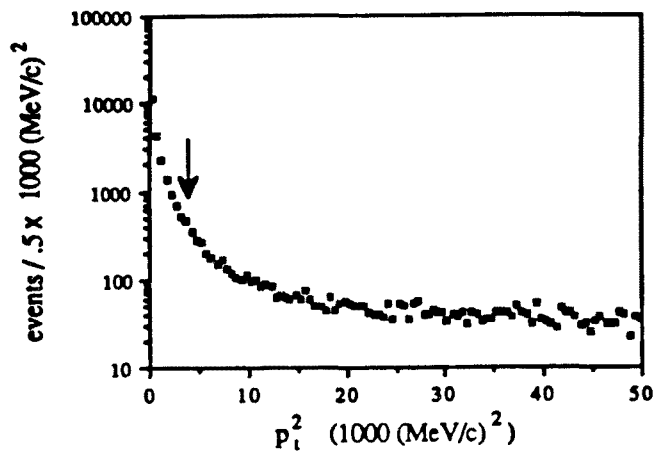


Figure 48. p_t^2 for events from the regenerated beam. These events and those in Figure 49 satisfied all first, second, and third stage cuts.

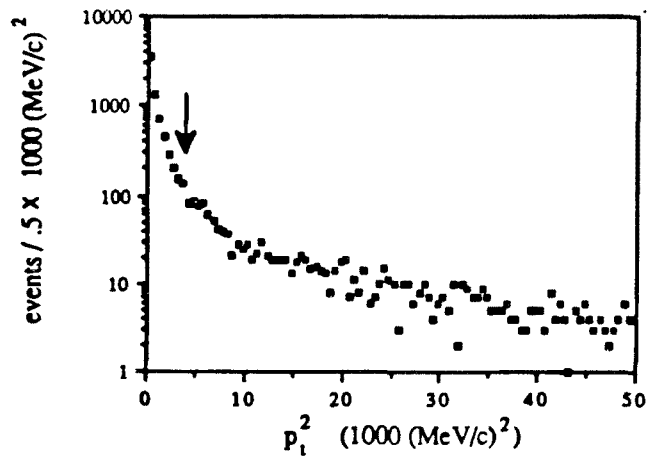


Figure 49. p_t^2 for events from the vacuum beam.

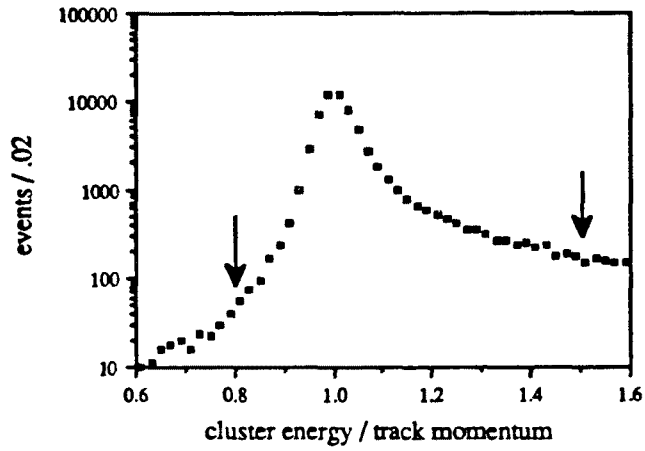


Figure 50. Electron cluster energy/track momentum. These events satisfied the same cuts as events in Figure 46, as well as the SEP2 cut.

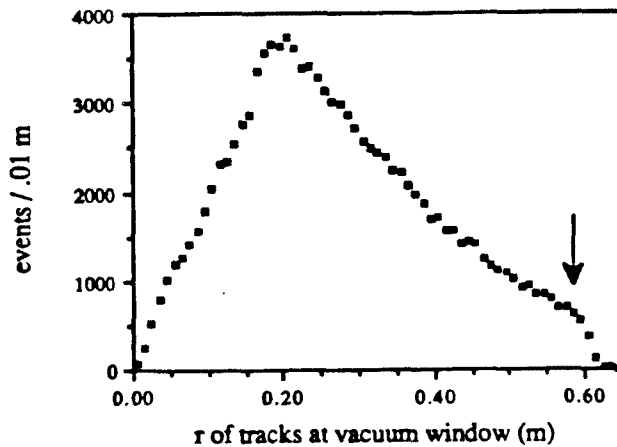


Figure 51. Distance of electron and positron tracks from the center of the vacuum window. These events satisfied the same cuts as those in Figure 50, as well as an E/p cut and a requirement that $110 \text{ m} < z < 140 \text{ m}$.

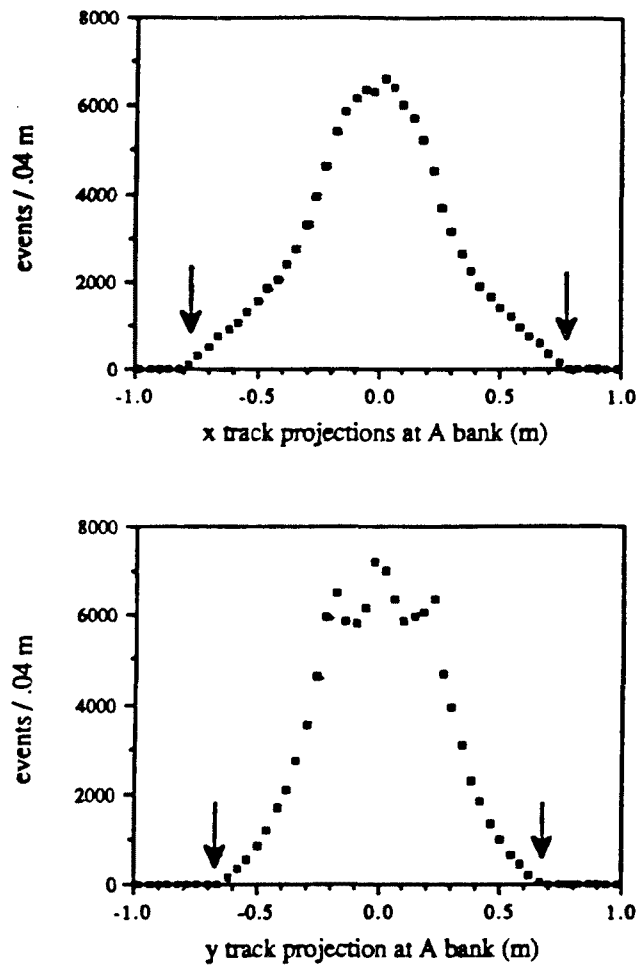


Figure 52. Positions of e^+e^- tracks at the A bank. These events satisfied the same cuts as those in Figure 51 as well as a vacuum window aperture cut.

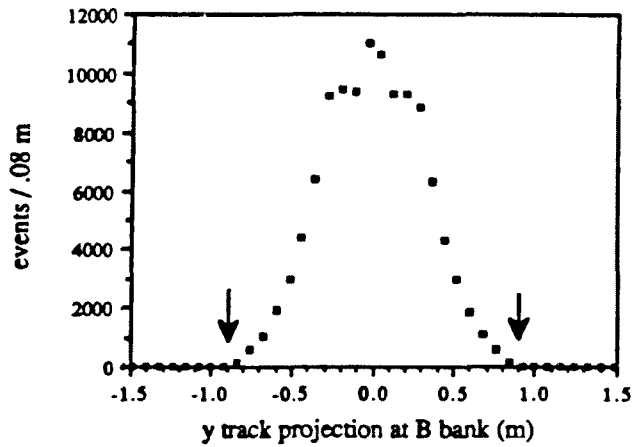
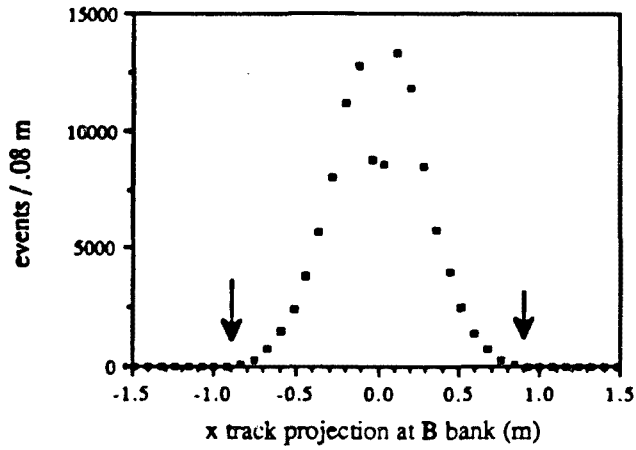


Figure 53. Positions of e^+e^- tracks at the B bank. These events satisfied the same cuts as those in Figure 52 as well as A bank aperture cuts.

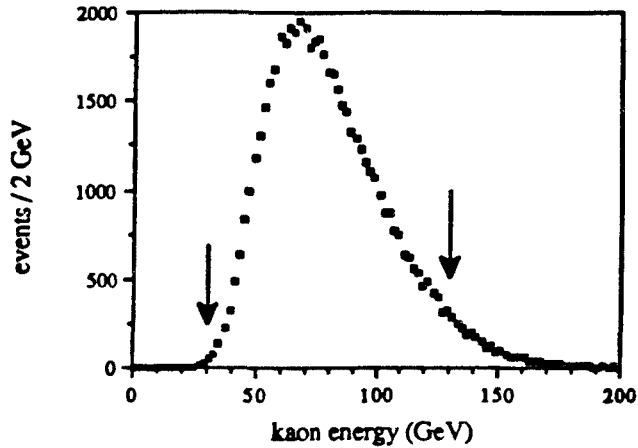


Figure 54. Reconstructed kaon energy distribution. These events satisfied the same cuts as those in Figure 53 as well as B bank aperture cuts.

to avoid having to understand the effects of the 30 GeV E_T threshold in the trigger (Figure 54).

Knowing the vertex and the total energy allowed us to compute the contributions of each photon to the three momentum components. These determined the total kaon momentum which in turn gave the kaon invariant mass. The resolution was good enough to allow a cut of $\pm 20 \text{ MeV}/c^2$ around the world average K mass value of $497.7 \text{ MeV}/c^2$, eliminating misreconstructed kaons and background events.

These cuts left us with 14536 $2\pi^0$ decays in the regenerated beam and 4386 decays in the vacuum beam (Figures 55 and 56). Table 3 shows the raw data sample (E, z) populations for charged mode; table 4 shows the bin populations for neutral mode.

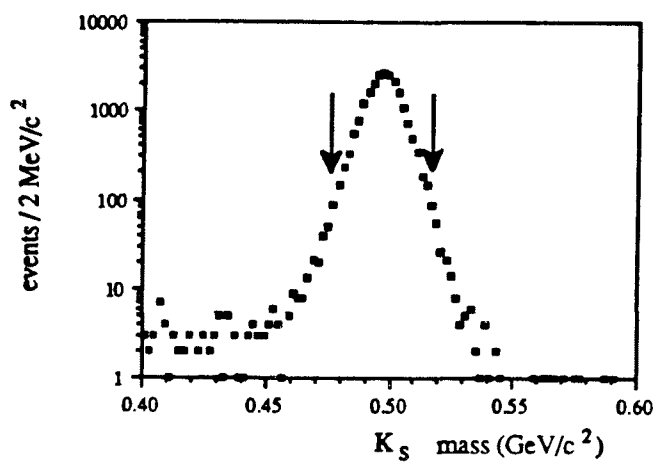


Figure 55. Reconstructed kaon mass, regenerated beam. These events satisfied all cuts except kaon mass.

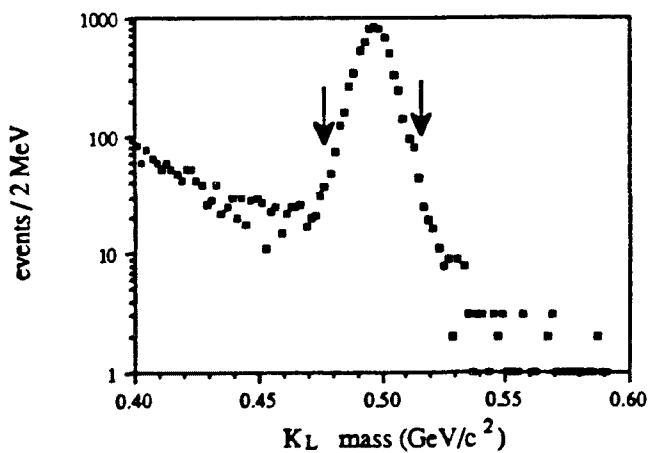


Figure 56. Reconstructed kaon mass, vacuum beam. These events satisfied all cuts except kaon mass.

Table 3. Charged mode data before background subtraction.

Charged data, regenerated beam, set 1

E =	35	45	55	65	75	85	95	105	115	125 GeV
z = 115.5 m	0.	0.	0.	0.	0.	0.	0.	0.	0.	0.
	0.	0.	0.	0.	0.	0.	0.	0.	0.	0.
	0.	0.	0.	0.	0.	0.	0.	0.	0.	0.
	0.	0.	0.	0.	0.	0.	0.	0.	0.	0.
120.5	0.	0.	0.	0.	0.	0.	0.	0.	0.	0.
	0.	0.	0.	0.	0.	0.	0.	0.	0.	0.
	1.	0.	0.	0.	0.	1.	0.	2.	0.	0.
	517.	665.	577.	418.	325.	236.	161.	88.	64.	41.
125.5	931.	1331.	1128.	873.	602.	450.	300.	202.	142.	97.
	577.	872.	832.	712.	542.	375.	255.	169.	114.	77.
	389.	623.	583.	500.	449.	312.	238.	139.	111.	73.
	284.	453.	478.	420.	311.	232.	205.	131.	77.	55.
	167.	270.	326.	347.	258.	223.	141.	107.	67.	46.
130.5	120.	187.	291.	273.	224.	191.	142.	75.	48.	45.
	74.	171.	214.	202.	180.	120.	100.	74.	47.	40.
	52.	110.	128.	131.	139.	133.	78.	71.	49.	37.
	28.	78.	102.	132.	118.	83.	84.	47.	43.	31.
	15.	60.	73.	81.	79.	75.	68.	29.	23.	24.
135.5	4.	46.	68.	67.	59.	60.	58.	49.	29.	22.
	4.	35.	49.	56.	60.	49.	45.	27.	27.	23.
	4.	22.	43.	68.	78.	59.	48.	19.	35.	16.
	3.	7.	16.	40.	34.	39.	39.	26.	21.	20.
	0.	0.	1.	0.	0.	1.	1.	0.	0.	0.
140.5	0.	0.	1.	1.	0.	0.	0.	0.	0.	0.
	0.	0.	0.	0.	0.	0.	0.	0.	1.	0.

Charged data, regenerated beam, set 2

E =	35	45	55	65	75	85	95	105	115	125 GeV
z = 115.5 m	0.	0.	2.	0.	0.	0.	0.	0.	0.	0.
	0.	0.	0.	0.	0.	0.	0.	0.	0.	0.
	0.	0.	0.	0.	0.	0.	0.	0.	0.	0.
	0.	0.	0.	0.	0.	0.	0.	0.	0.	0.
120.5	0.	0.	0.	0.	0.	0.	0.	0.	1.	0.
	0.	0.	1.	3.	1.	1.	1.	0.	0.	0.
	635.	889.	745.	560.	419.	298.	174.	126.	67.	55.
	1217.	1604.	1422.	1117.	821.	576.	358.	300.	180.	129.
125.5	789.	1103.	1085.	861.	669.	473.	359.	231.	166.	104.
	516.	764.	757.	660.	546.	419.	285.	193.	112.	103.
	336.	548.	589.	531.	408.	306.	229.	189.	109.	67.
	234.	399.	450.	416.	370.	248.	207.	149.	93.	68.
	158.	263.	296.	330.	251.	214.	179.	120.	77.	41.
130.5	101.	192.	260.	245.	217.	188.	139.	97.	58.	48.
	61.	180.	177.	189.	163.	142.	126.	91.	55.	41.
	43.	84.	117.	159.	143.	135.	89.	78.	44.	37.
	20.	67.	110.	117.	108.	96.	81.	53.	43.	27.
	18.	39.	71.	92.	96.	81.	65.	48.	33.	23.
135.5	12.	35.	69.	77.	85.	70.	53.	26.	37.	16.
	4.	22.	43.	68.	78.	59.	48.	19.	35.	16.
	3.	7.	16.	40.	34.	39.	39.	26.	21.	20.
	0.	0.	1.	0.	0.	1.	1.	0.	0.	0.
	0.	0.	1.	1.	0.	0.	0.	0.	0.	0.
140.5	0.	0.	0.	0.	0.	0.	0.	0.	1.	0.
	0.	0.	0.	0.	1.	1.	0.	0.	0.	1.

Table 3, cont. Charged mode data before background subtraction.

Charged data, regenerated beam, set 3

E =	35	45	55	65	75	85	95	105	115	125	GeV
z = 115.5 m	0.	0.	0.	0.	0.	0.	0.	0.	0.	0.	0.
	0.	0.	0.	0.	0.	0.	0.	0.	0.	0.	0.
	0.	0.	0.	0.	0.	0.	0.	0.	0.	0.	0.
	0.	0.	0.	0.	0.	0.	0.	0.	0.	0.	0.
	0.	0.	0.	0.	0.	0.	0.	0.	0.	0.	0.
120.5	0.	0.	0.	0.	0.	0.	0.	0.	0.	0.	0.
	0.	0.	0.	0.	0.	0.	0.	0.	0.	0.	0.
	1.	0.	1.	0.	1.	0.	1.	0.	0.	0.	0.
	672.	967.	862.	621.	449.	313.	225.	139.	102.	56.	
	1313.	1819.	1524.	1264.	917.	682.	453.	322.	232.	134.	
125.5	812.	1249.	1210.	969.	738.	559.	361.	281.	183.	97.	
	545.	846.	884.	772.	558.	453.	305.	200.	149.	104.	
	376.	611.	636.	525.	495.	374.	258.	196.	124.	98.	
	252.	449.	510.	452.	412.	298.	206.	162.	110.	70.	
	159.	313.	398.	365.	291.	252.	188.	138.	89.	56.	
130.5	97.	232.	264.	278.	272.	207.	164.	100.	68.	65.	
	67.	153.	192.	226.	187.	164.	135.	85.	72.	43.	
	56.	112.	138.	179.	145.	144.	118.	88.	48.	34.	
	34.	80.	119.	124.	134.	118.	88.	58.	33.	33.	
	16.	58.	102.	117.	107.	94.	68.	57.	42.	33.	
135.5	9.	40.	59.	76.	89.	85.	80.	47.	46.	29.	
	3.	17.	54.	62.	51.	66.	50.	43.	25.	22.	
	4.	15.	33.	52.	39.	40.	37.	24.	24.	21.	
	0.	0.	1.	0.	1.	0.	2.	1.	1.	0.	
	0.	0.	1.	0.	0.	0.	0.	0.	0.	0.	
140.5	0.	0.	0.	1.	1.	0.	0.	0.	0.	0.	
	0.	0.	0.	1.	1.	0.	0.	0.	0.	0.	

Charged data, vacuum beam, set 1

E =	35	45	55	65	75	85	95	105	115	125	GeV
z = 110.5 m	0.	0.	0.	0.	0.	0.	0.	0.	0.	0.	0.
	0.	0.	0.	0.	0.	0.	0.	0.	0.	0.	0.
	0.	0.	0.	0.	0.	0.	0.	0.	0.	0.	0.
	0.	0.	0.	0.	0.	0.	0.	0.	0.	0.	0.
	0.	0.	0.	0.	0.	0.	0.	0.	0.	0.	0.
115.5	0.	0.	0.	0.	0.	0.	0.	0.	0.	0.	0.
	0.	0.	0.	0.	0.	0.	0.	0.	0.	0.	0.
	0.	0.	0.	0.	0.	0.	0.	0.	0.	0.	0.
	0.	0.	0.	0.	0.	0.	0.	0.	0.	0.	0.
	0.	0.	0.	0.	0.	0.	0.	0.	0.	0.	0.
120.5	2.	6.	9.	4.	6.	7.	5.	1.	3.	1.	
	38.	50.	56.	54.	55.	33.	25.	19.	11.	13.	
	34.	51.	76.	68.	45.	35.	34.	34.	17.	13.	
	41.	63.	58.	57.	50.	48.	33.	25.	18.	13.	
	51.	77.	64.	62.	56.	42.	36.	29.	15.	10.	
125.5	59.	70.	75.	68.	56.	58.	29.	32.	11.	21.	
	40.	78.	83.	60.	59.	40.	27.	36.	14.	6.	
	52.	78.	70.	65.	59.	40.	27.	23.	22.	7.	
	58.	77.	77.	57.	66.	48.	50.	26.	18.	17.	
	61.	76.	85.	60.	66.	36.	28.	26.	9.	11.	
130.5	63.	91.	70.	55.	51.	41.	28.	20.	7.	19.	
	67.	57.	81.	76.	59.	51.	34.	12.	18.	10.	
	73.	92.	73.	65.	59.	37.	30.	31.	17.	16.	
	56.	84.	73.	61.	43.	29.	23.	17.	17.	8.	
	64.	82.	76.	53.	56.	30.	28.	12.	12.	9.	
135.5	61.	91.	65.	63.	57.	38.	23.	20.	11.	12.	
	55.	79.	77.	76.	53.	23.	33.	22.	14.	7.	
	52.	89.	83.	73.	50.	36.	29.	17.	11.	10.	
	48.	63.	46.	50.	44.	37.	16.	18.	18.	5.	
	1.	1.	1.	1.	0.	2.	0.	0.	0.	1.	
140.5	0.	3.	1.	2.	1.	0.	0.	0.	0.	0.	
	3.	2.	3.	0.	1.	2.	1.	0.	0.	2.	

Table 3, cont. Charged mode data before background subtraction.

Charged data, vacuum beam, set 2

E =	35	45	55	65	75	85	95	105	115	125 GeV
z = 110.5 m	0.	0.	0.	0.	0.	3.	3.	9.	8.	12.
	0.	0.	0.	0.	1.	4.	5.	14.	8.	11.
	0.	0.	0.	0.	3.	9.	13.	16.	17.	13.
	0.	0.	0.	4.	10.	14.	23.	16.	15.	15.
115.5	0.	1.	1.	7.	20.	23.	25.	23.	16.	14.
	0.	1.	9.	13.	31.	31.	29.	30.	14.	15.
	0.	5.	19.	31.	42.	36.	41.	24.	26.	20.
	2.	29.	41.	60.	65.	46.	36.	29.	19.	20.
120.5	11.	45.	61.	78.	47.	52.	46.	25.	19.	22.
	25.	67.	78.	85.	73.	56.	35.	24.	16.	16.
	36.	80.	92.	70.	68.	53.	36.	31.	21.	16.
	52.	102.	87.	84.	60.	53.	37.	22.	21.	18.
125.5	46.	89.	90.	83.	81.	61.	43.	40.	24.	14.
	68.	96.	99.	88.	64.	57.	43.	28.	23.	12.
	58.	126.	89.	89.	70.	49.	43.	33.	15.	25.
	66.	101.	108.	84.	61.	58.	32.	34.	25.	14.
130.5	78.	93.	82.	87.	65.	46.	34.	35.	21.	16.
	73.	109.	108.	81.	65.	59.	41.	22.	16.	10.
	57.	107.	96.	82.	61.	47.	39.	17.	20.	12.
	77.	104.	108.	79.	57.	59.	29.	28.	19.	17.
135.5	70.	103.	87.	69.	60.	59.	34.	32.	17.	9.
	84.	79.	105.	86.	54.	47.	40.	22.	21.	15.
	75.	92.	95.	94.	49.	40.	40.	17.	20.	14.
	76.	77.	88.	80.	62.	44.	32.	30.	19.	20.
140.5	77.	93.	104.	90.	46.	51.	38.	18.	15.	11.
	76.	127.	93.	71.	59.	42.	37.	35.	21.	4.
	78.	96.	94.	92.	75.	41.	38.	19.	14.	14.
	66.	80.	70.	61.	58.	36.	26.	27.	13.	11.
140.5	1.	2.	1.	2.	1.	2.	0.	1.	0.	0.
	1.	1.	1.	2.	1.	1.	2.	1.	0.	1.
	1.	1.	0.	1.	0.	1.	0.	0.	1.	0.

Charged data, vacuum beam, set 3

E =	35	45	55	65	75	85	95	105	115	125 GeV
z = 110.5 m	0.	0.	0.	0.	0.	1.	5.	6.	7.	9.
	0.	0.	0.	0.	0.	10.	9.	16.	15.	5.
	0.	0.	0.	2.	3.	6.	16.	20.	15.	15.
	0.	0.	0.	3.	7.	25.	27.	17.	17.	9.
115.5	0.	0.	3.	12.	24.	32.	39.	26.	17.	22.
	0.	0.	13.	25.	32.	26.	41.	29.	33.	14.
	0.	5.	34.	49.	47.	40.	27.	35.	32.	19.
	1.	29.	51.	54.	53.	52.	48.	36.	29.	14.
120.5	16.	49.	80.	70.	66.	75.	41.	45.	30.	25.
	22.	61.	81.	101.	80.	48.	43.	39.	36.	19.
	46.	83.	103.	93.	87.	71.	46.	34.	29.	13.
	40.	105.	104.	81.	67.	56.	50.	37.	21.	16.
125.5	59.	94.	87.	107.	78.	53.	53.	41.	42.	21.
	74.	87.	106.	87.	69.	50.	52.	37.	22.	19.
	60.	114.	99.	84.	79.	75.	45.	40.	28.	23.
	68.	94.	105.	82.	66.	64.	52.	30.	23.	13.
130.5	79.	116.	102.	94.	66.	67.	49.	35.	26.	24.
	84.	121.	122.	76.	71.	51.	38.	33.	31.	18.
	85.	109.	108.	105.	96.	68.	41.	33.	25.	21.
	85.	106.	108.	89.	77.	51.	54.	39.	15.	13.
135.5	68.	138.	106.	107.	71.	55.	42.	41.	20.	15.
	81.	134.	107.	93.	68.	63.	45.	27.	20.	22.
	72.	103.	109.	94.	73.	70.	38.	23.	18.	13.
	77.	101.	119.	101.	57.	54.	41.	27.	22.	13.
140.5	94.	128.	97.	94.	70.	64.	36.	26.	20.	15.
	90.	106.	93.	71.	78.	61.	35.	24.	22.	16.
	102.	120.	105.	87.	78.	47.	40.	29.	21.	13.
	76.	112.	87.	58.	54.	33.	35.	23.	18.	9.
140.5	4.	3.	1.	0.	5.	1.	0.	1.	1.	0.
	1.	1.	4.	3.	1.	1.	0.	0.	1.	0.
	3.	3.	4.	2.	2.	0.	0.	2.	0.	0.

Table 4. Neutral mode data before background subtraction.

Neutral data, regenerated beam

E =	45	55	65	75	85	95	105	115	125	GeV
z = 115.5 m	0.	0.	0.	0.	0.	0.	0.	0.	0.	0.
	0.	0.	0.	0.	0.	0.	0.	0.	0.	0.
	0.	0.	0.	1.	0.	0.	0.	0.	0.	0.
	0.	2.	0.	1.	0.	0.	2.	0.	0.	0.
120.5	6.	5.	4.	2.	2.	2.	1.	0.	0.	0.
	10.	23.	29.	14.	10.	5.	4.	3.	0.	0.
	46.	112.	119.	71.	55.	40.	14.	11.	8.	8.
	141.	257.	262.	221.	142.	86.	55.	25.	8.	8.
125.5	214.	422.	440.	302.	190.	138.	83.	40.	21.	21.
	255.	483.	518.	394.	268.	174.	72.	50.	23.	23.
	214.	425.	437.	354.	225.	129.	58.	42.	21.	21.
	198.	326.	396.	263.	178.	121.	59.	28.	11.	11.
130.5	158.	243.	259.	215.	137.	90.	43.	15.	12.	12.
	110.	218.	183.	173.	113.	69.	31.	25.	5.	5.
	85.	184.	175.	144.	93.	64.	48.	13.	7.	7.
	59.	128.	142.	105.	68.	38.	19.	16.	6.	6.
135.5	54.	102.	111.	81.	59.	36.	14.	4.	2.	2.
	36.	75.	73.	64.	37.	30.	19.	4.	5.	5.
	32.	48.	68.	43.	33.	26.	15.	9.	6.	6.
	19.	41.	44.	37.	37.	14.	9.	6.	4.	4.
140.5	12.	38.	36.	32.	18.	11.	4.	4.	0.	0.
	11.	21.	19.	9.	21.	6.	1.	3.	1.	1.
	5.	8.	6.	6.	5.	0.	1.	2.	2.	2.
	1.	2.	1.	1.	1.	0.	1.	0.	0.	0.

Neutral data, vacuum beam

E =	45	55	65	75	85	95	105	115	125	GeV
z = 110.5 m	0.	0.	0.	0.	0.	0.	1.	0.	0.	0.
	0.	0.	0.	0.	0.	0.	0.	0.	0.	0.
	0.	0.	0.	0.	2.	3.	1.	3.	0.	0.
	0.	0.	1.	1.	2.	0.	5.	2.	2.	2.
115.5	0.	0.	2.	2.	4.	0.	7.	2.	4.	4.
	1.	1.	7.	9.	5.	8.	12.	4.	3.	3.
	0.	7.	9.	12.	16.	11.	11.	11.	6.	6.
	3.	10.	13.	19.	20.	16.	7.	9.	5.	5.
120.5	5.	23.	30.	21.	22.	12.	16.	9.	5.	5.
	9.	30.	35.	25.	21.	20.	12.	10.	5.	5.
	3.	21.	51.	38.	35.	20.	14.	7.	8.	8.
	16.	27.	44.	40.	33.	13.	12.	3.	8.	8.
125.5	17.	30.	44.	42.	29.	27.	7.	11.	9.	9.
	20.	45.	39.	45.	34.	25.	16.	8.	2.	2.
	18.	56.	53.	31.	28.	13.	13.	15.	3.	3.
	21.	34.	55.	44.	27.	19.	6.	3.	2.	2.
130.5	27.	39.	51.	42.	27.	20.	10.	11.	2.	2.
	22.	37.	43.	49.	38.	14.	12.	8.	6.	6.
	33.	51.	50.	41.	26.	17.	12.	7.	2.	2.
	40.	47.	57.	34.	25.	24.	11.	6.	3.	3.
135.5	39.	56.	42.	34.	24.	12.	8.	3.	3.	3.
	24.	55.	55.	23.	21.	10.	4.	4.	4.	4.
	49.	53.	43.	26.	24.	13.	7.	3.	1.	1.
	47.	63.	54.	37.	11.	12.	9.	4.	0.	0.
140.5	49.	53.	44.	37.	15.	14.	5.	2.	0.	0.
	49.	45.	34.	24.	10.	8.	3.	3.	2.	2.
	33.	40.	36.	17.	16.	2.	1.	0.	0.	0.
	16.	20.	8.	8.	6.	1.	0.	2.	0.	0.

Chapter 6

EXTRACTING THE PHASE DIFFERENCE

6.1 Outline of the method

With the data sets in hand, we shall now discuss our strategy for extracting the phase difference. Recall from above that we wished to fit the data to the decay spectrum

$$|\rho|^2 e^{-\Gamma_S \tau} + 2|\rho||\eta| e^{-(\Gamma_S + \Gamma_L)\tau/2} \cos(\Delta m \tau + \phi_\rho - \phi_\eta) + |\eta|^2 e^{-\Gamma_L \tau}.$$

Since the proper time is given by $\tau = mc z / E$, where m is the kaon mass and z is the distance of the decay from the regenerator, one natural way to do this is to divide the data into (E, z) bins (10 GeV by 1 m) and to fit for ϕ_η in each energy bin. To compare the data with the true spectrum, however, we would need to correct for the effects of our detector acceptance and analysis reconstruction efficiency, determined, for example, by a Monte Carlo detector simulation. At that point, we would have to consider the effects of resolution smearing, especially in the neutral mode where we have already seen that the effects are not small. With perfect resolution, the expected z distribution for events downstream of a regenerator would be a knife edge at the regenerator position followed by an exponential. This was not a good approximation to our data, as seen in Figure 44. Regenerated events upstream of the regenerator would not have well-defined acceptances since no events were generated there. The problem could not be solved simply by ignoring the events upstream of the decay volume, however. The steepness of the decay spectrum downstream of the regenerator would give smearing in the decay vertex distribution that pushed events systematically from lower z to higher. This had to be treated properly as well.

Our answer to these concerns was to correct the data for background only, comparing the resulting $z(E)$ distributions with those generated by a Monte Carlo simulation. If the Monte Carlo agreement was good enough, any differences between data and Monte Carlo would be from the difference between the true phase and the one used to generate the Monte Carlo events. We could then vary the ϕ_η with which the Monte Carlo events were generated until we found the best match to the data. The method we used to vary this phase will be described below. The Monte Carlo, then, played an important role in the phase analysis; we shall therefore describe it in more detail before proceeding with our discussion of the phase difference extraction.

6.2 The Monte Carlo simulation

The Monte Carlo generated kaons at a target with a geometry like that used in the experiment. A momentum and direction for the kaon were chosen from a distribution of momenta and production angles,¹⁶ taking into account decays upstream of the decay volume as well as modeling a boron carbide/lead regenerator with the proper geometry placed in the designated regenerated beam. No scattering was given to the kaon in the regenerator. The kaon was traced from the target through a set of defining collimators and allowed to decay according to the proper time spectrum appropriate to either a vacuum or regenerated beam decay.

For charged events, two pions were generated and tracked through the detector. Decays upstream of the regenerator were subjected to aperture cuts on the pion positions at the lead mask, the upstream and downstream ends of the regenerator, and the HDRA. The pion directions were changed by multiple scattering in both the T and V counters. Events in which one of the pions decayed in flight upstream of the first drift chamber were discarded if the muon had less than 10 GeV of energy. (Events with more energetic

muons would have been eliminated at the trigger level.) Further multiple scattering occurred at the vacuum window, drift chambers, and the A and B banks. Aperture cuts on the pion tracks were imposed at these places too, and at the height of the magnet opening. The appropriate transverse kick was applied at the analyzing magnet. The probability of pion decay was checked as above from chamber 1 to the lead glass. Hits were generated in the proper A and B bank counters, and the trigger topology $2B \cdot (B_E \cdot B_W) \cdot (A_E \cdot A_W)$ was demanded. Allowances were made for tracks to be lost in cracks between adjacent counters in each bank. At this point track hits were digitized and wire inefficiencies included.

The events were then written to tape in the same format as that generated by the first pass data analysis. This allowed us to analyze data and Monte Carlo events with essentially the same second and third stage event reconstructions. The only difference in the second stage analysis for Monte Carlo events was that no corrections were made for chamber rotations or transit times along chamber wires or B bank counters. The third stage analysis was identical for data and Monte Carlo events.

The momentum, direction, and decay vertex were determined for neutral events as they were for charged events. The K was then allowed to decay to two π^0 's, each of which in turn decayed into two photons. A photon conversion in the lead sheet was assumed for every event; the randomly-chosen converted photon had to have an energy of at least 0.4 GeV, while each of the other photons needed 1.6 GeV. All four photons had to pass mask, RA, HDRA, and magnet (vertical direction only) aperture cuts and an additional cut at VA2. The photon directions were extrapolated to the glass; events containing photons which missed the outer edge were discarded. Photons near the inner edges which hit our simulated collar anti had a 91% chance of converting in the three radiation lengths of copper; the energy of photons which traveled down the pipes was

accumulated in the back anti until it exceeded the 5 GeV energy limit imposed by the analysis, at which time the event was rejected.

The converted photon was treated separately. An electron-positron pair and *bremstrahlung* photon were created at the lead sheet. The brem was checked for possible energy deposits in the CA and BA, while the trajectories of the pair were generally checked as those of the charged pions had been. Since the pair was created downstream of the V counter, we considered multiple scattering only in the lead and scattering sources downstream of it. The appropriate momentum kicks were applied at both the separator and analyzing magnets. Once we had checked that the pair would successfully reach the glass, we enforced the neutral trigger topology of two hits in the A bank and one or two hits in the B bank. We again considered the possibility that the tracks could have passed through A and B bank cracks.

Before kaon reconstruction, it was necessary to model the electromagnetic shower process in more detail than just smearing the cluster energies. Clusters were generated for the three photons, electron pair, and *bremstrahlung* photon by dividing the photon or electron energy among blocks in a 5 block \times 5 block cluster around the cluster center. The amounts of energy sharing were taken from a table compiled in a previous study of shower development in our lead glass. Adjustments were made in individual block energies to reflect fluctuations from photon statistics and shower depth in the glass.

The clusters were then reconstructed as they had been in the first pass of the analysis using the standard cluster finder. Track/cluster matching was done essentially as it was in the first pass analysis, although no adder cut was imposed. Tracks were again required to match one or two clusters, with an additional three clusters left over. Events in which tracks went down the beam pipes in the glass were rejected. The drift chamber data was simulated as it was for charged decay events.

The second pass analysis for the neutral Monte Carlo events differed from that for the data only in not making additional veto cuts on events with activity in the various veto counters and on events with large numbers of hits in the drift chambers. Energy sharing between the layers in the BA was also neglected. Note that the total BA energy cut and the CA cut were already done in the Monte Carlo, as were the aperture cuts that precluded activity in VA3 and DRAN. As in the charged mode analysis, we adjusted chamber data only for drift time and not for offsets and transit times.

The final stage of the analysis of neutral Monte Carlo events differed from the analysis of data events in more substantial ways than it had in charged, mostly in the corrections to cluster energies. First the Monte Carlo cluster energies were additionally smeared, as the Monte Carlo energy smearing ($1\% + 5\%/\sqrt{E}$) was smaller than we had observed. Then the cluster energies were increased by 2.4% to give a 3 block \times 3 block cluster with the energy of the original 5 \times 5 cluster. (This correction took into account that the calibration for the data assumed that a 3 \times 3 cluster contained all of the energy.) The Monte Carlo cluster generation procedure introduced an average 1.4% energy scale difference between electron and photon clusters, so we corrected the simulated events for nonlinearity in the same way as we had the data, although we took a to be 1.000 for electrons and 1/1.014 for photons. There was no overall energy scale factor needed for the Monte Carlo events.

Figures 57 and 58 show the reconstructed energy distributions for both data and Monte Carlo. A slight offset is visible in both charged and neutral modes. Figures 59 and 60 show the vertex z distributions for data and Monte Carlo at three representative energies for each mode. Tables 5 and 6 show the Monte Carlo event populations used in this analysis.

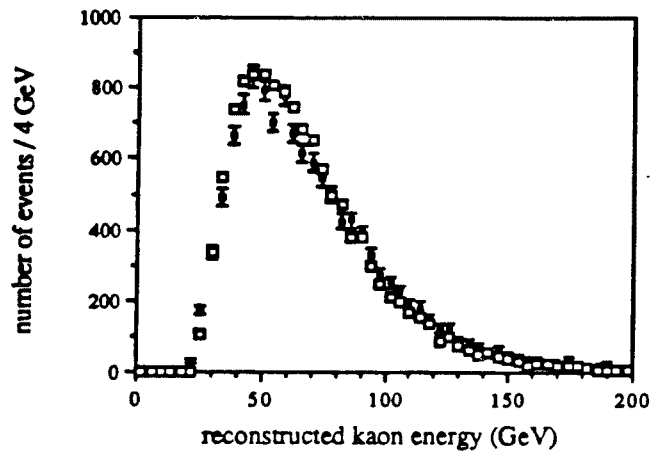


Figure 57. Comparison of reconstructed energy spectra from data and Monte Carlo for the third set vacuum charged mode events. The solid blocks with error bars indicate the data; the open blocks indicate the Monte Carlo.

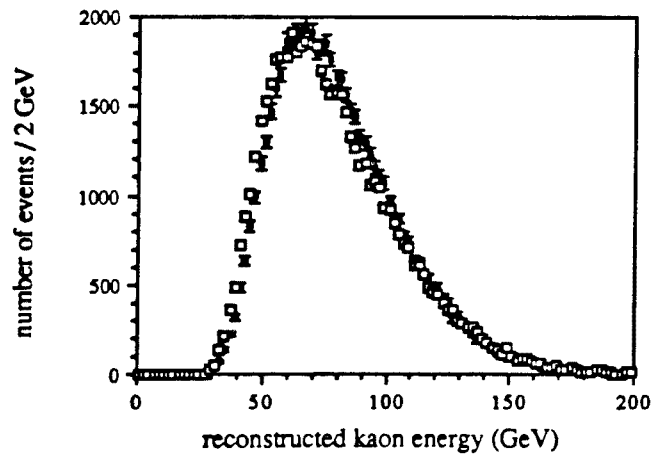


Figure 58. Comparison of reconstructed energy spectra from neutral vacuum data and Monte Carlo events. The solid blocks indicate the data; the open blocks indicate the Monte Carlo.

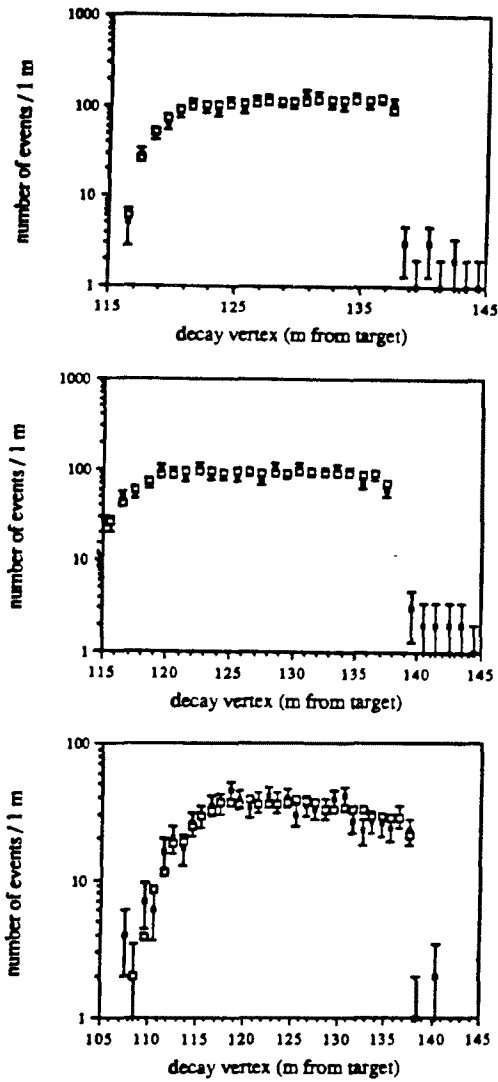


Figure 59. Comparison of reconstructed z vertex for charged data and Monte Carlo vacuum events. These represent the third set of charged mode data. The top graph is for kaon energies of 40–50 GeV; the middle, 60–70 GeV; the bottom, 100–110 GeV. Solid blocks are data; open blocks are Monte Carlo.

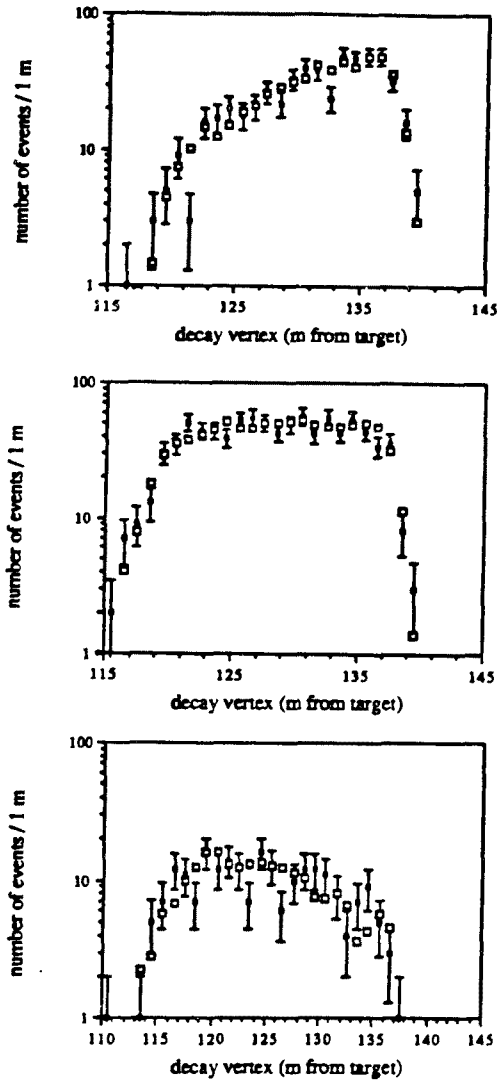


Figure 60. Comparison of reconstructed z vertex for neutral data and Monte Carlo vacuum events. The top graph is for kaon energies of 40–50 GeV; the middle, 60–70 GeV; the bottom, 100–110 GeV. Solid blocks are data; open blocks are Monte Carlo.

Table 5. Charged mode Monte Carlo events.

Charged MC, regenerated beam, set 1

E =	35	45	55	65	75	85	95	105	115	125 GeV
z = 115.5 m	0.	0.	0.	0.	0.	0.	0.	0.	0.	0.
	0.	0.	0.	0.	0.	0.	0.	0.	0.	0.
	0.	0.	0.	0.	0.	0.	0.	0.	0.	0.
	0.	0.	0.	0.	0.	0.	0.	0.	0.	0.
120.5	0.	0.	0.	0.	0.	0.	0.	0.	0.	0.
	0.	0.	0.	0.	0.	0.	0.	0.	0.	0.
	0.	0.	0.	0.	0.	1.	0.	0.	1.	0.
	4.	5.	8.	9.	9.	7.	8.	4.	3.	4.
	5107.	6188.	5166.	3829.	2548.	1827.	1187.	781.	518.	367.
	9388.	11908.	10217.	8036.	5638.	3789.	2652.	1703.	1196.	734.
125.5	6240.	8535.	7631.	6049.	4555.	3165.	2169.	1510.	987.	612.
	4119.	5919.	5694.	4775.	3571.	2505.	1898.	1223.	827.	576.
	2737.	4183.	4228.	3753.	2947.	2119.	1563.	1021.	719.	530.
	1825.	2886.	3276.	2931.	2294.	1817.	1298.	917.	632.	430.
	1142.	2045.	2447.	2205.	1893.	1521.	1109.	712.	511.	358.
130.5	762.	1588.	1848.	1756.	1573.	1263.	1001.	662.	464.	335.
	479.	1122.	1375.	1350.	1199.	968.	785.	548.	408.	267.
	316.	777.	1016.	1107.	977.	808.	601.	436.	320.	261.
	186.	530.	839.	811.	817.	673.	535.	422.	285.	209.
	128.	379.	625.	710.	680.	577.	439.	284.	262.	180.
135.5	67.	284.	446.	563.	571.	487.	343.	298.	210.	150.
	44.	184.	361.	432.	456.	378.	328.	260.	189.	143.
	27.	111.	162.	302.	287.	248.	218.	163.	131.	103.
	0.	0.	0.	0.	0.	2.	3.	1.	0.	1.
	0.	0.	0.	0.	0.	0.	0.	0.	0.	0.
140.5	0.	0.	0.	0.	0.	0.	0.	0.	0.	0.

Charged MC, regenerated beam, set 2

E =	35	45	55	65	75	85	95	105	115	125 GeV
z = 115.5 m	0.	0.	0.	0.	0.	0.	0.	0.	0.	0.
	0.	0.	0.	0.	0.	0.	0.	0.	0.	0.
	0.	0.	0.	0.	0.	0.	0.	0.	0.	0.
	0.	0.	0.	0.	0.	0.	0.	0.	0.	0.
120.5	0.	0.	0.	0.	0.	0.	0.	0.	0.	0.
	0.	0.	0.	0.	0.	0.	0.	0.	0.	0.
	2.	4.	8.	3.	15.	5.	8.	4.	5.	3.
	5282.	6021.	5137.	3807.	2621.	1797.	1209.	798.	524.	352.
	9407.	11975.	10474.	7861.	5500.	3892.	2714.	1779.	1093.	781.
125.5	6238.	8292.	7767.	6150.	4509.	3259.	2217.	1597.	958.	690.
	4101.	5928.	5835.	4667.	3576.	2628.	1794.	1236.	857.	624.
	2745.	4219.	4335.	3581.	2940.	2132.	1557.	1109.	718.	497.
	1796.	2954.	3176.	2932.	2316.	1757.	1291.	888.	581.	415.
	1191.	2089.	2426.	2231.	1897.	1482.	1080.	789.	501.	391.
130.5	770.	1499.	1855.	1792.	1531.	1249.	907.	674.	475.	346.
	489.	1064.	1346.	1361.	1175.	942.	796.	536.	382.	291.
	309.	742.	1048.	1135.	1021.	821.	621.	434.	354.	249.
	193.	536.	770.	889.	768.	701.	592.	431.	312.	224.
	129.	417.	611.	673.	661.	542.	436.	347.	252.	220.
135.5	71.	262.	439.	523.	518.	482.	402.	297.	218.	157.
	46.	187.	355.	463.	428.	394.	345.	240.	193.	141.
	23.	109.	211.	286.	298.	277.	192.	186.	140.	100.
	0.	0.	1.	0.	1.	2.	2.	4.	1.	0.
	0.	0.	0.	0.	0.	0.	0.	0.	0.	0.
140.5	0.	0.	0.	0.	0.	0.	0.	0.	0.	0.

Table 5, cont.

Charged MC, regenerated beam, set 3

E =	35	45	55	65	75	85	95	105	115	125 GeV
z = 115.5 m	0.	0.	0.	0.	0.	0.	0.	0.	0.	0.
	0.	0.	0.	0.	0.	0.	0.	0.	0.	0.
	0.	0.	0.	0.	0.	0.	0.	0.	0.	0.
	0.	0.	0.	0.	0.	0.	0.	0.	0.	0.
120.5	0.	0.	0.	0.	0.	0.	0.	0.	0.	0.
	0.	0.	0.	0.	0.	0.	0.	0.	0.	0.
	1.	4.	6.	6.	2.	3.	6.	4.	3.	4.
	4949.	6012.	5195.	3727.	2656.	1823.	1213.	820.	533.	357.
125.5	9358.	12136.	10368.	7788.	5598.	3903.	2615.	1792.	1170.	782.
	6258.	8512.	7724.	6228.	4543.	3252.	2088.	1482.	998.	705.
	4135.	5851.	5655.	4801.	3577.	2631.	1854.	1286.	897.	624.
	2589.	4188.	4272.	3777.	2974.	2168.	1517.	1051.	729.	542.
	1803.	3048.	3190.	2881.	2325.	1724.	1314.	907.	612.	435.
130.5	1175.	2136.	2440.	2303.	1914.	1482.	1130.	775.	545.	389.
	754.	1465.	1838.	1759.	1567.	1174.	931.	646.	484.	324.
	520.	1051.	1376.	1460.	1241.	959.	759.	522.	391.	306.
	342.	738.	1077.	1070.	1003.	807.	649.	480.	372.	246.
	201.	534.	762.	892.	812.	710.	510.	387.	307.	221.
135.5	128.	367.	617.	687.	675.	587.	463.	345.	249.	194.
	72.	243.	449.	544.	562.	484.	362.	294.	221.	147.
	38.	165.	370.	393.	447.	388.	334.	239.	205.	125.
	17.	123.	200.	309.	287.	242.	212.	168.	144.	107.
	0.	0.	0.	0.	1.	0.	2.	1.	1.	1.
140.5	0.	0.	0.	0.	0.	0.	0.	0.	0.	0.
	0.	0.	0.	0.	0.	0.	0.	0.	0.	0.

Charged MC, vacuum beam, set 1

E =	35	45	55	65	75	85	95	105	115	125 GeV
z = 110.5 m	0.	0.	1.	7.	6.	27.	64.	114.	152.	131.
	0.	0.	6.	6.	17.	61.	146.	187.	192.	178.
	0.	4.	10.	15.	77.	148.	237.	272.	235.	209.
	1.	6.	6.	46.	186.	317.	333.	362.	294.	254.
115.5	0.	1.	47.	187.	341.	463.	464.	445.	335.	307.
	1.	17.	165.	426.	588.	627.	546.	502.	383.	321.
	3.	117.	482.	757.	792.	757.	645.	531.	366.	329.
	46.	437.	956.	1028.	967.	856.	724.	561.	436.	326.
	229.	848.	1233.	1283.	1157.	989.	772.	608.	453.	342.
120.5	504.	1232.	1657.	1499.	1308.	1002.	817.	579.	462.	314.
	786.	1571.	1880.	1595.	1318.	1004.	784.	603.	450.	310.
	1025.	1749.	1841.	1634.	1350.	1036.	809.	584.	388.	340.
	1074.	1840.	1836.	1629.	1301.	1034.	787.	599.	419.	311.
	1186.	1923.	1844.	1636.	1316.	1039.	790.	592.	451.	288.
125.5	1275.	1817.	1783.	1537.	1294.	1010.	759.	583.	402.	281.
	1359.	1911.	1896.	1667.	1308.	976.	770.	611.	441.	295.
	1412.	1869.	1882.	1714.	1377.	953.	820.	564.	415.	295.
	1457.	2038.	1858.	1695.	1334.	995.	728.	547.	435.	284.
	1556.	2018.	1854.	1678.	1269.	1005.	779.	487.	410.	267.
130.5	1525.	1932.	1933.	1660.	1316.	936.	763.	560.	394.	299.
	1664.	1983.	1880.	1607.	1280.	1013.	704.	577.	397.	276.
	1705.	2101.	1951.	1641.	1344.	951.	729.	517.	383.	281.
	1741.	2083.	1879.	1565.	1296.	877.	677.	511.	354.	238.
	1840.	2101.	1975.	1625.	1317.	945.	690.	520.	368.	271.
135.5	1789.	2123.	1991.	1688.	1305.	1010.	711.	486.	347.	258.
	1821.	2060.	1933.	1570.	1275.	942.	650.	487.	322.	264.
	1858.	2134.	1975.	1588.	1235.	909.	630.	510.	371.	235.
	1437.	1706.	1546.	1264.	1011.	706.	545.	355.	260.	197.
	1.	3.	3.	3.	2.	7.	3.	2.	1.	2.
140.5	0.	0.	0.	0.	0.	0.	0.	0.	0.	0.
	0.	0.	0.	0.	0.	0.	0.	0.	0.	0.

Table 5, cont.

Charged MC, vacuum beam, set 2

E =	35	45	55	65	75	85	95	105	115	125 GeV
z = 110.5 m	0.	1.	4.	5.	5.	27.	81.	109.	130.	149.
	0.	2.	8.	5.	19.	69.	151.	210.	218.	185.
	0.	1.	4.	8.	49.	152.	221.	273.	245.	227.
115.5	0.	5.	10.	52.	177.	300.	346.	308.	313.	259.
	0.	6.	34.	172.	360.	424.	491.	395.	323.	217.
	0.	21.	163.	439.	573.	629.	538.	490.	382.	313.
120.5	1.	116.	462.	736.	795.	701.	599.	508.	403.	328.
	36.	457.	895.	1059.	1003.	877.	747.	558.	435.	367.
	244.	854.	1228.	1275.	1163.	951.	769.	611.	480.	320.
125.5	493.	1286.	1596.	1546.	1305.	1013.	810.	647.	475.	302.
	791.	1645.	1741.	1627.	1307.	1054.	811.	593.	435.	314.
	1027.	1668.	1831.	1631.	1354.	1070.	787.	609.	442.	314.
130.5	1088.	1722.	1857.	1654.	1364.	1003.	774.	582.	416.	318.
	1149.	1789.	1848.	1695.	1366.	975.	840.	578.	426.	285.
	1281.	1886.	1865.	1622.	1298.	1072.	789.	610.	448.	292.
135.5	1405.	1918.	1855.	1622.	1324.	1000.	790.	579.	442.	330.
	1432.	1973.	1881.	1612.	1307.	994.	789.	572.	411.	295.
	1475.	1952.	1922.	1684.	1283.	1021.	794.	516.	379.	304.
140.5	1543.	1999.	1915.	1615.	1328.	1006.	740.	515.	386.	279.
	1588.	1938.	1884.	1662.	1371.	974.	746.	561.	408.	266.
	1622.	2017.	1917.	1649.	1287.	994.	733.	506.	388.	288.
145.5	1708.	2016.	1931.	1655.	1298.	916.	694.	535.	361.	280.
	1686.	2078.	1983.	1575.	1309.	1002.	746.	490.	406.	299.
	1774.	2021.	1905.	1640.	1191.	952.	672.	489.	378.	256.
150.5	1750.	2099.	1955.	1514.	1320.	986.	713.	482.	348.	289.
	1819.	2059.	1940.	1582.	1204.	884.	685.	465.	341.	272.
	1775.	2137.	1902.	1589.	1245.	929.	712.	441.	330.	258.
155.5	1541.	1679.	1531.	1258.	1000.	720.	550.	368.	239.	178.
	0.	0.	4.	4.	7.	1.	4.	3.	6.	1.

Charged MC, vacuum beam, set 3

E =	35	45	55	65	75	85	95	105	115	125 GeV
z = 110.5 m	0.	1.	3.	2.	2.	21.	69.	138.	138.	153.
	0.	0.	2.	5.	21.	69.	148.	186.	207.	191.
	0.	3.	3.	9.	50.	149.	238.	297.	245.	202.
115.5	0.	1.	8.	61.	195.	300.	328.	310.	291.	230.
	0.	2.	43.	188.	368.	462.	465.	394.	315.	313.
	1.	14.	157.	465.	591.	576.	585.	472.	355.	314.
120.5	3.	106.	457.	741.	812.	738.	709.	521.	421.	348.
	64.	461.	903.	1050.	989.	881.	729.	586.	440.	340.
	231.	934.	1304.	1330.	1165.	995.	783.	589.	477.	342.
125.5	546.	1321.	1591.	1535.	1256.	1040.	786.	584.	444.	341.
	805.	1630.	1771.	1556.	1364.	1080.	809.	636.	471.	303.
	1007.	1744.	1773.	1661.	1376.	1146.	794.	569.	408.	308.
130.5	1077.	1812.	1845.	1652.	1322.	992.	803.	581.	430.	332.
	1130.	1862.	1787.	1714.	1335.	1035.	812.	573.	419.	308.
	1251.	1863.	1902.	1600.	1367.	1081.	737.	597.	454.	303.
135.5	1364.	1902.	1821.	1666.	1374.	1017.	817.	620.	408.	283.
	1405.	1923.	1882.	1673.	1372.	1060.	767.	610.	411.	286.
	1432.	1971.	1934.	1636.	1342.	1040.	757.	585.	388.	279.
140.5	1555.	1965.	1913.	1628.	1331.	1041.	755.	533.	394.	302.
	1587.	1976.	1936.	1650.	1287.	1018.	731.	532.	405.	271.
	1559.	1999.	1933.	1693.	1296.	953.	759.	538.	392.	252.
145.5	1681.	2071.	1920.	1665.	1251.	977.	708.	531.	368.	264.
	1777.	2118.	1945.	1596.	1218.	916.	709.	525.	387.	271.
	1841.	2079.	1988.	1637.	1249.	923.	665.	472.	330.	279.
150.5	1756.	2050.	1914.	1612.	1297.	912.	708.	476.	364.	257.
	1763.	2051.	2030.	1549.	1268.	905.	715.	461.	339.	266.
	1809.	2141.	1879.	1633.	1227.	925.	638.	461.	316.	219.
155.5	1519.	1650.	1625.	1256.	938.	732.	498.	340.	242.	199.
	1.	1.	7.	3.	4.	1.	5.	1.	3.	0.

Table 6. Neutral mode Monte Carlo events.

		Neutral MC, regenerated beam									
E =		45	55	65	75	85	95	105	115	125	GeV
z = 115.5 m		0.	0.	0.	0.	0.	0.	0.	0.	0.	0.
		0.	0.	0.	0.	0.	0.	0.	0.	0.	0.
		0.	0.	0.	0.	0.	0.	0.	0.	0.	0.
		0.	0.	1.	0.	2.	0.	0.	0.	0.	0.
120.5		0.	3.	1.	1.	2.	3.	1.	0.	0.	
		4.	13.	8.	7.	6.	6.	4.	0.	2.	
		22.	56.	50.	38.	37.	27.	9.	9.	2.	
		107.	212.	215.	180.	105.	64.	42.	22.	8.	
125.5		272.	561.	575.	406.	287.	180.	97.	43.	30.	
		521.	946.	927.	729.	450.	281.	159.	86.	34.	
		574.	1082.	1069.	787.	504.	290.	152.	68.	40.	
		545.	896.	907.	679.	455.	244.	143.	66.	22.	
130.5		453.	741.	732.	577.	326.	200.	107.	55.	22.	
		341.	605.	555.	451.	287.	160.	86.	51.	19.	
		261.	435.	413.	344.	226.	132.	54.	36.	13.	
		208.	364.	332.	274.	194.	100.	60.	23.	6.	
135.5		166.	287.	264.	196.	140.	85.	46.	19.	10.	
		115.	207.	216.	169.	114.	50.	41.	18.	9.	
		90.	177.	174.	133.	88.	56.	32.	12.	4.	
		66.	129.	131.	107.	83.	45.	22.	7.	2.	
140.5		61.	88.	92.	86.	64.	33.	17.	7.	4.	
		29.	68.	70.	57.	43.	23.	10.	6.	0.	
		21.	51.	55.	36.	26.	11.	2.	1.	2.	
		3.	18.	16.	17.	5.	4.	4.	2.	0.	

		Neutral MC, vacuum beam									
E =		45	55	65	75	85	95	105	115	125	GeV
z = 110.5 m		0.	0.	0.	0.	0.	0.	0.	0.	0.	0.
		0.	0.	0.	0.	1.	1.	1.	2.	2.	
		0.	0.	1.	1.	1.	3.	4.	7.	2.	
		0.	0.	0.	5.	2.	6.	13.	4.	14.	
115.5		0.	0.	3.	7.	9.	16.	16.	16.	13.	
		0.	2.	5.	20.	20.	31.	33.	19.	13.	
		3.	14.	24.	36.	57.	47.	39.	34.	21.	
		5.	17.	47.	75.	91.	71.	57.	29.	32.	
120.5		8.	57.	107.	126.	120.	108.	72.	50.	34.	
		24.	101.	172.	200.	144.	99.	94.	59.	21.	
		40.	124.	209.	222.	162.	112.	94.	41.	29.	
		56.	163.	225.	226.	154.	130.	76.	65.	25.	
125.5		80.	199.	242.	250.	189.	118.	72.	44.	31.	
		67.	170.	269.	220.	197.	118.	76.	36.	28.	
		83.	246.	310.	247.	184.	104.	78.	54.	21.	
		104.	258.	273.	242.	154.	116.	74.	51.	20.	
130.5		118.	277.	272.	242.	140.	101.	71.	36.	13.	
		144.	251.	294.	218.	172.	109.	65.	23.	9.	
		158.	269.	301.	226.	158.	81.	61.	30.	12.	
		176.	303.	309.	261.	147.	98.	44.	25.	12.	
135.5		183.	274.	313.	212.	158.	83.	43.	22.	11.	
		234.	308.	286.	193.	120.	82.	46.	29.	12.	
		214.	331.	284.	217.	133.	78.	38.	15.	10.	
		243.	321.	280.	215.	110.	61.	21.	12.	5.	
140.5		223.	331.	287.	197.	113.	71.	25.	17.	6.	
		265.	360.	295.	181.	101.	59.	33.	7.	7.	
		267.	350.	279.	137.	88.	48.	26.	15.	1.	
		200.	231.	186.	120.	58.	31.	4.	6.	1.	

6.3 Background estimation

The kinematic cuts on the data gave us quite a clean sample of kaon decays, as can be seen from Figures 29, 55, and 56, but there were still small backgrounds which had to be treated separately. The following discussion will describe our methods of estimating the sizes of our backgrounds.

6.3.1 Diffractive and inelastic regeneration

Both the charged and the neutral data samples contained some diffractively or inelastically regenerated events. Because our resolution was much better for the charged decays, the p_t^2 backgrounds were studied there first. Recall that our p_t^2 cut for charged mode was 250 (MeV/c)^2 ; for background fits we used events with $2000 \text{ (MeV/c)}^2 < p_t^2 < 100,000 \text{ (MeV/c)}^2$. These background events of all energies were fit to a function of $p_t^2(\equiv t)$ which assumed that the background shape was the sum of diffractive and inelastic scattering combined with detector acceptance:

$$[c_1(0.648e^{-184.7t} + 0.352e^{-26.17t}) + c_2e^{-6t}]e^{-c_3t} \quad (t \text{ in GeV}).$$

The factor multiplying c_1 describes the shape of the contributions from diffractive regeneration which was obtained from a special Monte Carlo program which modeled the scattering in our regenerator. The first of these terms describes the scattering from lead; the second describes the scattering from boron carbide. The different fall-off rates reflect the difference in nuclear sizes and resulting p_t^2 kicks as described earlier in the section on the design of the experiment. The term which includes c_2 describes inelastic scattering; the exponent is an empirically derived constant measured in previous experiments. The overall exponential factor containing c_3 describes the effects of our acceptance. The free parameters for the fit were c_1 , c_2 , and c_3 , and the fit gave a ratio

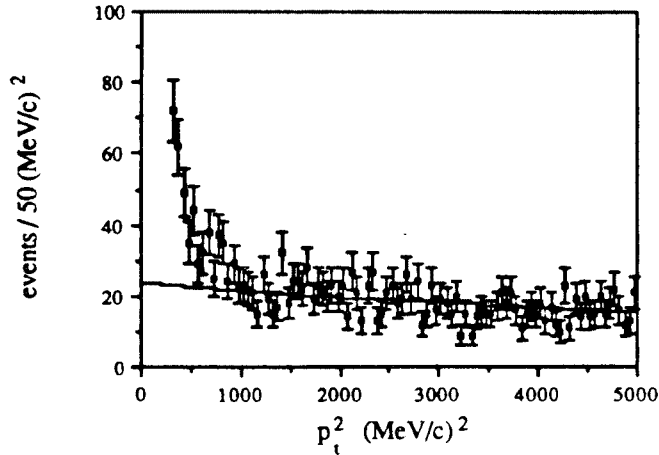


Figure 61. p_t^2 for the charged regenerated events. The line indicates the fit function. The first two data bins are beyond the plot scale. This represents about 1/3 of the total charged data sample.

of diffractive to inelastic events of 0.312. We then assumed that each energy bin had a p_t^2 background which could be described by the function above and which had the same ratio of diffractive to inelastic events as the sample as a whole. Fitting for c_1 and c_3 in each energy bin and integrating the resulting function below 250 (MeV/c)^2 gave us a background estimate of 0.2%. (See Figure 61.)

A similar treatment of the neutral regenerated background also had to consider resolution smearing, which was much greater than for the charged mode. Here the events used to estimate the background had $20,000 \text{ (MeV/c)}^2 < p_t^2 < 100,000 \text{ (MeV/c)}^2$. The function used was almost the same, with an additional term added to account for coherent events which had smeared beyond $20,000 \text{ (MeV/c)}^2$ and so raised the estimate of the background:

$$[c_1(0.648e^{-184.7t} + 0.352e^{-26.17t}) + c_2e^{-6t}]e^{-c_3t} + c_4e^{-103(t-0.02)}. \quad t \text{ in } (\text{GeV}/c)^2$$

The coefficient in the exponent of the final term and c_4 were determined from Monte

Carlo studies of the p_t^2 resolution.

Since we could no longer assume that all of the events with $p_t^2 < 20,000 (\text{MeV}/c)^2$ were background, it was difficult to estimate the size of the coherent signal. The ratio of the signal to background was not known, and since the number of “good” events depended on how much background we thought there was, an iterative approach was adopted. As a starting point, we assumed that the ratio of diffractive background to signal for $p_t^2 < 20,000(\text{MeV}/c)^2$ was the same as in charged mode since we used the same regenerator in charged and neutral modes. An initial guess of the amount of diffractive background fixed c_1 . We then fit for the other parameters to obtain a better background estimate. This new estimate changed how many coherent events we thought there were, and, since we assumed the diffractive to coherent ratio was fixed, the number of diffractive events. The procedure was repeated until the background estimate for $p_t^2 < 20,000(\text{MeV}/c)^2$ converged. The background for each energy bin was thus determined to be about 3.2%, approximately independent of energy. (See Figure 62.) This background could have a different proper time spectrum than the coherent decays, possibly shifting the phase. This problem will be discussed in more detail below.

6.3.2 Semileptonic decays

The background of events decaying by $K_L \rightarrow \pi l \nu$ in the sample of $K_L \rightarrow \pi^+ \pi^-$ decays is small, as seen in Figure 29. We used our Monte Carlo simulation to generate and reconstruct $K_L \rightarrow \pi e \nu$ and $K_L \rightarrow \pi \mu \nu$ events. Because the neutrino was undetected, we expected the reconstructed K to have a nonzero transverse momentum. The resulting simulated p_t^2 shapes were fit to exponentials. The sum of these to forms were fit to the data and extrapolated under the forward peak. The p_t^2 shape of the

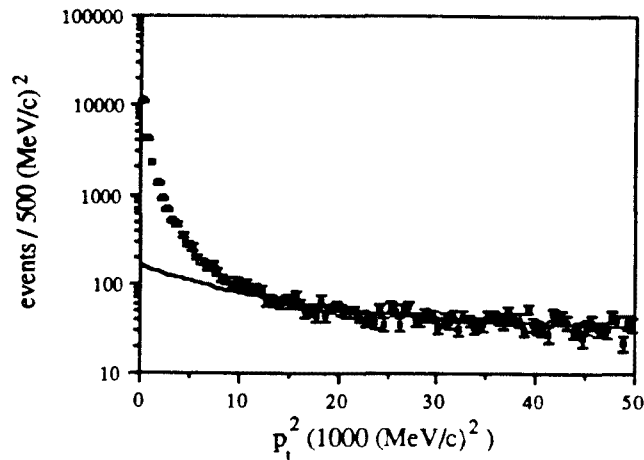


Figure 62. p_t^2 for neutral regenerated events. The line indicates the fit to the background.

Monte Carlo events was checked against the p_t^2 shape of data events obtained in special semileptonic runs; the fit was found to be consistent with the data. We estimated the background to be about 1.2% of the total number of events in the mass peak. Although the vacuum beam contained no phase information, we did use the K_L events as a flux constraint. This will be discussed further below.

6.3.3 $K_L \rightarrow 3\pi^0$ decays

We estimated the background to $K_L \rightarrow 2\pi^0$ decays from misreconstructed $K_L \rightarrow 3\pi^0$ decays with a stand-alone Monte Carlo simulation which generated kaon decays into two and three pions. The photons from pion decay were tracked through the detector and event reconstruction was attempted. After taking into account the differences in the published branching ratios and the probabilities of photon conversion in the lead sheet, we obtained an estimate of the fraction of $3\pi^0$ events which reconstructed under the $2\pi^0$ mass peak as a function of kaon energy. (See Table 7.) These fractions have uncertainties

of about 10% of the values themselves.

Table 7. Fraction of events in 2π mass peak from 3π decays

kaon energy (GeV)	background correction
45	.0200
55	.0155
65	.0134
75	.0142
85	.0167
95	.0195
105	.0230
115	.0271
125	.0315

These values were cross-checked by using only the $3\pi^0$ Monte Carlo to find the ratio of $3\pi^0$ events with $400 \text{ MeV}/c^2 < m_K < 460 \text{ MeV}/c^2$ to the number of $3\pi^0$ Monte Carlo events under the mass peak. We then used this ratio with the number of data events with $400 \text{ MeV}/c^2 < m_K < 460 \text{ MeV}/c^2$ to give the number of $3\pi^0$ events under the mass peak. The estimated numbers of $3\pi^0$ background events under the mass peak obtained in this way were consistent with the results above.

6.4 Finding the phase difference

In preparation for the determination of the phase difference from the final data set, we shall now describe the actual background subtraction process for the neutral mode regenerated beam data. No subtraction was done for the charged regenerated beam data because the better resolution and tighter p_t^2 cuts gave smaller backgrounds

which we took to be negligible. We discussed earlier how the size of the diffractive and inelastic regeneration was estimated. In practice, subtracting this background correctly was difficult because the phase as well as the momentum of a kaon could change in the scattering, thus changing the shape of the decay spectrum. We decided to let the data give us the appropriate K_S - K_L interference shape in z . This meant choosing events with large p_t^2 and using them to give the correct z shape for the subtraction. One concern here was that the ratio of diffractive to inelastic contributions to the background changed rapidly between the coherent peak region and the region from which we wanted to take the background shape, and there was no reason why a phase shift from diffractive scattering should be the same as a phase shift from inelastic scattering. We verified that this was not a problem in the charged mode where the p_t^2 resolution was much better. Z spectra as a function of momentum for events with $1000 \text{ (MeV}/c)^2 \leq p_t^2 < 10,000 \text{ (MeV}/c)^2$ were compared with similar spectra for events with $10,000 \text{ (MeV}/c)^2 \leq p_t^2 < 35,000 \text{ (MeV}/c)^2$. Even though the diffractive to inelastic ratio changed from roughly 1.6 for the low p_t^2 range to 0.7 for the high range, we found that the agreement of the z spectra was acceptable within the statistics (Figure 63). In order to apply the subtraction to the neutral data, events with $20,000 \text{ (MeV}/c)^2 \leq p_t^2 < 40,000 \text{ (MeV}/c)^2$ which passed all other cuts were binned by momentum and decay vertex and the total contents of each p bin scaled to give 3.2% background. (See Table 8.)

We now determined the phase of η by varying the phase of the Monte Carlo events. Rather than generating many Monte Carlo samples with different phase angles, we

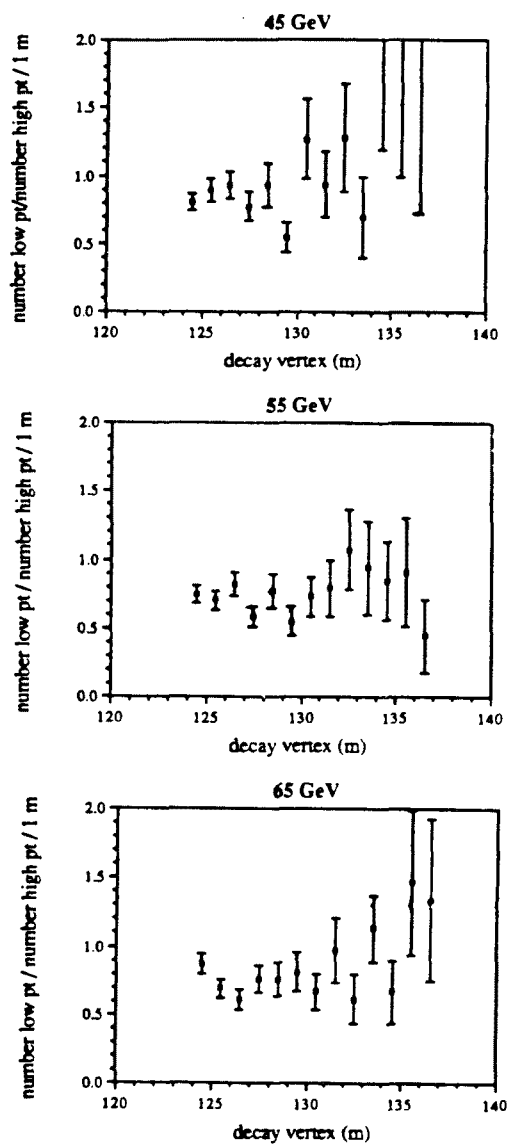


Figure 63. Ratio of the number of events in the diffractive-dominated background to the number of events in the inelastic-dominated background as a function of decay vertex for each energy bin.

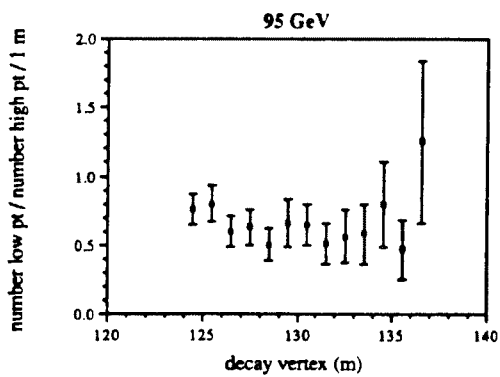
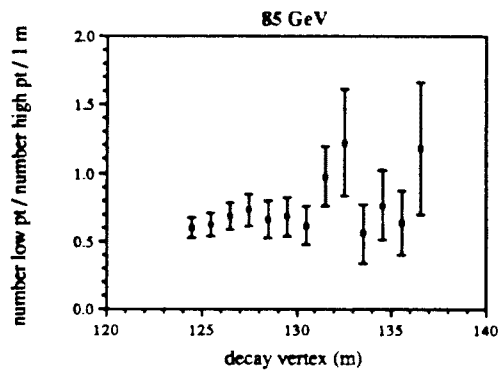
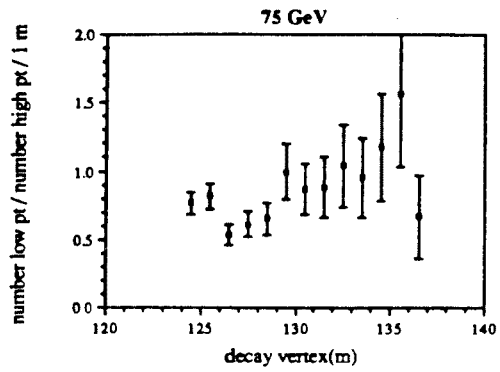


Figure 63., cont.

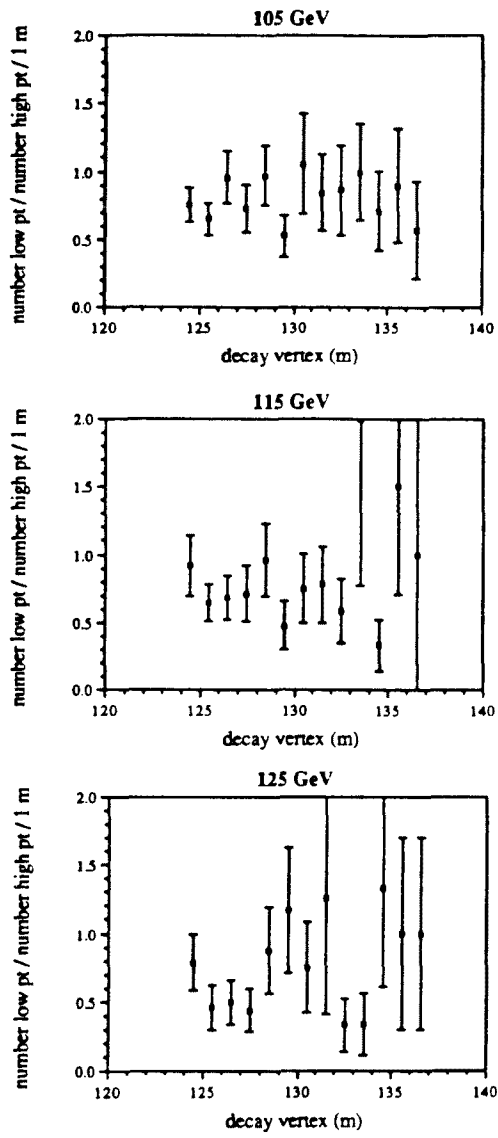


Figure 63., cont.

Table 8. p_i^2 background subtraction in (E,z) bins

$E =$	45	55	65	75	85	95	105	115	125	GeV
$z = 124.5$ m	5.3	8.9	12.9	8.6	6.5	4.6	1.8	0.2	0.3	
	5.3	12.7	13.3	10.1	9.4	5.3	2.9	1.3	0.3	
126.5	5.9	12.7	11.5	14.0	8.6	2.3	1.8	1.3	0.6	
	1.2	8.0	11.5	7.8	6.1	3.6	1.6	0.7	0.0	
128.5	3.5	5.2	11.5	9.0	5.0	3.6	1.8	1.5	0.3	
	1.8	6.6	4.1	3.9	3.2	3.0	2.1	0.9	0.6	
130.5	4.1	3.3	4.1	3.9	3.2	1.7	0.5	0.9	1.0	
	2.4	3.8	4.6	1.2	2.5	2.0	0.8	0.2	0.0	
132.5	3.5	1.4	2.8	2.3	2.2	1.7	0.5	0.2	0.0	
	1.2	2.8	3.2	1.6	0.4	1.0	0.3	0.0	0.0	
134.5	0.0	2.8	1.4	0.8	0.4	0.3	1.0	0.2	0.0	
	0.6	1.9	2.3	0.8	0.7	1.3	0.5	0.2	0.0	
136.5	0.6	0.5	0.5	0.4	0.4	1.0	0.0	0.0	0.0	

reweighted each Monte Carlo (E, z) bin by a factor

$$\frac{[|\rho|^2 e^{-\Gamma_S \tau} + 2|\rho||\eta| e^{-(\Gamma_S + \Gamma_L)\tau/2} \cos(\Delta m \tau + \phi_\rho - \phi_\eta) + |\eta|^2 e^{-\Gamma_L \tau}]_{\phi_\eta = \phi_{\text{trial}}, \rho = \rho_{\text{trial}}}}{[|\rho|^2 e^{-\Gamma_S \tau} + 2|\rho||\eta| e^{-(\Gamma_S + \Gamma_L)\tau/2} \cos(\Delta m \tau + \phi_\rho - \phi_\eta) + |\eta|^2 e^{-\Gamma_L \tau}]_{\phi_\eta = 45^\circ, \rho = \rho_{MC}}}, \quad (2)$$

since 45° was the value with which the Monte Carlo samples were generated. The proper time τ here, however, was the proper time associated with the *true* energy and decay position, not the reconstructed quantities. Since resolution smearing (at least in z) was large in the neutral mode, the proper time obtained from the reconstructed values of E and z was not the true proper time. In addition, because the energy and vertex distributions were nonlinear across the width of a bin, the (E, z) bin centers were not even the best approximations for the charged mode. To get better values, we generated samples of Monte Carlo events and calculated the average true energy and decay vertex for each bin of reconstructed events. The shape of the E_{true} vs. $z_{\text{reconstructed}}$ curves suggested fits of the energy values to a quadratic function of $z_{\text{reconstructed}}$. Because the differences between the neutral z bin center and the average true z value, Δz , rose steeply for points upstream of the regenerator, fell sharply downstream of the lead sheet, and were fairly constant in the decay volume, the Δz 's were fit to a cubic function of $z_{\text{reconstructed}}$. In the charged mode the Δz 's were fit to a constant, as the resolution smearing was negligible at either end of the decay volume. These functional forms then gave us values for the average true energy and vertex for each reconstructed bin. (See Figures 64-67.)

This left Γ_S , Γ_L , Δm , ρ , and η to be determined. The first three of these parameters as well as $|\eta|$ were fixed to the previously measured values shown in Table 9. The regeneration amplitude ρ was calculated from the expression⁶

$$\rho = i\pi \frac{f(0) - \bar{f}(0)}{k} \Lambda_S N \frac{1 - \exp[(i\Delta m/\Gamma_S - \frac{1}{2})l]}{\frac{1}{2} - i\Delta m/\Gamma_S},$$

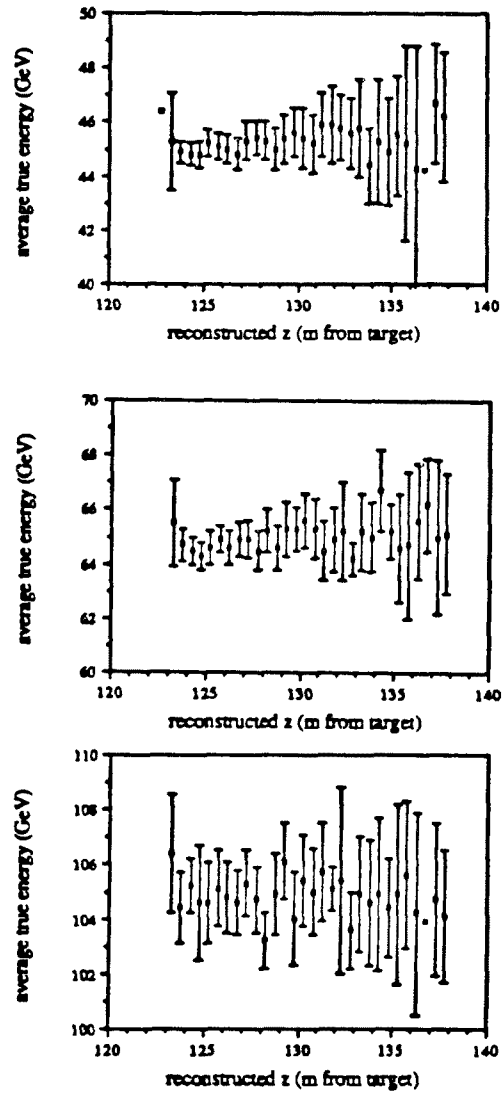


Figure 64. Average true energy as a function of reconstructed z vertex for charged Monte Carlo events. The top plot shows decays with reconstructed energies between 40 and 50 GeV; the middle, 60-70 GeV; the bottom, 100-110 GeV. Points with no error bars had fewer than six events contributing to the average.

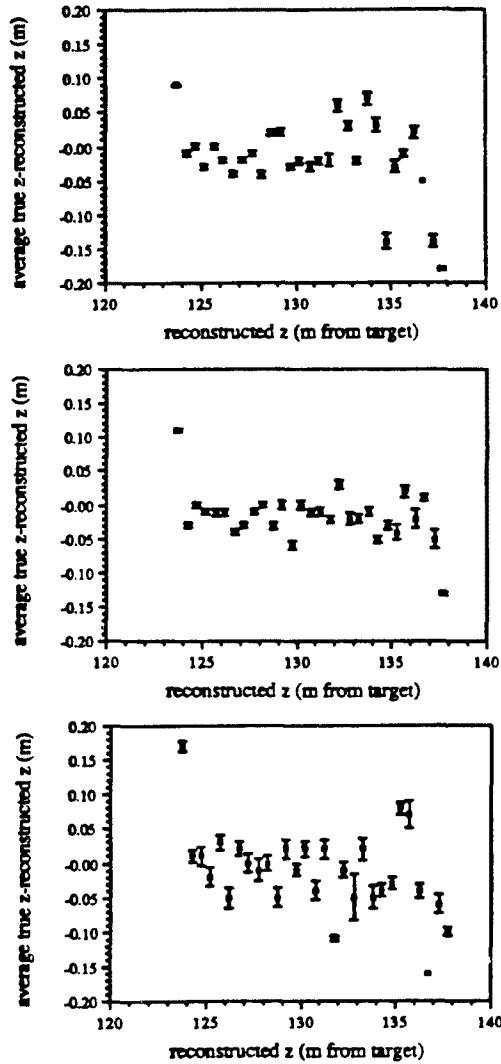


Figure 65. The difference between average true z and reconstructed z as a function of reconstructed z for charged Monte Carlo events. The top plot shows decays with reconstructed energies between 40 and 50 GeV; the middle, 60-70 GeV; the bottom, 100-110 GeV.

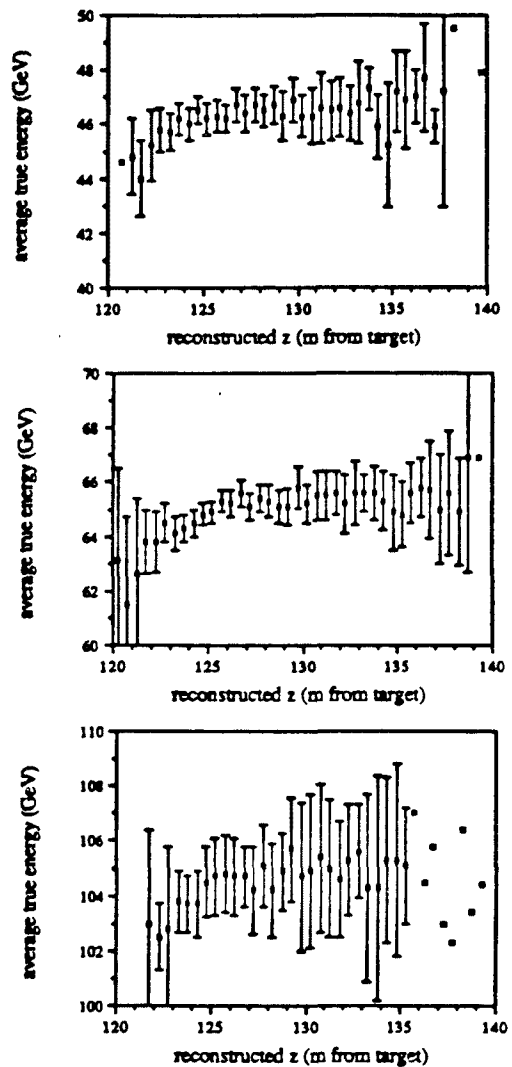


Figure 66. Average true energy as a function of reconstructed z vertex for neutral Monte Carlo events. The top plot shows decays with reconstructed energies between 40 and 50 GeV; the middle, 60-70 GeV; the bottom, 100-110 GeV.

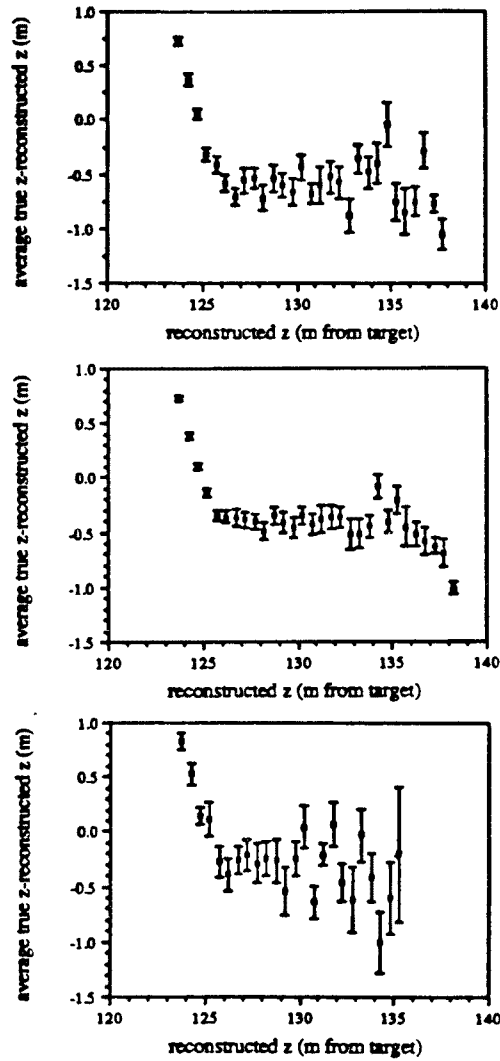


Figure 67. The difference between average true z and reconstructed z as a function of reconstructed z for neutral Monte Carlo events. The top plot shows decays with reconstructed energies between 40 and 50 GeV; the middle, 60-70 GeV; the bottom, 100-110 GeV.

where

- $k = p_K/\hbar$ is the kaon wave number,
 $\Lambda_S = \beta\gamma\tau_S$ is the mean K_S decay length,
 N is the scattering center density, and
 $l = L/\Lambda_S$ is the regenerator length in units of K_S decay lengths.

The geometry and density of the regenerator as well as the scattering amplitudes for lead were known; the scattering amplitudes for boron carbide, however, had not been previously measured. Other studies¹⁷ have shown that $|(f(0) - \bar{f}(0))/k|$ is well-described as an exponential function of kaon momentum:

$$\left| \frac{f - \bar{f}}{k} \right| = \left| \frac{f - \bar{f}}{k} \right|_{70 \text{ GeV}/c} \left(\frac{p}{70 \text{ GeV}/c} \right)^{-\alpha}.$$

A fit to $|(f - \bar{f})/k|$ at 70 GeV and α for boron carbide was included in the grand fit for ϵ'/ϵ ; the values obtained from this fit (corresponding to $|(f - \bar{f})/k|$ at 1 GeV = 74.9 mb, $\alpha = -.609$) were used for the regeneration parameters in the trial value of the decay spectrum. (The Monte Carlo events were generated with $|(f - \bar{f})/k|$ at 1 GeV = 70.4 mb and $\alpha = -.621$.)

Table 9. Fixed parameter values for phase fit.

Variable	Value
Γ_S	$1.120 \times 10^{10} \hbar \text{ s}^{-1}$
Γ_L	$0.002 \times 10^{10} \hbar \text{ s}^{-1}$
Δm	$0.5349 \times 10^{10} \hbar \text{ s}^{-1}$
$ \eta $	0.0022

Because we did not know our absolute incident kaon flux very well, we could only match the shapes of the data and Monte Carlo decay spectra; we therefore also had

to fit for the overall normalizations. The phase fit was very sensitive to the values obtained for this normalization, since the freedom of ϕ_η allowed the interference term of the decay spectrum to at least partially compensate for an under- or overestimate of the size of the distribution by the pure K_S term. Differences in the reconstructed energy spectra between data and Monte Carlo made it necessary to assign a separate normalization constant to each momentum bin. This extra freedom in the fit added to the uncertainty in the ϕ_η determinations, so we looked for a way to constrain these normalization parameters. We used the data from the vacuum beam for this purpose since they contained no phase information yet were collected under the same conditions as the regenerated beam data. The neutral vacuum beam data were corrected for $3\pi^0$ background contamination as described above and were incorporated in the fit as described below. This added constraint did help to reduce the uncertainty on the phase determination to a small extent.

Recall that we took charged data in three separated running periods. We found some differences in the reconstructed sizes of the beams for each set due to small changes in collimator settings in between charged runs. Each of these data sets was therefore described by a separate Monte Carlo sample which differed only in the dimensions used for the collimators. We constrained the charged phase to be the same for all three of the charged sets. We used the charged vacuum events without performing a background subtraction since the background was small.

Up to now we have considered the determinations of the charged and neutral phases separately. Because of our sensitivity to the uncertainties in the normalization and the regeneration amplitude of boron carbide, the systematic errors on the individual phases were large. To reduce our sensitivity to the second of these, which was common to both charged and neutral modes, we fit for the difference $\phi_{00} - \phi_{+-}$ (instead of ϕ_{00} alone),

as well as ϕ_{+-} .

The actual fit was done by a χ^2 minimization. Each (E,z) bin of regenerated beam data contributed a term χ_{Ez}^2 , where

$$\chi_{Ez}^2 = \frac{(d - r)^2}{r + \frac{r^2}{m}},$$

where

d is the number of data events in the bin,

r is the number of Monte Carlo events in the bin multiplied by the factor in equation (2) as well as a normalization constant $c_i(E)$, and

m is the number of Monte Carlo events in the bin.

The contributions from the vacuum beam data were similar, although in this case r was given by

$$r = b_j c_i(E),$$

where $c_i(E)$ is the same as for the regenerated data and b_j is an overall constant. The j runs over the four data sets, three charged and one neutral. To see why a constant b was chosen, consider the data-to-Monte Carlo ratios for regenerated and vacuum events after the proper time spectra have been made to agree:

$$\frac{d_R}{m_R} = \frac{N_0}{N_{MR}} e^{-L/\Lambda} \Gamma(K_S \rightarrow 2\pi^0)$$

and

$$\frac{d_V}{m_V} = \frac{N_0}{N_{MV}} \Gamma(K_L \rightarrow 2\pi^0).$$

Here d and m are as above, L/Λ is the absorber length in units of interaction lengths, N_0 is the number of K_L incident on the absorber, and N_M is the number of events generated by the Monte Carlo. We find d_R/m_R is proportional to d_V/m_V and note

that d_R/m_R after fitting is $c_i(E)$. We are thus led to an energy-independent constant. The sum of all of these $\chi_{E_i}^2$ formed the total χ^2 which was then minimized using the MINUIT package.

Chapter 7

RESULT AND ESTIMATE OF SYSTEMATIC ERRORS

7.1 Result

The above analysis yields a value for the phase difference of

$$\Delta\phi \equiv \phi_{00} - \phi_{+-} = -0.2^{\circ} \begin{matrix} +10.3^{\circ} \\ -9.3^{\circ} \end{matrix}$$

and a value of

$$\phi_{+-} = 46.7^{\circ} \begin{matrix} +3.1^{\circ} \\ -2.9^{\circ} \end{matrix}$$

with a χ^2 of 1009 for 968 degrees of freedom. The errors quoted above are statistical; the systematic errors will now be investigated.

7.2 Estimates of systematic errors

Let us first check the sensitivity of the fit to our choices of z bin size, upstream and downstream limits of the decay vertex, and energy range. The bin size was reduced from one meter to 0.5 meter with a change of only 0.2° in $\Delta\phi$. The upstream vertex limit on the range of the fit was varied between 123 m and 127 m. Our value for the phase difference was affected only by the cuts downstream of 124 m, which pushed the phase difference lower by about 1.3° . Varying the downstream limit also tended to push the phase difference lower; we observed a variation of about $\pm 4^{\circ}$ for downstream limits of the fit region between 132 m and 139 m. The asymmetry in sensitivity at the upstream end was probably caused by the difficulty of trying to establish the normalization from the steeply falling portion of the decay spectrum alone. The shift at the downstream end

was surprising because the proper time spectrum was rather insensitive to ϕ_η for most of our kaon energies at the downstream end of the decay volume as well as containing a comparatively small number of events. (See Figure 68.) This may be the sign of a problem with our understanding of the energy determination in the neutral mode.

The energy range used for the phase analysis was 40-130 GeV for neutral mode decays and 30-130 GeV for charged decays. The neutral energy range could not be extended at the level of the statistics we had, so this was not varied. The charged mode energy range was investigated: the phase difference was unaffected by the addition of events with energies from 140 to 160 GeV, while discarding the 30 GeV bin increased $\Delta\phi$ by 2° .

Errors associated with other features of the fitting procedure were also investigated. The vacuum beam events were introduced as a constraint to decrease the uncertainty in the normalization; they did, however, have some uncertainties of their own. Ignoring the vacuum beam events altogether, however, increased the phase difference by only 0.4° , so these uncertainties were negligible.

The effect of the determination of the average true energies and decay vertices was also examined. Although using just the (E,z) bin centers changed our phase result by 0.9° , a study of variations in the parameters for the neutral energies showed that the phase difference changed by only 0.1° , again a small effect.

Our background subtractions were also possible sources of systematic error. The K_S diffractive and inelastic subtraction was checked for sensitivity to the scale factors used in each energy bin to give the appropriate size of background. The error on these factors came from the statistical errors on the number of events in each momentum bin. The phase fit was insensitive to changes of one standard deviation of these values. The $3\pi^0$ background subtraction for neutral vacuum beam events changed the phase

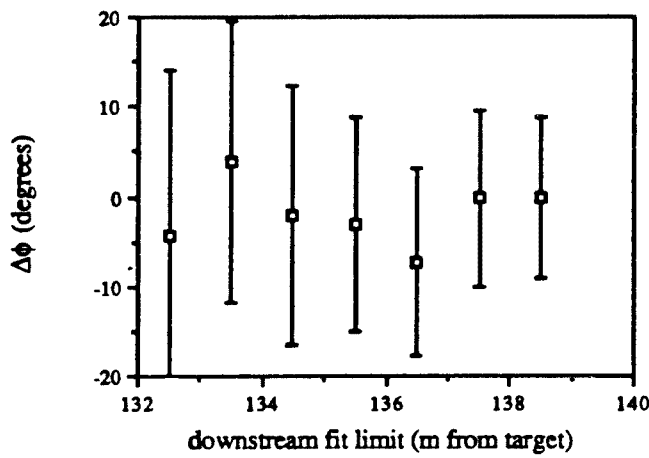
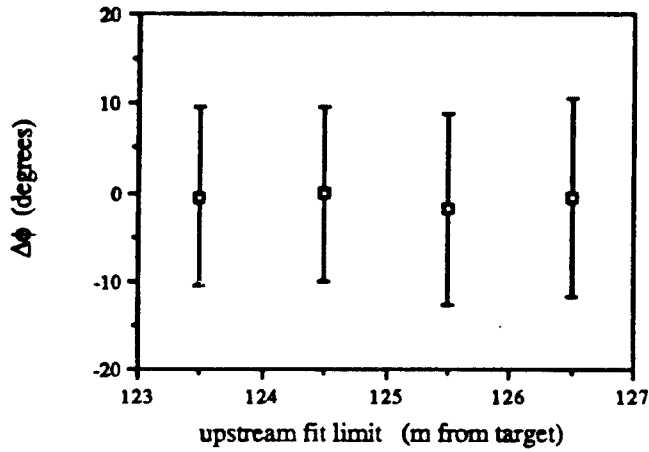


Figure 68. $\phi_{00} - \phi_{+-}$ as a function of limits on the length of the decay volume used in the fit. The top graph shows the behavior of $\Delta\phi$ as the upstream limit is varied; the downstream limit is fixed at 138 m. The bottom graph shows $\Delta\phi$ behavior as the downstream limit is varied; the upstream limit is fixed at 123 m.

difference by only -0.1° .

Of the constants assumed for the fit, the regeneration parameters for boron carbide were a particular source of concern, since the overall size of the spectrum was determined by $c_i|\rho|$. Changes in $|(f - \bar{f})/k|$ at 1 GeV of one standard deviation from the central fit value gave deviations of about 0.4° . Similar variations in the power law exponent gave changes in $\Delta\phi$ of at most 0.1° . Thus as far as the phase difference was concerned, these uncertainties were negligible. It must be noted, however, that each of the phases ϕ_{00} and ϕ_{+-} individually is quite sensitive to the regeneration amplitude because of the $c_i|\rho|$ coupling. In addition to uncertainty in the magnitude of $(f - \bar{f})/k$, there was also some uncertainty in its phase. This phase is related to the power law α of the momentum dependence of $|(f - \bar{f})/k|$, as discussed in reference 18. From the value of α used in the fit, we calculated that the phase of $(f - \bar{f})/k$ for boron carbide should differ by 1° from the nominally used value (-126.1°). Fitting for $\Delta\phi$ with this new value changed the phase by only 0.2° .

We have discussed above that we were especially sensitive to the neutral energy scale since it entered into the calculation of the z vertex as well as the kaon energy. Data to Monte Carlo comparisons of $2\pi^0$ and $3\pi^0$ decay modes suggested that the introduced energy scale factor of 0.996 might have been as low as 0.993. We therefore generated two additional sets of Monte Carlo events, one with a factor of 0.993 and the other with a value of 1. By fitting for $\phi_{00} - \phi_{+-}$ as a function of the downstream limit of the z vertex, we found a shift of about 2° from the nominal values. (See Figure 69.) A similar fit to the event set with no energy scale correction is shown for comparison. We have also estimated the effects of a systematic shift of the Monte Carlo acceptance by using reconstructed decay vertices which are just the usual reconstructed vertices plus a term linear in z . Our sensitivity measured in this way is that a shift of .001 per

meter of decay volume gives a 1.4° shift in the phase. Studies indicated that there was an acceptance disagreement of 0.4-0.5% in charged mode and 0.3% in neutral mode. Both shifts were in the same direction, though, so the net effect on the phase difference should be at most 2.8° .

7.3 Conclusion

A consideration of the largest contributions of systematic effects above, then, (see Table 10.) suggests a total systematic uncertainty of approximately 5.8° , giving

$$\phi_{00} - \phi_{+-} = -0.2^\circ \begin{matrix} +10.3^\circ \\ -9.3^\circ \end{matrix} \text{ (statistical)} \pm 5.8^\circ \text{ (systematic)}.$$

Within errors we see no evidence for a phase difference or the accompanying *CPT* violation, although within our uncertainties our result does not disagree with that of Christenson *et al.*¹²

7.4 Future plans

While the results presented here do not have sufficient sensitivity to make a strong statement about *CPT* conservation, better measurements of the phase difference are being planned. At this writing, experiment 731 is in the middle of a second data collection run which is expected to yield ten times more events than the data sample used in this analysis, with a corresponding increase in sensitivity. Unless systematic problems dominate that analysis, the combined statistical and systematic error should be about the same size as the error estimated by the NYU group.

In addition, the Fermilab program committee has approved a proposal¹⁹ for a dedicated measurement of the phase difference to run two years from now with essentially the same spectrometer as that used here. The major difference will be the conversion

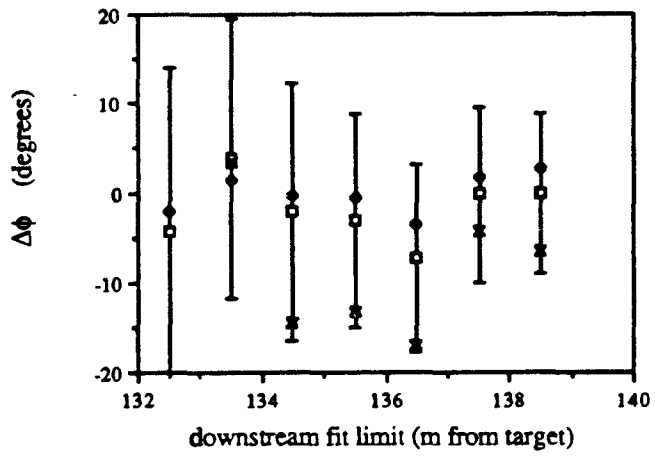


Figure 69. $\Delta\phi$ as a function of downstream limits of the fit decay volume. The open boxes with errors indicate results for the nominal energy scale; open diamonds indicate results for 0.993. The x's indicate results for an energy scale of 1.

Table 10. Summary of systematic effects.

Effect	Change in $\Delta\phi(^{\circ})$
<i>z</i> bin size	0.2
upstream <i>z</i> limit	1.3
downstream <i>z</i> limit	4.0
charged mode energy range	2.0
inclusion of vacuum events	0.4
uncertainties in average true <i>E</i> and <i>z</i>	0.1
uncertainty in neutral mode p_1^2 subtraction	< 0.1
uncertainty in vacuum $3\pi^0$ subtraction	0.1
uncertainty in boron carbide $ (f - \bar{f})/k $	0.4
uncertainty in boron carbide α	0.1
uncertainty in phase of boron carbide $(f - \bar{f})/k$	0.2
uncertainty in energy scale factor	2.0
inaccuracy of Monte Carlo acceptance	2.8

$$\sigma^2 \approx 1.3^{\circ 2} + 4.0^{\circ 2} + 2.0^{\circ 2} + 2.8^{\circ 2}$$

$$\sigma = 5.8^{\circ}$$

of the current vacuum beam to another regenerated beam with a second regenerator 14 m upstream of the decay volume. The distance is chosen to put the proper time spectrum from the upstream beam in a region where it is fairly insensitive to the phase at the decay volume. By using a one interaction length upstream regenerator and a two-thirds interaction length downstream regenerator, the proper time spectra for decays from the two beams in the decay volume fall at about the same rate; hence the resolution smearing from one proper time bin to another should be the same for both beams. Tentative plans also call for the recording of both charged and neutral modes of both beams simultaneously to further reduce systematic errors and to provide more cross checks, such as verifying the glass calibration with $\pi^+\pi^-\pi^0$ events. To extract the

phase difference, the double ratio of

$$R = \frac{(\text{neutral upstream regenerator beam decays})/(\text{neutral downstream decays})}{(\text{charged upstream decays})/(\text{charged downstream decays})}$$

will be formed with the decays again binned by energy and decay vertex. This should eliminate problems with understanding the acceptance and the resolution smearing since these will cancel to first order. Care will have to be taken that the z scales for charged and neutral mode are the same, but this can be checked using many of the techniques from E731. The difference $R - 1$ is expected to yield a value of .01 for each degree of phase difference from Monte Carlo studies which also indicate that the method should have a precision of about one degree given statistics similar to those in the second run of E731.

Two experiments at CERN, one running at the SPS and one to run at the new LEAR facility, will also attempt to provide better measurements of the phase difference. The existing NA31 experiment has just completed an ϵ'/ϵ measurement. This group collects $\pi^+\pi^-$ and $\pi^0\pi^0$ decays simultaneously from a target which can be moved close to or far from their proton target to give K_S and K_L . Their third data collection run will be dedicated to measuring the phase difference, which they estimate they can do with a statistical uncertainty of 1° . Systematics may be more of a problem in the analysis of this experiment, since they will have to understand the acceptance of their detector very well in order to correct for it. A total of 10^8 kaon decays are anticipated. The new LEAR experiment will collide protons with antiprotons to create charged and neutral kaons. The sign of the charged K will determine whether the neutral particle was a K^0 or \bar{K}^0 by strangeness conservation. They too will need lots of statistics to get to their proposed uncertainty in the phase difference of 2° .

References

1. W. Pauli, in *Neils Bohr and the development of physics*, W. Pauli ed. McGraw-Hill, New York, 1955.
G. Lüders, *Dan.Mat.Fys.Medd.* **28**(1955) no.5.
G. Lüders, *Ann. Phys.* **2**(1957)1.
R. Jost, *Helv. Phys. Acta* **30**(1957)409.
2. The proofs by Lüders and Pauli (cited below) each additionally assume that the usual spin and statistics relations for fermions and bosons hold, that products of boson (fermion) fields in the Hamiltonian are replaced with a symmetric (antisymmetric) linear combination of the fields, and that any fermion fields which are not kinematically dependent on each other anticommute. The work of Jost provided a more rigorous basis for the *CPT* Theorem. Jost assumed only that the theory was Lorentz invariant, that the energy of all states was ≥ 0 , and that weak local commutativity held, a weaker assumption than the spin-statistics connection. I wish to thank Professor A. S. Wightman for his helpful comments on the *CPT* Theorem.
3. Particle Data Group, *Phys. Lett.* **170B**(1986)1.
4. K. Lande *et al.*, *Phys. Rev.* **103**(1956)1901.
5. J.H. Christenson *et al.*, *Phys. Rev. Lett.* **13**(1964)138.
6. K. Kleinknecht, *Ann. Rev. Nucl. Sci.* **26**(1976)1. This review contains a thorough description of neutral kaon phenomenology and *CP* phenomenology.
7. V.V. Barmin *et al.*, *Nucl. Phys. B* **247**(1984)293. This comprehensive paper contains many of the details for the *CPT* violation phenomenology presented in this thesis.
8. T.J. Devlin and J.O. Dickey, *Rev. Mod. Phys.* **51**(1979)237.
9. J.W. Cronin, *Rev. Mod. Phys.* **53**(1981)373.
10. V.F. Weisskopf and E.P. Wigner, *Z. Physik* **63**(1930)54.
V.F. Weisskopf and E.P. Wigner, *Z. Physik* **65**(1930)18.
11. J.W. Cronin, *Acta Physica Polonica* **B15**(1984)419.
12. J.H. Christenson *et al.*, *Phys. Rev. Lett.* **43**(1979) 1209.
J.H. Christenson *et al.*, *Phys. Rev. Lett.* **43**(1979)1212.

13. G. Charpak and M. Gourdin, *The $K^0 \bar{K}^0$ system*, CERN 67-18, 11 July 1967.
14. More details on the properties of lead glass and our particular block-phototube assembly can be found in the thesis of R.H. Bernstein, University of Chicago (unpublished).
15. E. Longo and I. Sestili, *Nucl. Inst. and Meth.* **128** (1975)283.
16. A.J. Malensek, *Empirical formula for thick target production*, Fermilab document FN-341, 12 Oct 1981.
17. A. Gsponer *et al.*, *Phys. Rev. Lett.* **42**(1979)13.
18. W.R. Molzon, Ph.D. thesis, University of Chicago (unpublished).
19. G.D. Gollin, spokesman. *Measurement of the phase difference between η_{00} and η_{+-} to a precision of 1°* , Fermilab proposal 773.